Kinetics of Deliquescence of Ammonium Sulfate Particles

By

Rocsana Gabriela Pancescu

A thesis
presented to the University of Waterloo
in fulfillment of the
thesis requirement for the degree of
Doctor of Philosophy
in
Chemistry

Waterloo, Ontario, Canada, 2008

Author's Declaration

I hereby declare that I am the sole author of this thesis. This is a true copy of the thesis, including any required final revisions, as accepted by my examiners.

I understand that my thesis may be made electronically available to the public.

ABSTRACT

The goal of this project was to study the deliquescence kinetics of aerosol particles of atmospheric significance. In the course of this work a novel experimental method was developed, which utilizes the measurement of the water vapor loss in laminar aerosol flow to determine vapor uptake on the aerosol surface. The newly designed flow tube apparatus uses a system of Nafion based dryers and humidifiers, which greatly simplifies the optimization and control of the relative humidity in the aerosol flow. The design, which also utilizes a movable inlet, enables easy variation of the aerosol residence time in the deliquescence reactor, while keeping other experimental conditions constant.

In this study, a numerical retrieval procedure was used to characterize aerosols *in situ* from their IR extinction spectra. The procedure allows that the aerosol size, number distribution, phase and composition be determined, provided the optical constants of all the components (materials) comprising the aerosol are known. For the purpose of studying the deliquescence kinetics of ammonium sulfate aerosol and monitoring their evolution from solid to liquid (state), we have acquired a set of optical constants for a range of $(NH_4)_2SO_4$ compositions. A set of experiments in a somewhat modified flow tube set up was performed to produce AMS aerosols of known composition, including solid, saturated (water) solution (40 % wt.) and a series of diluted solutions with composition ranging between 40 and 10 % wt. in 5 % increments. The IR spectra of these model aerosols were used to derive the optical constants, using an inversion method proposed by Clapp. The derived refractive indices, which cover the spectral range from 590 to 5990 cm^{-1} with 2 cm^{-1} resolution, were compared with those already available in the literature. Using various examples to compare the quality of fittings to experimental spectra, we demonstrated that our optical constants present an improvement relative to those previously reported by B. Toon's (for crystalline AMS) and S. Martin's (for AMS solution). The suitability of applying this procedure to ammonium sulfate aerosols and its sensitivity to spectral range was also investigated and discussed.

As a preparatory step for the deliquescence kinetics study, our new flow tube apparatus and the tools for the characterization of aerosol were verified in a standard deliquescence experiment performed on $(NH_4)_2SO_4$ aerosols. The deliquescence process of an equilibrated aerosol flow was monitored as a function of increasing humidity and the deliquescence relative humidity (DRH) determined to be 79.6 ± 0.85 % which is, within experimental uncertainty, in an excellent agreement with the results reported by other research groups.

In the kinetic experiment, a flow of solid $(NH_4)_2SO_4$ aerosols is pre-humidified to a humidity close to, but enough below DRH that there is no detectable amount of liquid aerosols in the system. Such an equilibrated aerosol flow was introduced to the deliquescence reactor where it is further humidified in a controllable manner, by varying the position of the movable inlet. The amount of water transferred to the aerosol through the Nafion membrane was closely monitored, as well as the resulting increase in the water content in the aerosol flow (both gaseous and liquid). This was achieved by measuring the RHs and flow rates of the aerosol and humidification flow, and the characterization of aerosol composition and concentration using their IR spectra. The experimental conditions and aerosol residence times in the reactor where chosen such that no other diluted solution except for saturated $(NH_4)_2SO_4$ droplets were produced in the process. The number distribution of deliquesced aerosols and the corresponding change in the water content in the aerosol flow were used by a newly developed kinetic model to determine the kinetics of the deliquescence process. Assuming fully developed laminar flow conditions, the water vapor concentration in the flow and its depletion in the presence of aerosol was modeled, to retrieve the value of the water vapor uptake. In the case of micron-sized ammonium sulfate aerosols, which were used in this study, the uptake coefficient,γ, was determined to be $0.0072 \pm 6.54 \times 10^{-3}$. The uncertainty associated with this value, as well as the suggested improvements to the experimental procedure and the kinetic model in order to reduce the uncertainty were discussed.

ACKNOWLEDGEMENTS

I had the privilege to be a part of an extraordinary research group at the University of Waterloo. I have to thank my advisor Dr. Jim Sloan for his guidance, understanding, advice and encouragement during my five years of graduate studies.

I would also like to thank my present and former colleagues for their help, support and fruitful discussions. Special thanks go to Dr. Juan Najera and Dr. Rodion Remorov for their friendship and valuable advice during different stages of my research.

I am deeply indebt to my good friend and mentor Dr. Biljana Cosic, from who I learned many things about experimental physical chemistry and scientific writing. Thanks for everything Biljana.

DEDICATION

To my husband, Ciprian Pancescu for his love, support and continuous encouragement.

TABLE OF CONTENTS

Chapter nine: Concluding Remarks

LIST OF FIGURES

Chapter 4

Chapter 5

Chapter 6

Chapter 7

Chapter 8

Annex		*Page*
1	Efficiency of the Nafion dryer as a function of purge/aerosol flow rate at room temperature.	(137)
2	Nafion dryer efficiency dependence on the temperature and on the purge/aerosol flow rate.	(138)
4	Water removal (from the aerosol flow) dependence on the: purge/aerosol flow rate (black line), temperature & purge/aerosol flow rate (red line), second dryer – KOH & purge/aerosol flow rate (blue line), second dryer & temperature & purge/aerosol flow rate (yellow line).	(139)

LIST OF TABLES

List of Abbreviations

AIM	- Aerosol Inorganic Model
AMS	- Ammonium Sulfate
b.c	- Boundary Conditions
CCN	- Cloud Condensation Nuclei
DMA	- Differential Mobility Analyzer
DRH	- Deliquescence Relative Humidity
ERH	- Efflorescence Relative Humidity
FTIR	- Fourier Transform Infrared
i.d.	- Inner Diameter
KK	- Kramers-Kronig
KRS-5	- Thallium Bromo Iodide
MCT	- Mercury Cadmium Telluride
MS	- Mass Spectrometry
o.d.	- Outer Diameter
PSI	- Pounds per Square Inch
RH	- Relative Humidity
SEM	- Scanning Electron Microscopy
SLPM	- Standard Liters Per Minute
S/N	- Signal to Noise

Chapter One: Introduction

1.1 Introduction

It is well known that atmospheric aerosols (fine solid particles or liquid droplets suspended in air) have an important impact on global climate, environment and human health. Their role in these eco- and bio-systems is rather complex, since in a given process they can be involved both physically and chemically. In order to better understand the influence of aerosols on these systems, it is necessary that their physical and chemical properties, as well as their abundance and distribution in the atmosphere be well known. Recently, an increasing amount of research has been dedicated to characterize atmospheric aerosols and better understand the physical and chemical phenomena involved. [1,2]

One of the initial steps in this is to identify the major sources and sinks of atmospheric aerosols, the rates of their emission (and disappearance) and evaluate (accurately) their amount, composition, and distribution in the atmosphere. In the most general sense, aerosols are identified as those that originate from natural sources and human activity. Sea salt, windblown dust, volcanic emissions, and biomass burning are considered as the primary sources of natural aerosols, while industrial processes, transportation and waste disposal are considered major anthropogenic sources. Apart from being emitted from primary sources directly into the atmosphere, aerosols can be also formed *in situ* from gaseous precursors. These secondary aerosols are typically classified into several major groups according to their composition and abundance, such as sulfates, nitrates, or carbonaceous matter. In the year 2000, the total production rate of aerosol particles was estimated to be approximately 5975 Tg $year^{-1}$(see Table 1.1).[3] According to this compilation of data, around 93% (mass) of this amount is due to natural sources (primarily sea salt and mineral dust) and 7% due to human activity. It is also interesting to observe that while more than 98% of natural aerosols are primarily emitted directly in the atmosphere (as primary aerosols), the anthropogenic aerosols from primary sources and those formed *in situ* have comparable contribution (around 50-50%).

Table 1.1: Estimates for global production rates of particulate matter from natural and anthropogenic sources.[3]

Source type	Amount Tg/year
Natural sources	
Direct emissions	
Sea salt	3340
Mineral dust	2150
Biomass burning	60
Biogenic material	56
Subtotal	5606
Secondary production	
Sulfate	78
Nitrate	4
Hydrocarbons	16
Subtotal	98
Total natural	5704
Anthropogenic sources	
Direct emission	
Fossil fuel burning	35
Industrial dust	100
Subtotal	135
Secondary emission	
Sulfate	122
Nitrate	14
Hydrocarbons	1
Subtotal	137
Total anthropogenic	272
Sum total	5976

A vast majority of the particulate matter is found in the troposphere (a region located below 11 km altitude), with the concentration of aerosol particles further decreasing with increasing altitude. Although the areal distribution and the concentration of aerosols are strongly related to the proximity of sources (primary and secondary), they may also vary greatly due to a number of factors. For instance, the transport of aerosols via natural circulation (in the atmosphere), variation in the life-time of aerosols due to the difference in size and chemical composition or, in the case of secondary aerosols, the probability that the adequate reaction conditions are met for *in situ* formation. These are just some of the factors that contribute to the non-uniform distribution of aerosols, which is often difficult to predict.

Similarly, the composition of tropospheric aerosols may be very complex due to the multitude of sources and a variety of removal mechanisms. Furthermore, individual aerosol particles may consist of one or more chemical species, the exact composition being difficult to determine. For simplicity reason, they are often treated as equivalents or derivatives of the major aerosol species present in the atmosphere, such as sulfates, nitrates, volatile organics or black carbon. For some other purposes, however, it may be more useful to think of the atmospheric particles as belonging to one of the following categories: water soluble inorganic compounds, water insoluble inorganic compounds (minerals), and organic compounds.[3]

As can be seen from Table 1.1, sulfate aerosols represent a significant fraction of atmospheric (and subsequently tropospheric) aerosols. It is estimated that only around 5% of sulfate aerosols are directly emitted into the atmosphere while 95% formed *in situ* via gas-to-particle conversion from SO_2 as a precursor. Since SO_2 is the final oxidation product of all other sulfur gases in the atmosphere (which is further converted to sulfates SO_4^{2-}), sulfate aerosols represent the total load of all sulfur-based emissions into the atmosphere.

Table 1.2: Summary of natural sources of sulfur in the atmosphere (Tg year^{-1}) in 2000.[3]

Source	DMS	SO_2	Others (H_2S, CS_2, OCS)
Oceans	31-80.6	-	0.84-1.91
Costal wetlands	0.01-1.12	-	0.18-3.37
Soils and plants	0.19-1.49	-	0.13-1.91
Volcanoes	-	22.8-28.8	0.58-2.05
Biomass burning	-	7.78	0.04-0.26
Other	-	-	0.27-0.89
Sums	31.19-83.20	29.85-36.57	1.74-8.89

Table 1.2 shows relative contribution of major natural sources of sulfur in the atmosphere. [3] It can be seen that DMS, produced by marine phytoplankton and SO_2 from volcanoes and biomass burning are the largest contributors to the natural sulfur (loading) in the atmosphere. It should be noted that during volcanic eruptions the bulk of the gasses including SO_2 is ejected to the stratosphere, hence these emissions do not contribute significantly to the tropospheric load of sulfur.

On the other hand, anthropogenic aerosols and their precursors are emitted primarily into the troposphere and are thus concentrated predominantly around industrial and urban areas. The major anthropogenic sources and their contribution to the overall sulfur emission are summarized in Table 1.3.

Table 1.3: The most important sources of human-made sulfur emissions in 1976-1980.[3]

Source	Production and use (Tg $year^{-1}$)	Emission rate (Tg $year^{-1}$)	Percentage of total (higher limit)
Combustion of coal	3233	62-55.7	60.0
Combustion of petroleum and its products	6699.3	29.1-25.9	28.1
Smelting of nonferrous ores	25.1	10.7-6.8	10.4
Sulfuric acid	105.7	1.3-0	1.5
Pulp and paper	240.1	0.3-0	
Total emissions		103.4-88.4	

As it can be seen, sulfate aerosols represent about 45% of all man-made aerosols in the atmosphere (and most of the total sulfate load in the troposphere), with the industry, combustion and transportation being the largest contributors. Sulfate aerosols detected in the atmosphere contain H_2SO_4 and NH_4HSO_4, $(NH_4)_2SO_4$, $(NH_4)_3H(SO_4)_2$ (depending on the degree of sulfuric acid neutralization with ammonia). Sulfur gases in the atmosphere are oxidized to SO_2, to SO_4^{2-} and further converted into H_2SO_4. In the lower troposphere where there is a high concentration of NH_3, $(NH_4)_2SO_4$ is the dominant form of sulfate aerosol.

Ammonia ions in the troposphere result from a gas-to-particle conversion of NH_3. Three major sources are identified to contribute to the amount of ammonia in the atmosphere. It is estimated that about 20-35 Tg/year of ammonia worldwide comes from metabolic decomposition of organic waste like manure from livestock and wildlife.[3-5] Somewhere between 1.2 and 8.1 Tg/year of it is emitted by chemical industries (production of fertilizers and compounds used in the refrigeration system) and motor vehicles.[3] Finally, a significant amount of ammonia comes from the use of fertilizers in agriculture. Depending on the relative amounts of the SO_4^{-2} and NH_4^+ present in the atmosphere and the subsequent degree of neutralization, sulfate aerosols can occur in the form H_2SO_4, NH_4HSO_4 and $(NH_4)_2SO_4$, with ammonium sulfate estimated to be the most abundant form of sulfates in the lower troposphere.

1.2 Aerosols and Earth radiative balance

Tropospheric aerosols and, in particular, sulfate aerosols are known to play an important role in the Earth's energy balance.The Earth's radiative balance is determined by the relative magnitude of incoming and outgoing radiation fluxes to and from the planet. As shown in Fig. 1.1, about half of the incoming solar radiation passes though the atmosphere and reaches the Earth's surface where it is absorbed and radiated back to the atmosphere in the form of thermal radiation. Approximately 20% of the incoming sunlight is absorbed by the atmosphere (atmospheric gases), while the remaining 30% is reflected back into space (primarily by clouds, aerosols and atmosphere, and to lesser extent by Earth's surface). On its way up through the atmosphere, a large portion of the thermal radiation from the surface is absorbed by greenhouse gasses (water vapor, carbon dioxide, ozone) or reflected back by clouds and aerosols. The heat absorbed by the greenhouse gases can be re-emitted in all directions, however most of it is directed toward the Earth's surface rather than outer space, due to reflection by clouds (and aerosols). This phenomena, in which the thermal (infra red) radiation from the Earth's surface is literally trapped by the atmosphere leading to the warming of climate, is known as a greenhouse effect. The presence of aerosol particles can intensify or moderate this effect, depending on their size and composition and distribution in the atmosphere.

The first, most apparent effect of aerosols is that they influence the Earth's reflectivity directly, by absorbing and scattering incoming (short-wave) solar radiation and absorbing and re-emitting (long-wave) thermal radiation from the Earth's surface. Indirectly, they can change the microphysics of clouds by acting as cloud condensation nuclei, thus affecting cloud reflectivity (albedo) and lifetime. Both cloud albedo and lifetime strongly depend on the number, size and composition of present aerosols. For example, a large number of small particles lead to an increase in cloud albedo resulting in an increased cooling effect.[1,6-8]

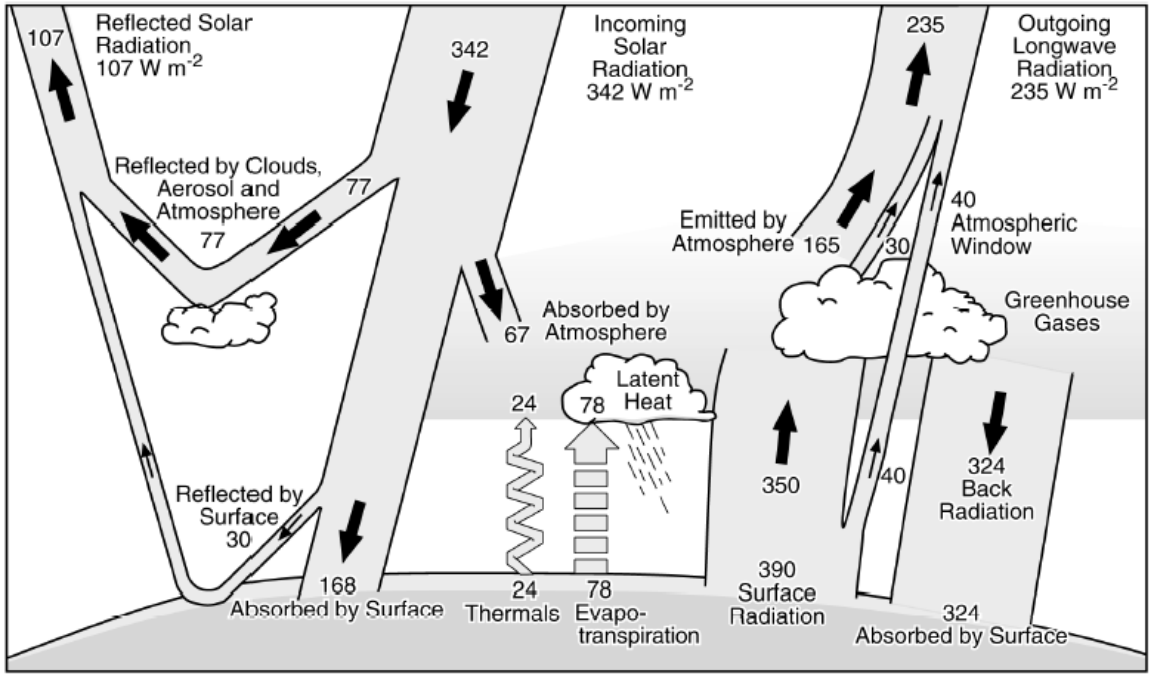

Figure 1.1: Earth's energy balance[9]

While the effect of the greenhouse gases on the Earth's energy balance has been acknowledged early on leading to intensive research in this field, the role and significance of atmospheric aerosols had not been fully recognized and understood initially. The major reasons for that was the lack of reliable information on their composition and abundance in the atmosphere, and the particular difficulties in quantifying their indirect effect. Nowadays, it has been estimated that the combined influence of aerosols has a net cooling effect on the Earth's atmosphere (as illustrated in Figure 2.2). Due to their high scattering activity and abundance, sulfate aerosols only are estimated to produce the cooling effect similar in magnitude but opposite in sign to the greenhouse effect.[10]

In addition, being a highly hygroscopic material, sulfate aerosols are very efficient as cloud nuclei.[11] As a matter of fact, it was partly due to the lack of understanding of this cooling aerosol effect that the full extent of the greenhouse warming has not been recognized earlier.

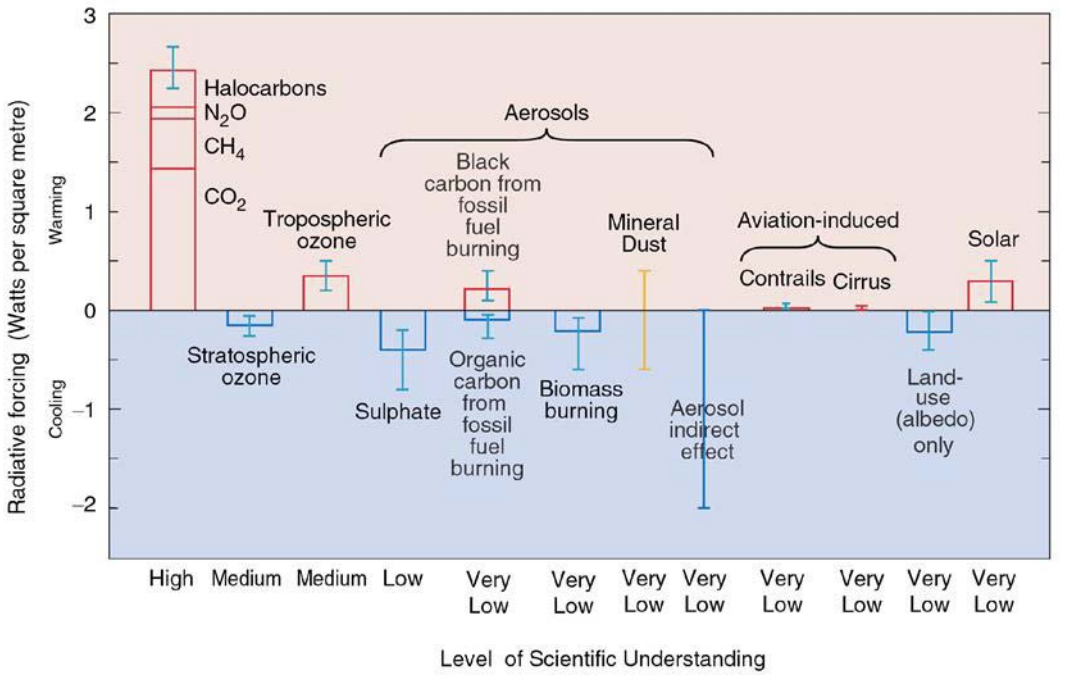

Figure 1.2: The global mean radiative forcing of the climate system for the year 2000, relative to 1750[12]

A better understanding of the complex role of the aerosol particles on climate requires a detailed knowledge on their abundance, physical properties and composition in the atmosphere. Current efforts are thus focused on two major fields: first, on developing better techniques for the remote sensing (detection and characterization *in situ*) of atmospheric aerosols and, second, on introducing more sophisticated atmospheric models that could accurately quantify the individual aerosol effects on the Earth's radiation budget.

1.3 Aerosol size distribution

Physical and chemical behavior of aerosol particles is strongly related to their size distribution. The knowledge of size distribution of airborne particles is important in understanding their deposition mechanisms and lifetime in the atmosphere. The majority of aerosol particles are polydisperse with a wide variety of sizes (0.01-10 μm radius), lifetimes (days and weeks) and concentrations (ranging from 10^2 particles/cm^3 in pristine to 10^5 particles/cm^3 in urban areas). In principle, monodisperse aerosols have a very short lifetime due to the particle tendency to coagulate and to grow by condensation. Size distribution parameter is thus an important factor in identifying the source of aerosols (when their composition is known), determining the contributions of various sources and estimating their regional and global transport.

The size distribution of aerosols represents the number of particles of a certain size in a cm^3 volume and the number density of aerosols is defined as the total number of particles per cm^3. Over time, various mathematical functions were proposed to characterize aerosol size distribution, however among them the log-normal distribution has been found to give the best fit to distribution shapes obtained for different sizes of well studied aerosols. The main characteristic of log-normal distribution is that when abscissa is given as log of particle diameter, the distribution exhibits a typical bell shape.

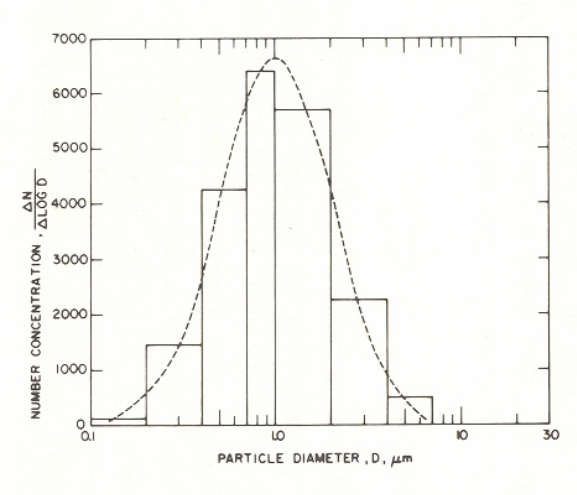

Figure 1.3: Relative number distribution histogram of a log-normal particle size distribution plotted on linear-log [13] .

A lognormal distribution can be characterized by two parameters: the geometric mean diameter, d_g, given by

$$\ln d_g = \frac{1}{N}\int_0^\infty (\ln d_p)\,dn \qquad \textbf{(1-1)}$$

and the geometric standard deviation, σ_g, defined by

$$\ln \sigma_g = \left[\frac{\int_0^\infty (\ln d_p - \ln d_g)^2\,dn}{N-1}\right], \qquad \textbf{(1-2)}$$

where N is the total number of particles and d_p is the diameter of the aerosol particle.

The cumulative function that describes the distribution is given by:

$$dN = \frac{N}{\ln \sigma_g \sqrt{2\pi}} \exp\left(-\frac{(\ln d_p - \ln d_g)^2}{2(\ln \sigma_g)^2}\right) d\ln d_p \qquad \textbf{(1-3)}$$

The short form of this function is:

$$dN = N(d_p)\,d\ln d_p \qquad \textbf{(1-4)}$$

where $N(d_p)$ is the total number of particles in the size interval d_p to $d_p + dd_p$.

It is well known that small particles (high number) contribute more to the number and surface distribution, and big particles contribute more to volume distribution. Therefore it is common practice to use the volume distribution to acquire more information about the particle size distribution when the sample contains a large number of small particles. Once the number of particles is known, the surface and volume are easily calculated by applying the following equations:

$$S(d_p) = N(d_p)\pi d_p^2 \qquad \textbf{(1-5)}$$

$$V(d_p) = N(d_p)\frac{\pi d_p^3}{6} \qquad \textbf{(1-6)}$$

where S and V are the total surface and volume of particles in the same size interval.[14]

1.4 Aerosols optical properties – Refractive index and Extinction

Among aerosol properties, light extinction is a key parameter in characterizing the radiative effect of atmospheric particles. Extinction, in the most general sense, refers to the attenuation of a light beam as it passes through a particle. When illuminated, particle can scatter and absorb light reducing the intensity of the incident light beam. Scattering describes the propagation of light through the interaction with a particle, during which light may change direction as the result of three separate processes: reflection, refraction and diffraction. The ability of a particle to absorb and scatter light is determined by its refractive index n^*, which is defined as the ratio of the light velocity in the suspending medium (air) to the velocity of light in a particle. For an absorbing material it is a complex number given as:

$$n^* = n(v) + ik(v) \qquad \textbf{(1-7)}$$

where the real part, *n(v)*, gives the aerosol scattering and the imaginary part, *k(v)*, gives the aerosol absorption. Although *n* and *k* are referred to as the optical constants, they should not be thought about as constants because they vary strongly with frequency.

The ratio of the light passing through the aerosol sample to the light incident on the aerosol is given by the Lambert-Beer law:

$$\frac{I}{I_0} = e^{(-\sigma_{ext} L)} \qquad \textbf{(1-8)}$$

where I_o is the intensity of light incident on the particle, σ_{ext} is the extinction coefficient and L is the path length of light. σ_{ext}, defined as a fractional loss in intensity per unit path length, is a function of the extinction efficiency of material, the size of the particle and the total number of particles in a sample.[6] The extinction coefficient can be expressed as:

$$\sigma_{ext} = N(\pi r^2 Q_{ext}), \qquad \textbf{(1-9)}$$

where N is the number of aerosol particles per cm^3, r is the particle radius and Q_{ext} the extinction efficiency. The $\pi r^2 Q_{ext}$ quantity in equation (1-9) is also known as the extinction cross-section of a particle.

The extinction efficiency is a dimensionless quantity which describes the ability of a particle to remove light from the incident beam. It is defined as

$$Q_{ext} = \frac{amount\ of\ light\ removed\ \ through\ \ scattering\ and\ absorption\ \ by\ a\ particle}{amount\ of\ \ incident\ light}$$

and hence, it is a function of scattering efficiency Q_{scatt} and absorption efficiency Q_{abs}. In the case when a particle is suspended in a non-absorbing medium, the extinction efficiency is simply a sum of the scattering and absorption efficiency.

$$Q_{ext} = Q_{scatt} + Q_{abs} \qquad \textbf{(1-10)}$$

While absorption efficiency is a unique property of a material which can be determined experimentally by measuring the absorption coefficient, scattering efficiency can only be determined through calculations (computation).Calculating extinction efficiency is not simple, since it is a complex function of the particle size, the wavelength of the incident light, and the optical properties of the suspended material and the surrounding medium. Depending on the particle size and how it correlates with the radiation wavelength, three different scattering regimes are identified and the corresponding theories used to calculate scattering of the particle. To distinguish these regimes a non-dimensional parameter α is introduced, defined as a ratio of the characteristic dimension of a particle and the wavenumber ν

$$\alpha = 2\pi r\nu \qquad \textbf{(1-11)}$$

In the case of small particles, *i.e.* when $\alpha << 1$, scattering is described by Rayleigh theory. On the other hand, for big particles, geometric optics theory can be readily applied to calculate scattering intensity and pattern. For $\alpha \sim 1$, no simple analytic form can be used to calculate. In the case of a spherical particle and single scattering only, the solution to Maxwell's equations for the interaction of an electro-magnetic wave with an isotropic, homogeneous particle can be greatly simplified.

This solution, also better known as Mie theory, is hence used to calculate the scattering pattern and intensity of spherical particles in so-called Mie scattering regime. In particular, Mie provided the solutions for the calculation of the extinction and scattering cross-sections,

$$K_{ext} = \frac{2\pi}{k^2}\sum_{n=1}^{\infty}(2n+1)\mathrm{Re}\{a_n + b_n\} \quad \textbf{(1-12)}$$

$$K_{sca} = \frac{2\pi}{k^2}\sum_{n=1}^{\infty}(2n+1)\left(|a_n|^2 + |b_n|^2\right) \quad \textbf{(1-13)}$$

$$k = \frac{2\pi n_0}{\lambda} \quad \textbf{(1-14)}$$

where $K_{ext} = \pi r^2 Q_{ext}$ and $K_{sca} = \pi r^2 Q_{sca}$ are extinction and scattering cross-section respectively, n refractive index of the particle, n_0 refractive index of the medium and $a_n(n, n_0, v)$ and $b_n(n, n_0, v)$ the scattering coefficients which are complex functions of the refractive indexes of the particle and the medium, and the size parameter.[15]

The difference in these scattering patterns among the particles of different sizes is illustrated in Figure 1.4. In practice, a direct consequence of this is that extinction by airborne particles may vary greatly with their composition and size. For instance, in the case of small aerosol particles (r < 0.025 μm) extinction efficiency is strongly dependent on their size, decreasing rapidly with decreasing radius (since according to the Rayleigh theory $Q_{ext} \propto r^4$), whereas for big particles (r > 2 μm), Q_{ext} has an oscillating pattern which attenuates with increasing particle radius, approaching the limiting value of 2 for very large particles.[6] For the particles in the 0.0025<r<2 μm range, Q_{ext} has complex dependence and can be extracted from graphs or obtained by computer-aided calculation.

Figure 1.4: Examples of the scattering pattern from three different sizes of aerosol particles [16]

As already mentioned, the theories discussed above are used to calculate scattering pattern and extinction of a single particle of a certain size. In the case of multi-disperse aerosols, the total spectral extinction can be calculated by integrating the extinction cross-section over all particle sizes:

$$\tau(\lambda) = \int_r K_{ext}[r, n(\lambda, C)]P(r)dr \qquad \textbf{(1-15)}$$

where C is the aerosol composition and $P(r)$ is the particle size probability distribution function. As it will be discussed in more detail in Chapter 2, in this study we have used this method extensively to calculate and fit experimental extinction spectra of aerosol particles. Since the particles used in this work were spherical and well within the Mie scattering regime, the extinction cross-section K_{ext} in eq. (1-12) was calculated according to Mie theory.

1.5 Deliquescence and efflorescence

A vast majority of atmospheric aerosols contain hygroscopic and water soluble compounds. The hygroscopic properties of such airborne particles are directly or indirectly involved in a number of processes and phenomena in atmosphere and nature, from their effect on the visibility, formation of clouds, and radiative forcing, to their influence on chemical reactivity and biochemical cycles in nature.

Suspended in the air with a variable amount of water vapor, water soluble atmospheric aerosols are subjected to two distinct physical processes with respect to the ambient humidity, deliquescence and efflorescence.[8,17-24] In the most general sense, deliquescence is the process of water uptake and dissolution of a solid particle in humid air. Efflorescence describes the opposite process, in which a liquid aerosol particle (i.e. solution droplet) loses water and crystallizes when exposed to dry air. In reality, this cycle of dissolution and precipitation of a solid particle with changing humidity contains several distinct steps as depicted in Figure 1.5.

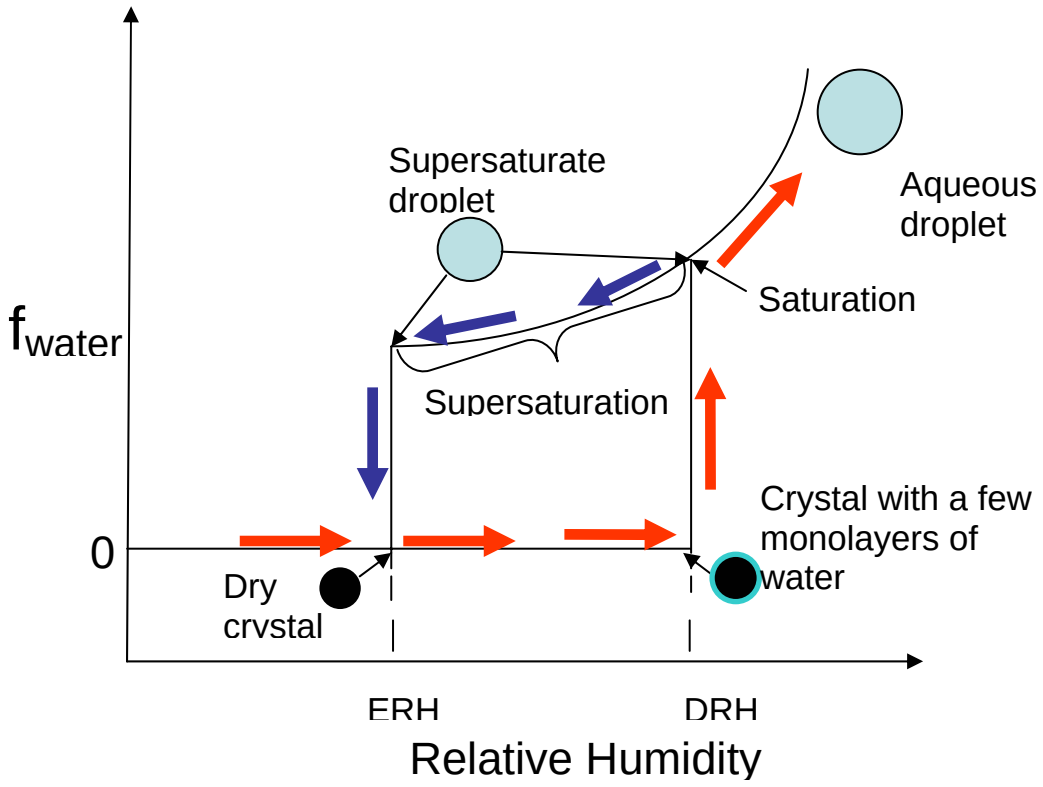

Figure 1.5: Humidogram of a hygroscopic aerosol particle

Basically, during the humidification process (presented by a red line in Figure 1.5) a dry aerosol particle uptakes water forming, initially, a crystalline core covered by adsorbed water molecules. Under the conditions of increasing humidity, the water "film" can grow up to a few monolayers of water. For instance, the IR study of the water uptake on NaCl crystals particles indicates that at relative humidities (RH) of 70%, these particles are coated with approximately 4 monolayers of water.[25]At certain RH, also known as the deliquescence relative humidity (DRH), the crystal core abruptly dissolves into the water layers forming a saturated droplet.

This particular step in which a particle undergoes phase transition from solid to liquid is known as deliquescence. At this point Gibbs free energy for the dry particle becomes greater than Gibbs free energy for a dissolved salt droplet, making the process of phase transition thermodynamically favorable.[24] When the saturated liquid droplet is in equilibrium with the ambient relative humidity, the DRH corresponds to the vapor pressure of the saturated salt solution.

For some typical atmospheric aerosol compounds such as NH_4NO_3, NaCl and $(NH_4)_2SO_4$, these DRH at which solid particles convert into saturated liquid droplets are around 62%, 75%, and 80% respectively. Since the deliquescence process is characterized by the uptake of water molecules into the droplet, it is accompanied by an apparent increase in the particle mass and volume.[8,24] As the ambient relative humidity increases further to values larger than DRH, the droplet takes up more water and continues to grow by condensation, becoming more dilute. The growth stops once the particle is in equilibrium with the surroundings. As mentioned, these humidification steps are characterized by particle growth which, in some cases, can be significant. In the case of ammonium sulfate, the deliquescence curve of which is shown in Fig. 1.5, the growth factor (ratio of droplet diameter to "dry" crystalline particle diameter) during the deliquescence step only is around 1.5, corresponding to the increase in the particle volume by a factor of around 3.3. As expected, further dilution of liquid particles results in even larger growth factors. For instance, when a solid ammonium sulfate particle is exposed to humidities around 97.1% it will result in the formation of a diluted droplet (10 % wt $(NH_4)_2SO_4$) and the growth factor is more than 2.5. This corresponds to an almost 17-fold increase in volume, relative to the initial solid particle.

The dehumidification process or "drying" of a liquid particle is represented in Fig. 1.5 by a blue line. When subjected to lower relative humidities, the aqueous diluted particle gradually loses water and becomes more concentrated. The concentration of the droplet solution continues even beyond the saturation point, DRH. Once the relative humidity decreases below DRH, the liquid droplet becomes a supersaturated solution due to water evaporation and remains in liquid state down to efflorescence point, ERH. At the efflorescence point, as the particle reaches critical supersaturation, homogeneous crystallization occurs almost instantaneously. At this point Gibbs free energy for a dry particle is lower than Gibbs free energy for a supersaturated droplet, resulting in spontaneous phase transition.

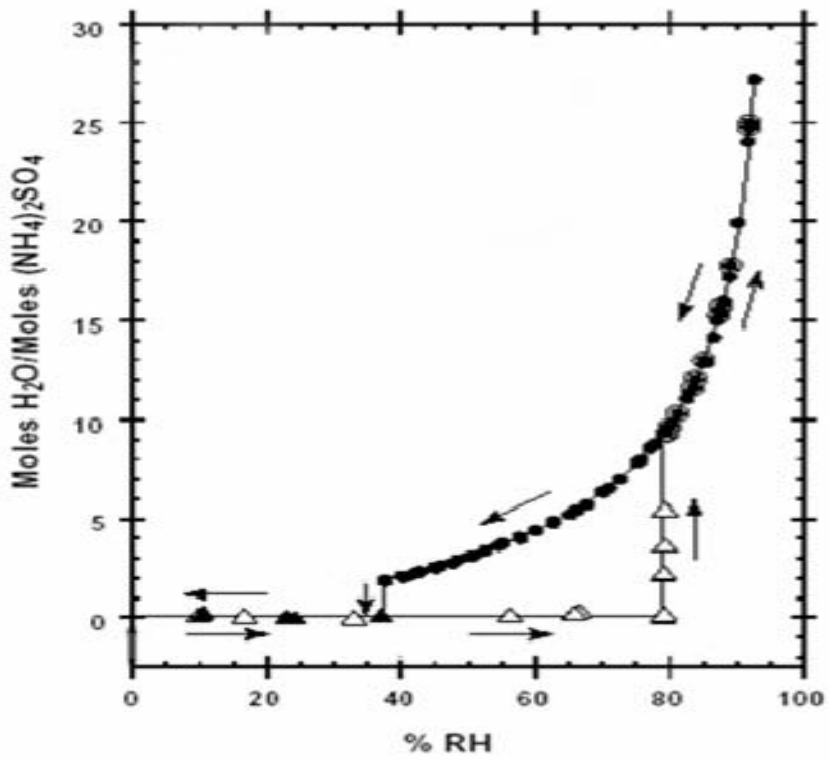

Figure 1.6 Ammonium sulfate humidification and dehumidification cycle at 25^{0}C, reproduced from Tang and Munkelvitz. Open symbols correspond to the growth (humidification) phase and filled ones to the evaporation (dehumidification).[26]

While figures 1.5 and 1.6 show the deliquescence and efflorescence processes of pure water soluble compounds, atmospheric aerosol particles may often contain one or more components, internally or externally mixed. In the case of an inorganic salt mixture, aerosol particles start to take up water and grow at so-called mutual deliquescence relative humidity (MDRH), which is lower than the DRH of individual pure component present in the mixture.[8,27,28] Therefore, the growth profile of multi-component aerosols is missing the sharp transition from solid to liquid. For particles coated with hydrophobic compounds, an increase in deliquescence RH is noticed because the coating offsets the dissolution of the solid core. Internally mixed aerosols containing inorganic salts and water soluble organics, however, deliquesce at RH <DRH $_{salt}$. This implies that the organic fraction is responsible for the water uptake at humidities lower that the DRH of the pure inorganic salt.[29]

In general, humidification and drying of hygroscopic aerosols exhibits a hystersis effect, with deliquescence and efflorescence occurring at different relative humidities or different ranges of humidities, in the case of mixed aerosols. The direct consequence of this is that in the region between the ERH and DRH aerosols could be present either as "dry" particles or supersaturated droplets, depending on their history. As shown by Figure 1.6 in the case of ammonium sulfate, depending on the conditions, particles can occur either as solid or supersaturated liquid droplets in the range between 37 and 80% RH. The ambient relative humidity and its time profile thus dictate the phase and the composition of hygroscopic atmospheric aerosols.

As discussed, these transformations are accompanied by changes in aerosol volume and composition which have strong effect on aerosol scattering properties and, subsequently, their impact on many atmospheric phenomena including climate forcing.[30]

Chapter Two: Determination of the composition, size distribution and optical properties of aerosols

2.1 Introduction

Experimental studies on aerosols often require that many (if not all) of its properties be well known, such as number density, size distribution, chemical composition, or shape and morphology of particles. There are numerous methods available to characterize aerosols which exploit different properties of particles, often physical (mechanical and optical) and electrical. One of the most straightforward ways to determine aerosol size distribution is by collecting and analyzing particles. The majority of particle sizing instruments utilize mechanical (inertial and diffusional) mobility of particles, their electrical mobility or the combination of the two, all of which are functions of particle size.

Inertial collectors (e.g. cyclones and impactors) and diffusional collectors (such as diffusion battery), both typically used in cascade, classify particles according to their size with each stage collecting particles smaller than in the previous one. Electrical mobility type instruments such as differential mobility analyzers separate (charged) particles based on their different mobility in an electric field. By varying the electric field and thus changing the mobility of particles, different particle sizes can be sampled out from the aerosol flow. What all these methods have in common is that they allow separation of particles within a narrow mobility range, which can be collected on filters and screens and subsequently analyzed. Depending on the particular information of interest, collected aerosols can be subjected to conventional chemical, gravimetric, spectroscopic (e.g. FTIR) and microscopic analysis (SEM, TEM, AFM etc.) to obtain detailed information on aerosols, from the chemical composition to the size, size distribution, shape and morphology of particles. Such comprehensive ways of analyzing aerosols is reliable and may provide a variety of information on the aerosol properties and as such is often used as a standard against which other indirect methods are verified. A major disadvantage of it is that it is a time consuming, off-line and invasive way of characterizing aerosols.

Often there is no need for most of the aerosols properties to be known in real time, but only information on the one or two properties of interest (i.e. size distribution or composition of aerosols). For that purpose a number of direct reading instruments have been developed. They are typically equipped with detectors which can count or in some other indirect way quantify particles in a flow. One such type of particle detector is a collection electrode connected to an electrometer, which can quantify the number of charged particles deposited on its surface. It is one of the principal components of DMS (differential mobility spectrometer). Basically, DMS is a DMA equipped with a series of collection electrodes distributed along the annular space through which the charged aerosol flow is passed. Since particles with different sizes have different electrical mobilities and trajectories, monodisperse fractions of aerosol particles will be collected and detected simultaneously on individual electrodes.

Another type of detector commonly used for continuous particle sizing is optical detector, which utilizes the property of aerosols to scatter light when illuminated by a light beam. The light scattered by a particle which is, as discussed in Section 1.4, a complex function of a particle size, can be easily converted to an electronic pulse and provide information on the number and, potentially, size and size distribution of particles. While there are techniques which, in particular, use the scattering pattern to deduce the particle size and even image particles (such as dynamic light scattering) there are simpler ways to quantify aerosols by combining this scattering property of aerosols with their mechanical mobility. Aerodynamic Particle Sizer by TSI (APS) is an example of such an instrument. There, aerosol flow is accelerated through a nozzle resulting in larger particles exhibiting lower velocities due to inertia. The velocity of the particles is determined by measuring their time-of-flight between two laser beams, where the time-of-flight corresponds to the time difference between the two electrical pulses generated by a particle passing the laser beams.

These are just some of many commonly used fast-response methods for qualitative characterization of aerosols. Many of them are simple, inexpensive and commercially available. The situation is somewhat different, however, with the instruments for qualitative characterization of aerosols in real-time.

There are not many simple methods available for determination of chemical composition of aerosols in real time. Most of them are based on some type of mass spectrometry, preceded by the particle evaporation and ionization step. Although mass spectrometry is a versatile technique which allows both qualitative and quantitative analysis of aerosols in continuous (or semi-continuous) manner, it is also an expensive and intrusive technique. However, recently, novel noninvasive methods have been developed for simultaneous characterization of aerosol composition and size distribution *in situ*. They utilize the aerosol property to extinct light and its high sensitivity to particle size and optical property of material (see Section 1.4). This indirect method relies on the calculation of the extinction spectrum of aerosol particles and finding the best fit to the experimental spectrum. When the optical properties of the material are known, the solution that generates the best fit provides the information on the particle size distribution.

In the case of multi-component aerosols, provided the optical properties of all components and/or phases are available, both the composition of the aerosol and the size distribution of each component can be retrieved. The basic principle of this method can be also used in reverse fashion.

By finding (iteratively) the best fit to the experimental spectrum of an aerosol sample with known composition, optical properties (optical constants) of the aerosol material can be determined. The major advantage of this method is that it allows on-line qualitative and quantitative characterization of aerosols without any (or with minimal) disturbance to the aerosol flow. The main limitation of it is that it can be used only if reliable optical constants for all components are available. As discussed in more detail in the following sections, in this work we have tested and used these, so-called inversion methods to qualitatively and quantitatively characterize aerosols and derive optical constants of aerosol materials.

Finally, there is another convenient method for the characterization of aerosol chemical composition *in situ* that was used in this work that should be also mentioned here.

In case when aerosol particles are in equilibrium with the surrounding medium (essentially humid air), their composition can be indirectly determined using thermodynamic models, most notably Aerosol Inorganics Model (AIM) by Clegg et al., nowadays also available on-line. By simply monitoring ambient conditions of aerosols such as temperature and humidity, and knowing the initial composition of aerosol mixture, the final, equilibrated composition and phase of aerosols can be determined.

As it will be shown in Chapter 6, we used this method to determine the composition of equilibrated ammonium sulfate solution aerosols in optical constant studies. In addition to AIM, more specialized thermodynamic models have been developed and published recently, such as ADDEM (Aerosol Diameter Dependent Equilibrium Model) by Topping et al.[31,32] Apart from determining the aerosol composition, the model allows that the size of growing, deliquescing particles to be predicted, starting from some initially given size of dry aerosol. Although these methods provide a very useful tool for studying aerosols, their major restrictions are that they are applicable under limiting circumstances, that is when aerosols are in or approximately near equilibrium. In addition, their predictive ability has been so far limited only to soluble inorganic compounds.

2.2 Retrieval of aerosol size distribution and composition from IR extinction spectra (using the inversion method)

2.2.1 Determination of aerosol number density and size distribution

In this method, experimental extinction spectra are used to determine size and number density of aerosol particles. The inversion procedure, developed previously in our laboratory by Zasetsy, involves the least square fitting of a basis set of spectra to the experimentally recorded spectrum. In the simplest case of one-component aerosols, the basis sets are the extinction spectra for all discrete aerosol sizes considered to be present in the aerosol sample. An example of such a basis set extinction spectra for solid AMS particles is shown in Figure 2.1. The iterative procedure, with a minimization function χ shown by Eq. (2-1), is repeated until the best fit to the experimental spectrum is obtained.

$$\chi = \min[\left|K \cdot P - \tau_{\text{ext}} + \gamma \cdot S \cdot P\right|^2]^{1/2} \text{ 33-35} \qquad \textbf{(2-1)}$$

In the above equation, **K** is a $m \times n$ matrix, where m is the number of frequencies at which extinction is calculated in a spectrum and n the number of discrete radii, composed of the aerosol extinction spectra. The element of the **K** matrix is the extinction cross section $K_{i,j}$. Thus, columns of the matrix **K** are the extinction spectra for a set of particle sizes (radii). Mie theory for spherical particles is used to calculate the extinction spectra for a number of discrete radii in the range of 0.05 to11.88 microns at wavenumbers between 6000 and 500 cm^{-1}. The accuracy of the calculated reference spectra is limited only by the uncertainty of the indices of refractions because Mie calculations can be extended to arbitrarily high levels of accuracy. (This range of particle size was chosen because it covers the sizes of particles that give significant light scattering in the frequency range of interest.) Further, τ_{ext} is the extinction experimental spectrum used to retrieve the aerosol number and size distribution. **P** is the solution vector giving the particle size distribution, normalized by the total volume of the sample. (The total volume density is obtained using the path length of the sample and summing over the component **P**.) This approach does not put any limitation on the shape of the distribution; it can be applied successfully to retrieve multimodal size distributions.

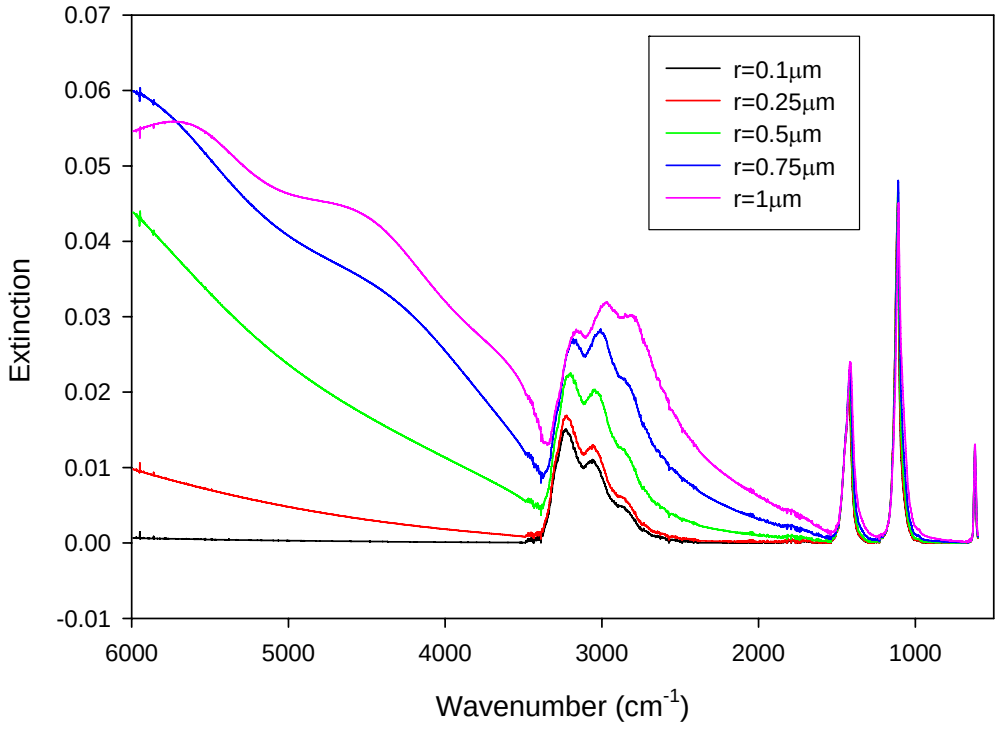

Figure 2.1: An example of basis set extinction spectra for selected particle sizes in the range between 0.1 and 1 μ for solid $(NH_4)_2SO_4$. (Note: these are derived from our new set of optical constants for solid AMS in this study)

The solution vector **P** is subjected to two main constraints. First, we apply the smoothness constraint to the size distribution. Smoothness can be governed by a smoothing factor γ and when no smoothing is applied, i.e. γ = 0, the computed size distribution has sharp features due to the fact that extinction does not vary much with size in the case of small particles. A more realistic, smoother distribution is obtained by increasing γ without affecting the goodness of the fit. In the least square procedure (Eq. 2-1) **S** is a $(m-3)\times m$ matrix used to minimize the third differences of vector **P**, thus imposing the smoothness constraint on the size distribution. Next, to assure that all computed spectral intensities are either positive or zero the minimization problem is subjected to the second non-negativity constraint, that is $\mathbf{1}\cdot\mathbf{P}\geq\mathbf{0}$.

In practice, the influence of the smoothing value on the extinction spectrum's fit have been studied by colleagues in our laboratory and it has been found that the goodness of fit, χ^2, does not change significantly for a range of γ values. This leads to difficulties in selecting the smoothness that provides the smallest difference between the experimental and retrieved spectrum, just by looking (visual inspection of) at the spectra. The optimal value of the smoothing factor for the best fit occurs at the point where χ^2 begins to increase sharply with increasing γ value. For systems in which the particles are in equilibrium with the surroundings, this point coincides with the point of maximum entropy giving us the confidence to assure that the computed size distribution using the optimal smoothing factor is the actual equilibrium size distribution of aerosols. Hence the highest amount of smoothness that still provides the same goodness of the fit value is used. The procedure we are using gives us the option to specify the allowed increase in χ^2. In the first iteration it assumes $\gamma = 0$, and calculates the spectrum corresponding to a first guess size distribution and compares it with the experimental extinction spectrum, χ_0^2. γ is then incrementally increased and χ_i^2 (where i is iteration index) is computed for this particular γ value. The procedure stops when the difference between χ_i^2 and χ_0^2 exceeds some specified value for the increase in χ^2, typically on the order of a few percent (1-2%).

The output of the program is given in the form of normalized size distribution and total volume of aerosols, which can be easily converted to the corresponding number (or surface) distribution and the total number density. The shape of the size distribution and the number of modes in the sample are determined from the best fit to the experimental spectrum. As shown and discussed in Chapter 5, we have tested and verified the applicability of this method against other conventional sizing techniques.

2.2.2 Determination of aerosol composition

This inversion method was extended further to multicomponent aerosol systems to determine their composition, phase and size distribution. Provided the basis spectra for all components likely to be present in the sample are available and assuming the aerosol spectral contributions are additive (*i.e.* homogeneous particles and single scattering), the $\mathbf{K} \cdot \mathbf{P}$ term can be represented as:

$$K \cdot P = \left(K_{ext}^{1}, K_{ext}^{2}, \ldots K_{ext}^{N}\right) \cdot \left(p^{1}, p^{2}, \ldots p^{N}\right)^{T} \qquad \textbf{(2-2)}$$

where $\mathbf{K}_{ext}^{i}$ is again a $m \times n$ matrix representing each component, N the number of components in the aerosol and p^{i} is the m-length vector of coefficients that can be used to solve Eq. (2-1). The spectrum is fitted with respect to all basis sets available, and the best fit and distribution of each component is retrieved. Providing the density of the materials in question is known, the relative contribution of each component can be determined from its volume fraction, and the composition of the aerosol determined. As it will be shown in Chapter 6, we have used this tool to deduce the composition of mixed aerosols, such as those containing both solid and deliquesced AMS.

2.3 Determination of complex index of refraction of aerosols (using the inversion method)

Determination of complex indices of refraction for crystalline AMS

The new indices of refraction reported in this study in Chapters 4 and 6 were derived using the iterative method originally proposed by Clapp et al.[36] It is based on the determination of complex refractive indices from aerosol (IR) extinction measurements and the particular implementation used in this work was described previously in detail by Zasetsky et al.[35] The basic algorithm of this numerical procedure is summarized and shown in Figure 2.2.

Briefly, as discussed in section 1.4 the complex refractive indices are given in the form:

$$n^*(\nu) = n(\nu) + ik(\nu) \quad \textbf{(2-3)}$$

where n and k are the frequency-dependent real and imaginary components, respectively. In the first step, the iterative procedure requires an initial guess, (k_0), for the imaginary component, k, typically obtained from a small particle (experimental extinction) spectrum, $\alpha_{abs}(\nu)$, for which the scattering amplitude may be considered negligible. The initial guess for the imaginary part is calculated as:

$$k_{0(\nu)} \approx \frac{\alpha_{abs}(\nu)}{\nu} \quad \textbf{(2-4)}$$

and $k(\nu)$ scaled linearly by the scaling coefficient $,1+\Delta k$, where Δk is a varied increment in k :

$$k_{(\nu)} = (1+\Delta k)k_{o(\nu)} \quad \textbf{(2-5)}$$

A subtractive Kramers-Kronig transform, given by Eq. (2-6) is then performed to calculate the real component, $n(\nu)$, for the newly determined $k(\nu)$ value.

$$n(\nu_i) = n_\infty + \frac{2P}{\pi}\int_0^\infty \frac{\nu \cdot k(\nu)}{\nu_i{}^2 - \nu^2} d\nu \quad \textbf{(2-6)}$$

The transform also requires the "anchor point", which is the real component of the refractive index at infinite frequency, n_∞. For instance, for solid ammonium sulphate the index of refractions at the anchor point, n_∞ , is 1.528 measured at 550 nm.[2] In this particular case, the point is considered to be at infinite frequency since it is far enough from the IR experimental range used in the study and ammonium sulphate has no absorption bands at this wavelength. The iteration procedure stops when the increment Δk is smaller than an initially set small value.

The newly derived set of optical constants $n^*(\nu)$ and Mie theory are then used to calculate monodisperse extinction spectra for 96 discrete radii between 0.05 and 11.88 μm over the 500-6000 cm^{-1} frequency range, as described in Section 2.2. These size and wavelength limits were chosen to cover the frequency and size range within which the scattered intensity is most sensitive. These calculated extinction spectra, which we refer to as the spectral basis set, are then fitted to the experimental spectrum using a linear least-squares method. The amplitudes of the monodisperse spectrum that produce the best fit constitute the size distribution for the sample.[34] The initial guess for the imaginary component is then varied, a new real component calculated and the procedure repeated in a systematic way until the best fit is obtained between the experimental and calculated spectrum. Any remaining, small-scale discrepancies between the experimental and calculated spectra are reconciled by correcting *k* by a small amount at each frequency and repeating the steps described above. The final solution is a set of scaled and corrected optical constants that provide the best fit of the experimental data within the set accuracies.

As it will be discussed in Chapters 4 and 6, we utilized this method to derive complex indices of refraction for solid AMS and the range of the compositions of AMS solutions and subsequently used them in the retrieval method to characterize aerosols in this study.

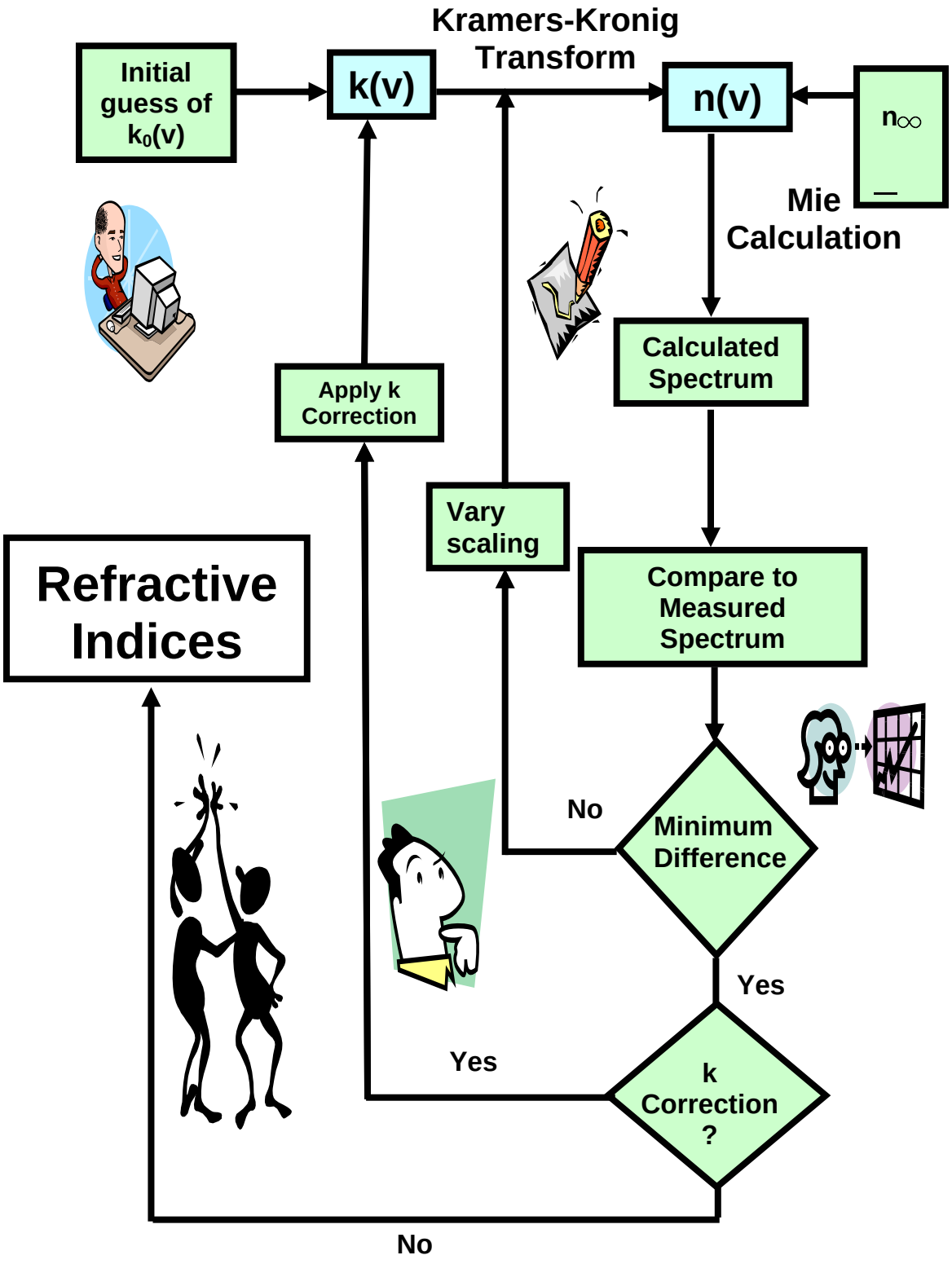

Figure 2.2: Flow chart depicting inversion procedure

Chapter three: General experimental

3.1 Introduction

In general, an experimental set up for aerosol studies typically consists of a few major components: a unit for aerosol generation, a detection (or collection) unit, and a system of chambers or flow tubes for conditioning (humidification, drying, cooling) and reacting of aerosol. As it will be shown in the following Chapters, in the course of this work several different types of experiments were done to study the optical and hygroscopic properties of ammonium sulfate aerosol, as well as the kinetics of its deliquescence. For that purpose different experimental set ups were used and the specifics of each of them are given in the chapters devoted to the particular study. All these experimental designs, however, are based on a very similar principle and have many elements in common. In this chapter we describe the major, common components of the experimental set ups used throughout this work and basic principles of their operation.

3.2 Aerosol Generation

Several different types of aerosol generators were tested and used in the course of this work. Here is a brief overview and general recommendations on the aerosol production methods we adopted and experimented with in the preparation for this study.

3.2.1 Constant Output Atomizer

The Constant Output Atomizer (by TSI Inc., model 3076) is one of the most commonly used aerosol generators in aerosol particle studies.[37] The operational principle of the atomizer is based on the mechanical dispersion of liquid into droplets. Fig.3.1 is a schematic of the cross-section of the Atomizer Assembly Block. Compressed carrier gas (typically N_2) impinges onto the 0.9 cm diameter platinum disc with a 0.03429 cm diameter hole, generating a high velocity jet. A region of low pressure is created by the jet, drawing liquid from the reservoir into a vertical passage in the atomizer block. In the atomizing region, the jet breaks the liquid into small droplets.

Due to their momentum, large droplets collide with the wall situated in front of the jet and the resulting liquid is drained back into the reservoir, whereas the remaining small liquid particles are carried by the gas out of the atomizer through 1.25 cm i.d. stainless steal tubing. The use of a backing pressure in the 25 to 35 PSI range produces aerosol flow rates between 2.7 and 3.3 standard liters per minute. The atomizer produces aerosols with a fairly stable size distribution and number density, of approximately 2×10^6 particles/cm^3. It generates submicron droplets with a lognormal size distribution and the mean diameter of 0.3 μm and standard deviation smaller than 2. Producing crystalline particles thus require an additional drying step, typically achieved by using a silica gel unit or some other types of a drier (see Section 3.4.1.1). Since the solid particles are generated from solution, their size can be varied by using solutions of different concentrations.

From our own experience, the constant output atomizer was found to be very efficient for the production of small aerosols using diluted salt solution. When more concentrated solutions were used to generate bigger aerosols, the atomizer showed a tendency to clog up frequently (jeopardizing the continuity of experiments). Clogging of the atomizer results in a blockage of the flow and in a variable output. This is most likely a consequence of the significant temperature drop in the expansion region, which causes the precipitation of salt from solution and its buildup on the platinum orifice. We tried to solve the clogging problem in several ways. The first idea was to try to do it by increasing the temperature of the atomizer and, hence, the solubility of the salt in the solution. We did several attempts by heating different regions of the atomizer. For instance, by heating exclusively the atomizing region (by wrapping the atomizer with a heating tape), or pre-heating the compressed gas (by passing the gas through a heated cooper coil), or heating the entire solution in the atomizer bottle (by placing it in a hot bath). None of these attempts worked although the temperature of the elements or even the whole system was raised by more than 10 to 15^0C.

The clogging problem was partly solved by using pre-humidified nitrogen as the compressed gas. This modification allowed longer operation times of the atomizer between cloggings, but it did not completely solve the problem. This production method was therefore employed only in the experiments when working with low concentration salt solutions, otherwise a nebulizer was used.

Another limitation of this device that should be pointed out is that the carrier gas and aerosol flow rate can be varied only over a narrow range (around 3±0.3 l/min) limiting the variation of the residence times that can be used.

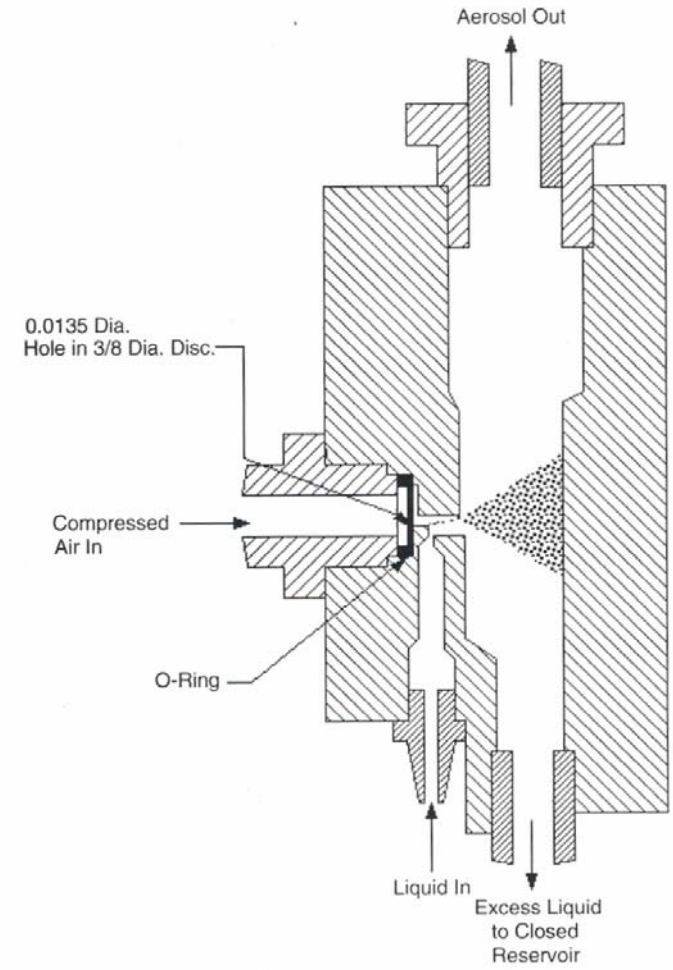

Figure 3.1: Model 3076 schematic of the atomizer assembly block[37]

3.2.2 Ultrasonic Nebulizer

The Large-Volume Ultrasonic Nebulizer (DeVilbiss, Ultra-Neb 99) is another commonly used type of aerosol generator. The piezoelectric transducer of the Ultrasonic Nebulizer is located at the bottom of the nebulizer chamber, which is filled with salt solution. Vibrations transmitted to the liquid in the nebulizer chamber cause cavitations in the surface layer and separation of droplets from the bulk.

A flow of nitrogen gas is passed over the solution surface and carries the newly formed droplets out of the nebulizer chamber. The size of the aerosols produced by this nebulizer ranges from 0.5μm to 10 μm. Aerosol number density can be controlled by varying the voltage applied to the transducer and by adjusting the flow rate of the carrier gas. To obtain a fairly stable number and size distribution it is necessary to maintain a constant level of liquid in the nebulizer chamber. This can be achieved by using a continuous feed system that is supplied with the nebulizer. It should be also noted that when the nebulizer is turned on, due to the energy transfer the solution warms up to 40^0C and it takes about half an hour for the system to reach a steady state. The ultrasonic nebulizer has a high aerosol output (6 ml/s for water aerosol) and, as will be also discussed in Section 3.4.1.1 it can be successfully used in conjunction with a silica gel dryer. When Nafion dryer is used, the high output of the nebulizer is a draw back. Due to its limiting capacity to remove water, Nafion membrane saturates and collapses within a few minutes of operation. In principle, this problem can be solved by splitting and using only a fraction of the output. Finding the most optimal configuration and calibrating it for variable aerosol flow rate, however, proved to be time consuming. For the generation of large particles we thus opted for a more flexible Burgener nebulizer, described in the next section.

3.2.3 Burgener Nebulizer

The Mira Mist Nebulizer, shown in Figure 3.2, operates using a compressed gas (typically nitrogen). It contains a solution line connected to a sample capillary tube and a gas line, parallel to the capillary tube, encapsulated in a Teflon body. Liquid sample, stored in ordinary flasks, is fed into the nebulizer lines by Peristaltic pumps (Instech, P720).[38] At the tip of the nebulizer the solution is atomized by the high velocity gas.

A convenient feature of the design shown in Figure 3.2 is that the larger opening at the tip of the sample path prevents clogging even when working with highly concentrated salt solutions.[39] A backing pressure of around 45-55 PSI is necessary to generate an aerosol flow rate of 1 l/min. The number density of produced aerosols is controlled by the pump speed, diameter of silicone pump tubing and orientation of the nebulizer.

Since the stability of the output depends greatly on the quality of the silicone tubing, the tubing (which deteriorates fast with frequent usage) should be replaced periodically. The generated particle size depends on the concentration of the sample, and in our experiments, in particular, ranged between 0.1 and to 6 μm in radius.

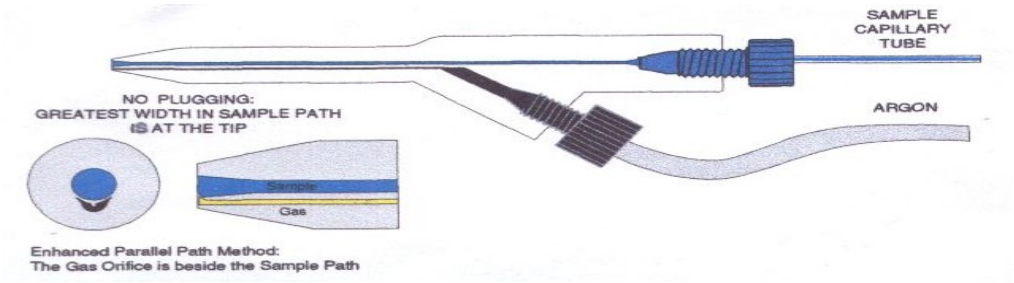

Figure 3.2: Cross-section of the Mira Mist Nebulizer body and tip[39].

To use the nebulizer optimally in our experiments, we designed a special inlet with a multiple purpose: to hold the nebuliser in horizontal position, provide an inlet for an additional gas line and allow drainage of excess liquid. The inlet is basically a horizontal glass pipe with a 45° side arm facing downward, both 3.8 cm inner diameter. The nebulizer body is held inside the horizontal part of the glass pipe by a custom-made stainless steal fitting. The fitting is equipped with an inlet for carrier gas, which is introduced from the back and around the nebulizer with minimal disturbance to the aerosol flow. Introduction of the additional gas flow thus allows the aerosol flow rate and its residence time in the reactor to be varied independently of the backing pressure. The side arm of the glass pipe (connected to a flask) is used to drain the excess liquid, obtained from the collision of the expanding aerosol flow with the walls. With this particular modification, the Mira nebulizer has shown to be a versatile and easily controllable device for aerosol generation.

3.3 Aerosol Conditioning

In this study, all aerosol experiments were carried out at ambient temperature and pressure. The key variables in the experiments were aerosol composition and relative humidity. As discussed in the previous section, aerosol composition was varied by atomizing or nebulizing solutions of different concentrations and their subsequent conditioning to a desired relative humidity, which was controlled by a system of driers and humidifiers. This section describes the drying and humidification methods employed in this work and the design of the units used for this purpose.

3.3.1 Aerosol Drying

In the course of this study we have used and tested two different methods for aerosol drying: a silica gel type of dryer and a semi-permeable membrane (Nafion) dryer. In this section we discuss these methods, their advantages and limitations, and the design of the custom-made drying units.

3.3.1.1 Silica gel Dryer

Silica gel diffusion dryer is commonly used in reducing the RH of the aerosol flow. The dryer is typically designed as a tube filled with a bed of highly hygroscopic silica gel beads. In our experiments, the dryer was made of a glass tube (10 cm i.d, 1 m long) filled with silica gel. As the aerosol passes through the silica gel filling, the water vapor from the carrier gas diffuses toward by the silica gel and is adsorbed by it. The decreased humidity of the carrier gas pushes the equilibrium by enhancing the water transfer from aerosol to the gas, resulting in the evaporation of water from the surface of the aerosol until a new equilibrium is reached. The reduction of RH is a diffusion limited process, thus it may be controlled by the length of the dryer or the residence time of the aerosol in the dryer.

Since silica gel is a very efficient drying agent it can remove a large amount of water from a sample, bringing it to a complete dry state in a single step. The downside of it, however, is that silica gel desiccant efficiency is substantially reduced after each experiment due to water saturation and aerosol buildup. Hence, cleaning and reactivating the drying material (which is a cumbersome and time consuming process) has to be done on a daily basis.

3.3.1.2 Nafion Dryer

The discussed drawbacks of using and regeneration of silica gel made us search for a different methods for drying aerosols. One promising alternative was a Nafion (Perma Pure LLC) based dryer.[40] Tubular Nafion dryers have been successively used in controlling the RH of hygroscopic aerosol particles.[41] The Nafion membrane, developed at DuPont, is an ionic polymer with a Teflon backbone and sulfonic acid groups added into the matrix (see Figure 3.3). Nafion is highly resistant to chemical attack, selective and permeable to water and impermeable to most of the gases.[40] The presence of a water vapor gradient across the membrane generates movement of the water molecules from one sulfonic group to the other, each sulfonic group being hydrated with up to 13 water molecules. The process is reversible, which makes it possible that Nafion be used as both a dryer and a humidifier, as demonstrated further in this chapter. A dry Nafion membrane can absorb up to 22% by weight of water[42] and it expands by about 10%. This fact should be taken into consideration when designing a dryer in order to preserve the shape of the Nafion tubing and consequently the aerosol flow and density in the flow tube.

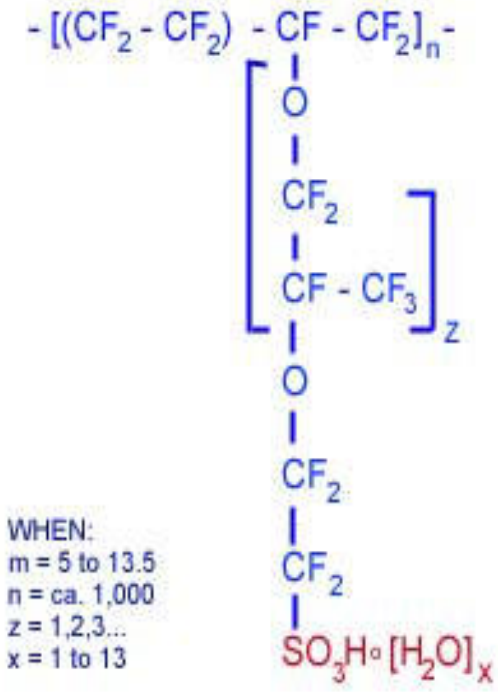

Figure 3.3: Chemical structure of Nafion. [40]

In most of our experiments dryers were made using Nafion tubing 90 cm long (ID 1.78 cm, wall thickness 0.01 cm) enclosed in a 3.81cm i.d. glass (Pyrex) jacket. On one end, the jacket is attached to a funnel-shaped glass piece (using plain drain pipe coupling), which reduces the jacket from 3.81cm i.d. to a 1.52 cm i.d. glass tube, the size that can loosely fit inside Nafion tubing. The 1.78 cm glass tube on the funnel-shaped piece extends coaxially further inside the expanding section of the piece, providing support to one end of the Nafion tube, to which is attached by a Teflon tape (Figure 3.4 a). The other end of the Nafion is attached to a 1.78 cm i.d. glass tube (18 cm long), again using a Teflon tape (Figure 3.4 b). This tube which holds Nafion is then coaxially attached to a glass jacket by a reducing, stainless steel quick fit connector that allows adjustments of the length of the Nafion at one end during experiments. This feature is essential for maintaining the aerosol flow constant during experiments, since Nafion is not self sustaining and in high humidity environment it expands and collapses inward. In addition, to secure the tubular shape of Nafion tube, three overhead transparency rings (2 cm wide) are placed inside the tube at equally spaced intervals. The glass jacket is designed with two side inlets, located one at the top and one at the bottom of the dryer.

Drying of aerosols is achieved by passing the aerosol flow inside the inner (Nafion) tube and a flow of dry nitrogen gas through the jacket. For the highest efficiency, the dryer works in the countercurrent mode, with the dry gas flowing in the opposite direction with respect to the aerosol flow. Apart from it, drying efficiency can be optimized by changing aerosol and sheath gas flow rates (i.e. residence times), the size (length and diameter) of the dryer, Nafion tube thickness, and Nafion temperature. To determine the optimal length of the Nafion tubing, two processes have to be considered: the diffusion of water vapor inside the Nafion dryer and the transport of water molecules across the membrane. (Diffusion rate of water molecules from the surface of the aerosol particles to the carrier gas in this case is not taken into account.) Since it was reported that the rate of mass transfer of water through the Nafion membrane is high compared with the rate of its diffusion,[43] drying can be considered diffusion limited. The minimal length of the dryer can be determined by assuming that the residence time of the aerosols in the dryer should be at least equal or longer than the diffusion time of water molecules.[42]

Figure 3.4:
Nafion Dryer/Humidifier:
a) Upper part and connection to the U shape Glass tube
b) Lower part

$$t_{diff} \leq t_{res} \tag{3-1}$$

where diffusion time, t_{diff}, and residence time, t_{res}, are defined as

$$t_{diff} = \frac{r^2}{D_g} \tag{3-2}$$

and

$$t_{res} = \frac{L}{u} = \frac{L}{F_c / r^2 \pi} \tag{3-3}$$

In the equations (3-1), (3-2) and (3-3), r and L are the radius and the length of the Nafion tube in m, D_g the diffusion coefficient of water vapor in nitrogen gas or air (cm^2/s) its length, u the velocity (cm/s) and F_c the flow rate of the nitrogen gas (cm^3/s) through the Nafion tube. From the given equations, the expression for the minimal length of the dryer can be derived to be

$$L \geq \frac{F_c t_{diff}}{\pi r^2} \tag{3-4}$$

For the 1.78 cm i.d. Nafion tubing used in this work and the t_{diff} of water vapor from the center to the inner wall of the membrane of around 1.8s (obtained assuming that D = 0.22 cm^2/s), and the high limit flow rate used in our experiments of around 50 cm^3/s, the minimal length of the dryer was determined to be around 36 cm. In most of the experiments in this study we used the Nafion drier length of around 90 cm, as described above. In general, its efficiency (given varied aerosol and dry N_2 flow rates) was such that liquid ammonium sulfate aerosols (RH > 80%) could be dried to solid particles (20%<RH <35%) in a single step. It should be noted that the efficiency of the dryer does decrease gradually in time due to aerosol buildup on the Nafion membrane. However, the regeneration of Nafion is simple and quick, merely by rinsing the membrane with de-ionized water and drying it with nitrogen gas.

3.4 Deliquescence reactor

As already mentioned, a simple Nafion humidifier described in the previous section can be used to deliquesce aerosols. In this case the deliquescence process, in particular the deliquescence time of aerosols, can be controlled only by varying the aerosol flow rate. This, in return, affects the overall conditions in the reactor by changing the aerosol flow pattern and its residence time in other parts of the flow system. For the purpose of the deliquescence kinetics experiments, in which deliquescence time and deliquescence process in general should be closely controlled, we designed a deliquescence rector.

The reactor, shown in Figure 3.5, is a Nafion-based humidifier which allows for the deliquescence time to be gradually changed without changing other aspects of the aerosol flow. The reactor consists of a stainless steel tube (110 cm long, 3.5 cm i.d.) perforated throughout the middle section (96 cm long with 60% of the area opened), enclosed in a glass jacket (110 cm long pipe with a 10 cm i.d) as seen in Figure 3.6 b. The perforated tube supports the Nafion membrane through which water vapor transfer takes place. The Nafion membrane (103 cm long, 14.5 cm wide and 50.8 microns thick, from Ion Power Inc.) is wrapped around the perforated tube and sealed at both ends with Teflon tape. A rubber band (SBR Rubber-Red, Allstate Gasket, 0.15 cm thick) and a stainless steel strip (100 cm long, 0.25 cm thick and 1.3 cm wide) are placed on top of the overlapped edges of the membrane and fixed to the perforated tube by gear clamps (1 cm wide) with rubber strips underneath. Five gear clamps at equal distances are used to secure the Nafion. The rubber strips are necessary to provide a better seal to the perforated tube and to protect the membrane from tear. The solid ends of the perforated tube are attached to the glass jacket by PVC fittings as it can be seen in Figure 3.6 a and c.

Another essential part of the deliquescence reactor is a movable inlet, which is used to vary the surface area available for transfer, that is, the contact time between aerosols and the water vapor. Essentially, the inlet is a stainless tube (145 cm long and 3.25 cm i.d) which can slide in and out of the perforating tube, to which is attached by a quick fit connector.

In deliquescence experiments, humidified nitrogen gas is introduced concurrently into the reactor jacket and water vapor transferred to aerosol flow inside the perforated tube. When the deliquescence reactor is closed, i.e. the inlet completely inside the perforated tube, there is no contact between water vapor and aerosols. The reactor is completely open when the inlet is outside the perforated tube, allowing maximum water vapor transfer. The diffusion time of water vapor in the reactor can be calculated applying eq.3.2. In a nitrogen atmosphere and in the absence of any flow, the diffusion time is about 12.65 s.

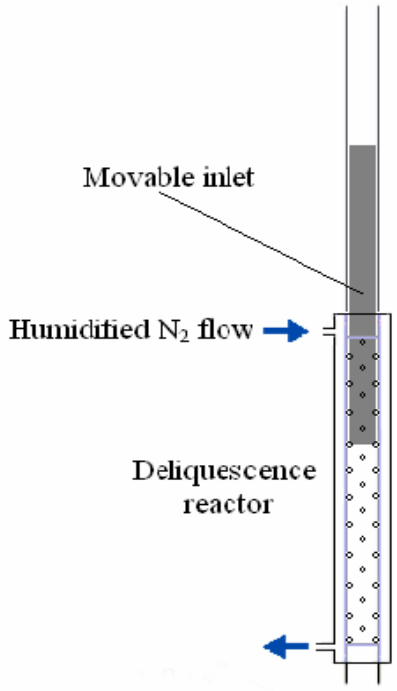

Figure 3.5: Schematic drawing of the Nafion based Deliquescence Reactor

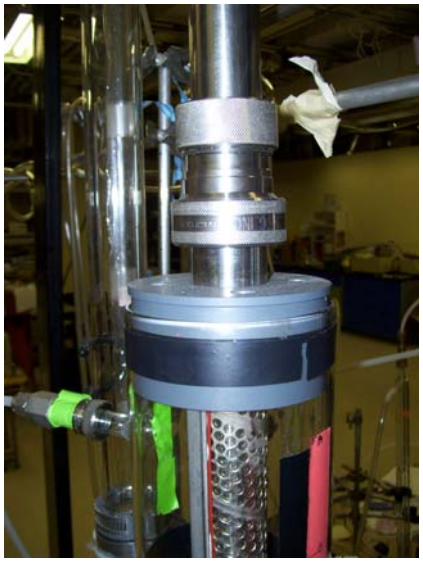

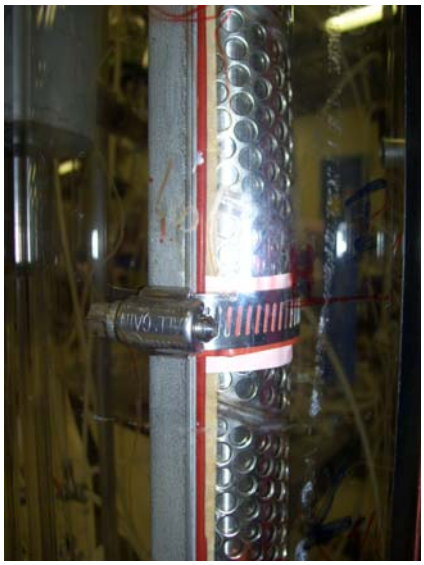

Figure 3.6: Deliquescence reactor:

a) **Upper part and connection to the movable inlet**
b) **Middle part**
c) **Lower part and connection to the observation cell**

3.5 Aerosol detection

As discussed in Chapter 2, in this work we used an inversion method coupled with infra red spectroscopy to monitor and characterize aerosols *in situ* from their infra red spectra. While the numerical aspect of the procedure is explained in Section 2.2.1, the experimental part including the description of the optical set up and the FTIR measurement procedure is described in the following section.

3.5.1 FTIR Measurements

In our setup the infrared beam from the Fourier Transform Infrared Spectrometer (IFS 55) passes though an observation cell and is collimated by a parabolic mirror into the MCT transducer. Before each experiment the photoconductive MCT detector is cooled by liquid nitrogen to reduce thermal noise, providing a 7-8 hours working window after every cooling. An observation cell, which is essentially a stainless steel cross with perpendicular side arms (3.5 cm i.d., and arms 2 cm i.d., MDC company), is placed in between the FTIR and the detector. The side arms of the cell are equipped with KRS-5 (Thallium Bromo-Iodide) windows (0.4cm thick and 3.75cm diameter, International Crystal Labs) and aligned with the infra red beam. KRS-5 material was chosen due to its wide transmission range (20000-250 cm^{-1}) and low solubility in water. For this particular study the latter feature is very important, because many experiments were carried in high humidity environment. The acceptance angle of a Michelson interferometer and hence of the detector is very small, (approximately 10^{-3}sr in our apparatus), justifying the assumption that only forward scattering reaches the detector in calculating the extinction spectra.

The infra red spectra are recorded by IFS 55 (by Bruker Optics) utilizing OPUS software (again provided by Bruker Optics). Spectroscopically, the aerosols are monitored over the range 500 to 6000 cm^{-1}. The extinction spectra are recorded with a resolution of 4 cm^{-1} and each spectrum is the result of 100 scans. The number of scans was chosen after a few experimental trials and represents a compromise between a good signal-to-noise ratio and the recording time. Before each experiment the system is flushed with dry N_2 until the traces of ambient gases such as water vapor and CO_2 are completely removed, and a background spectrum is then recorded.

To minimize moisture adsorption and accumulation on the sensitive (optical) elements of the spectrometer and detector, the FTIR spectrometer and the MCT detector box were continuously purged with 8 and 6 SLPM of dry nitrogen, respectively. One of the regulators is used to purge the metal box (26cm x 29 cm x 32cm) that houses the detector.

3.6 Nitrogen humidification system

The humidified nitrogen flow, used in the humidifiers described above, was produced in two ways. For the pre-humidifying (conditioning) stage in which the aerosols should be brought to around 75% RH, we used a humidified nitrogen flow of around 93% produced using water bubblers. A bubbler is basically a glass flasks (500 cm^3) equipped with a glass tube (0.8 cm i.d.) in the center, which ends with a cylindrical piece of sintering glass (2 cm long). A flow of dry nitrogen is passed through a bubbler filled with deionized water. To remove any water droplets carried by the flow, the bubbler output was passed through a separatory funnel (1 l volume) with a side inlet at the top, through which only a gas phase is further transferred to the pre-humidifier. The efficiency of the bubbler at room temperature was tested with respect to the nitrogen gas flow rate and the produced relative humidity. For the given bubbler design, it was found that the optimal nitrogen flow rate is around 2 l/min, resulting in the humidified flow of around 93% RH. In the case of experiments where higher input of humid nitrogen was needed, two or four bubblers were used in parallel, providing up to around 10 l/min of humid nitrogen at 91-93% RH.

To obtain a humidified gas with higher humidity than 93%, as needed for deliquescence experiments, a different humidification method was used. For this purpose a TSI atomizer was used to generate water aerosols (at 3 l/min). The atomizer output is diluted with a variable dry nitrogen flow and passed through a 3m long, 3.81cm i.d. glass pipe to equilibrate. The system was calibrated with respect to the dry nitrogen flow and it was found that around 1.5 l/min is needed to produce 99% humidified nitrogen flow at total rate of 4.5 l/mim. The humidified nitrogen flow was again passed thought a separatory funnel prior to entering the deliquescence reactor jacket.

3.7 General experimental set up

As mentioned previously, in the course of this work we performed several different kinds of experiments on aerosols using different experimental set ups. So far we talked about the major components of the experimental assembly. In this section we describe the experimental set up itself and how these units are incorporated into an aerosol flow reactor. We will also present the most universal version of the set up, the design of which can be easily modified (according to specific experimental requirements.) due to the fact that most of the units are interchangeable with standard connections.

The aerosol flow reactor set up, shown in Fig 3.7 , was used for the deliquescence kinetics experiments described in more detail in Chapter 8. The purpose of this particular experiment was to produce dry $(NH_4)_2SO_4$ particles, pre-condition them to a near-deliquescence RH and, in the final step, deliquesce them partially or fully. The set up therefore consists of an aerosol generator (atomizer or Burgener nebulizer), a Nafion dryer in which $(NH_4)_2SO_4$ solution droplets are dried to solid that is RH < 35%, a Nafion pre-humidifier in which the dry aerosol is conditioned to around 75 % RH, a U-shape glass tube leading the aerosol to the reactor, in which they are deliquesced to RH > 80% and the observation cell in which they are monitored. The monitoring system also includes the FTIR and MCT detector. To maintain the residence time and flow characteristics of aerosols constant, a glass tube (1.5 m long) is placed at the top of the deliquescence reactor to accommodate the full length of the movable inlet, to which is connected by a stainless steel quick fit connector. A 15 cm bare inlet section is left between the two quick fits connecting the inlet to the glass and the perforated tube, in order to be able to move it manually up and down. A good alignment of the perforated tube with the top glass pipe is essential for the inlet to slide smoothly. Otherwise, moving of a not properly aligned inlet along the deliquescence reactor may affect the observation cell position and subsequently the amplitude of the IR signal.

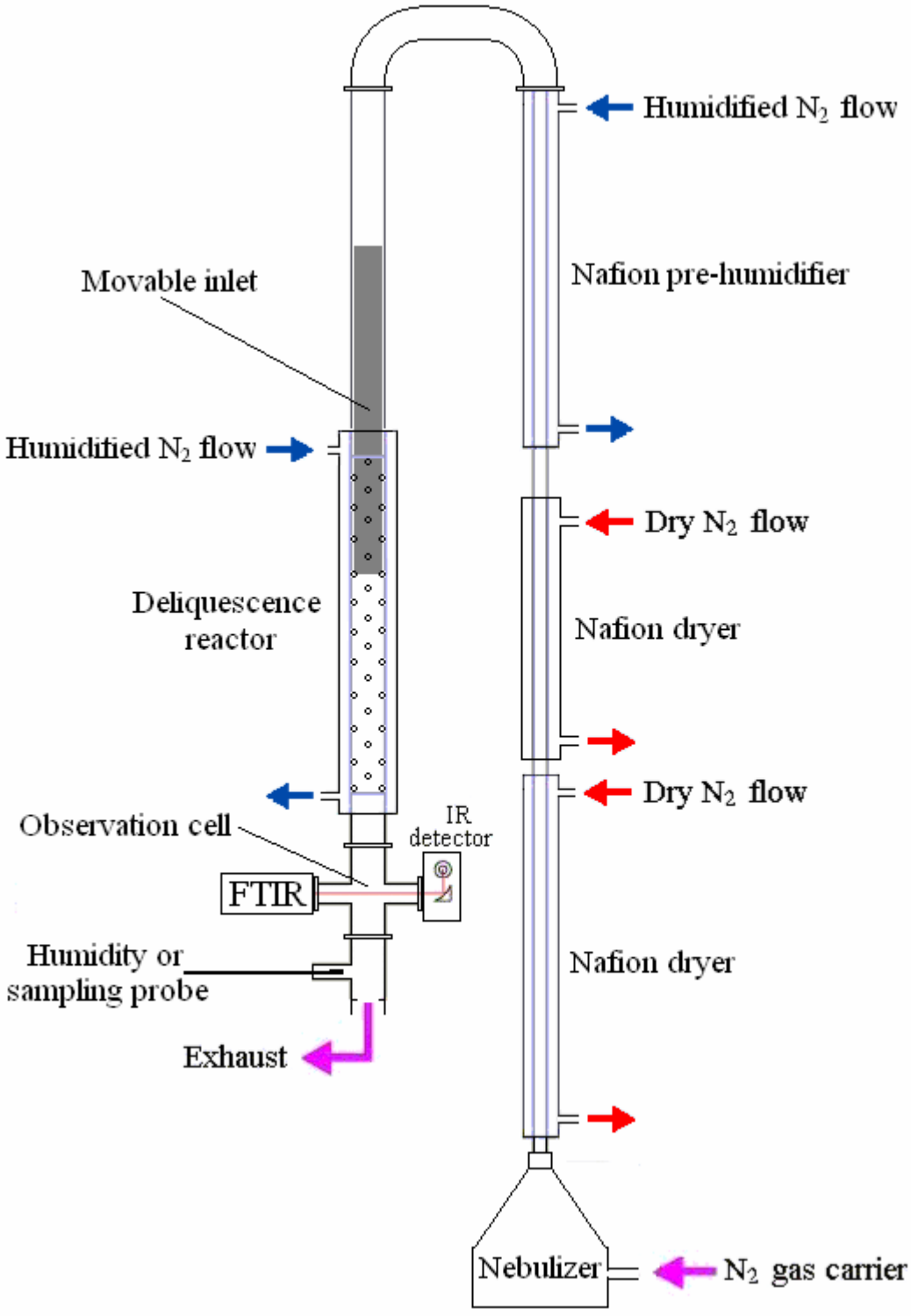

Figure 3.7: **Schematic diagram of the room temperature glass flow tube used in the kinetics of deliquescence of AMS experiments.**

The stainless steel observation cell is located downstream from the deliquescence reactor and is attached to the perforated tube by a two-sided stainless steel quick fit. Although the fit itself can hold the cell, an additional stand was used to provide better physical support to the cell, since the slightest changes in the cell position during experiment may lead to significant changes in the amplitude of the IR signal. For that purpose a metal holder which bolts into the floor was designed. The holder is equipped with a metal ring in which the bottom part of the cell can be fitted and secured against rotation and movement in either direction. Downstream from the cell, a cylindrical (3.5 cm i.d., 15 cm long) stainless steel piece was placed to accommodate the probe for temperature and humidity measurements. The piece has a 1.25 cm i.d. side arm with a quick fit in the end, which holds the probe firmly and provides air-tight connection. The cylindrical probe holder is attached at the top to the cell and at the bottom to the exhaust system by a Teflon drain pipe connector.

The remaining units of the aerosol flow reactor are joined using different types of connectors. The 3.8 cm i.d. glass pieces (the long glass and the U-tube) are connected with stainless steel drain pipe couplings. The 1.27 cm movable glass ends of the Nafion dryer and the pre-humidifier are connected with a stainless steel two-sided quick fit with a 15 cm long body that provides extra space for the extension of the Nafion under high RH conditions. The 1.27 cm stainless steel outlet of the atomizer and 1.27 cm glass inlet of the dryer are attached with a standard stainless steel two-sided quick fit connector. The 1.27 cm i.d. glass outlet of the pre-humidifier and the 3.8 cm i.d. glass U-tube are connected with a custom-made cylindrical Teflon fitting (3.8 cm. o.d. and 1.27 cm i.d. inner opening). The same type of fitting is used to reduce the outlet of the horizontal (3.8 cm i.d.) glass tube holding the nebulizer to a 1.27cm i.d. plastic tube (5 cm long), which is then connected to the dryer 1.27cm inlet with a flexible, 90°-bent silicone tubing (1.27cm i.d., 20 cm long) which can snugly fits onto the 1.27cm solid tubing (and is further secured by gear clamps.).

The entire flow apparatus, including the optical system, were supplied by a high pressure nitrogen gas, which was previously purified for (possible) particles and organics by passing it through a Whatman Carbon Cap (activated carbon filter device, Arbor Technologies Inc.).

To regulate the flow rates and provide stable flow conditions, the purified high pressure nitrogen is divided through a system of 6 regulators and 10 flow meters (Omega Engineering Inc.).

All stainless steel parts used in our experimental setup are pretreated with a hydrophobic fluoropolymer (FluoroPel PFC 802A-FS, Cytonix Corp.)[44] to reduce particle deposition and water droplet accumulation on the walls. As mentioned previously, the observation cell windows are continuously purged (during and off experiments) with dry nitrogen gas (typically at around 10 cm^3/min (standard)) to prevent aerosol deposition and moisture absorption.

Figure 3.7 shows a generic version of the experimental set up that can be used in most of the experiments done in this study. Depending on the particular experimental requirements, this could have been done by simply reversing the roles of the drier and pre-humidifier or by closing them off if no exchange was needed. However, as it will be shown in the following chapters, in such cases – when no water vapor exchange was required, the dryer, the humidifier, or the deliquescence reactor were rather replaced by simple glass tubing (3.8 cm i.d.). This was done for several different reasons. First, using FluoroPel coated glass tube instead of a closed off Nafion exchanger speeds up simple aerosol conditioning process. Second, it minimizes aerosol deposition on the walls relative to the case when Nafion membrane is used. All these variations in the experimental set up and operating conditions used in different experiments will be discussed in the beginning of the chapter dealing with that particular study.

3.8 Relative humidity measurements

As discussed, relative humidity is one of the most important variables in the aerosol experiments done in this study. The quality and interpretation of the results therefore strongly depends on the accuracy of relative humidity measurements. In our experiments, depending on reaction conditions, humidity was determined in two different ways. By direct measurements, using a Vaisala humidity probe or indirectly, using humidity calibration curve. In direct measurements, Vaisala humidity probe (HM70)[45] was used to measure the RH and temperature of the carrier gas in the flow tube.

The probe is a 33 cm long, 1.25 cm diameter stainless steel tube equipped with a HUMICAP^{R} 180 sensor, enclosed at the tip in a protective, stainless steel filter cap. Water vapor diffuses from the carrier gas through the filter and to the humidity sensor, resulting in a 20 to 40 s response time of the probe to changes in RH. The humidity probe is supplied with a MI70 hand held indicator and a PC software for direct data monitoring and storage. The accuracy of the instrument in measuring the RH, as reported by the manufacturer, is ±1% for RH from 0 to 90% and ±2% for RH from 90-100%. The accuracy of the temperature measurements is specified to be $\pm 0.2^{0}$C at $+20^{0}$C.[45]

The presence of contaminants (species other than water) in the system may result in their deposition on the filter cap or diffusion to the sensor, leading to a decrease in the sensitivity of the humidity probe, a shorter lifespan and a change in calibration. Similarly, the presence of condensed water on the sensor is another source of inaccuracy. Two functions in the instrument settings can be used to solve these problems. Absorbed chemicals can be evaporated by performing a chemical purge (during which the sensor is heated at 160^{0}C for 2 minutes) and condensed water can be removed by a sensor preheat (in which the sensor is heated to 100^{0}C for 4 minutes). It is recommended that a chemical purge and a sensor preheat be performed before each experiment, especially when the probe has been exposed to a high concentration of contaminants.

Since the effect of ammonium sulfate aerosols on the humidity sensor is not known, in addition to direct measurements (where the probe is placed in the aerosol flow), the RH was determined by means of a RH calibration curve and the two methods were compared.

The calibration curve is obtained in an experiment, in which the area of the 1887-1891 cm^{-1} water vapor band is correlated to the relative humidity measured by a humidity probe. In the calibration experiment, a saturated flow of nitrogen (2.3 l/min) is generated by atomizing deionized water with a TSI atomizer (at 25 PSI) and passing it through a Nafion dryer to remove extra liquid water. The humidity of the flow is then randomly varied in the 15-100% RH range, by changing the drying rate (26 to 0 SLPM, dry nitrogen sheath flow rate) in the Nafion dryer.

Using a somewhat modified experimental set up than the one shown in Figure 3.7, where the pre-humidifier and the deliquescence reactor are replaced by a simple glass tubing (3.8 cm i.d.) infrared water vapor absorption spectra are recorded simultaneously with the direct RH measurements using the Vaisala probe. An example of one such calibration curve, obtained by correlating the integrated area of the water vapor band with the measured RH is shown in Fig. 3.6 by red markers. Since in separate experiments we deal with different aerosol flow rates, it was appropriate to test the calibration curve for the dependence on this variable. For that purpose, the humid nitrogen flow rate was increased to 3.3 l/min (by operating the atomizer at 35 PSI) and a separate calibration curve was generated, represented in Fig 3.6 by blue markers. As it can be seen, there is a very good agreement between the two calibration curves, indicating that the relative humidity measurements are not sensitive to the absolute water vapor concentration, as it should be the case. Taking into account the uncertainties of the humidity probe readings and calibration fits, the precision of the humidity measurements obtained using the calibration curve is estimated to be ± 2% for RH from 0 to 90% and ±3% for RH from 90-100%.

By comparing the measurements obtained using both methods and based on our own experience, we came to the conclusion that we can rely on direct RH measurements when dealing with diluted salt solution, in which case the difference between the direct and indirect method is less than 0.5%. Otherwise, in the case of concentrated ammonium sulfate solutions, the difference between the RH values obtained from the direct measurement and calibration curve may amount to about 3% (at RH>75%).

Due to the corrosive nature of ammonium sulfate and its possible deposition on the probe's sensor, which may have affected the manufacturer's calibration and the accuracy of the probe, the probe itself had to be re-calibrated after every few experiments. A two point calibration is done using standard, saturated salt solutions with well known relative humidity at room temperature, such as LiCl-11.3%, NaCl-75%, and K_2SO_4-97%.[46] Since the RH measurements and the calibration itself are very sensitive to changes in temperature, the probe calibration was preformed in a well insulated volumetric flask containing standard salt solution.

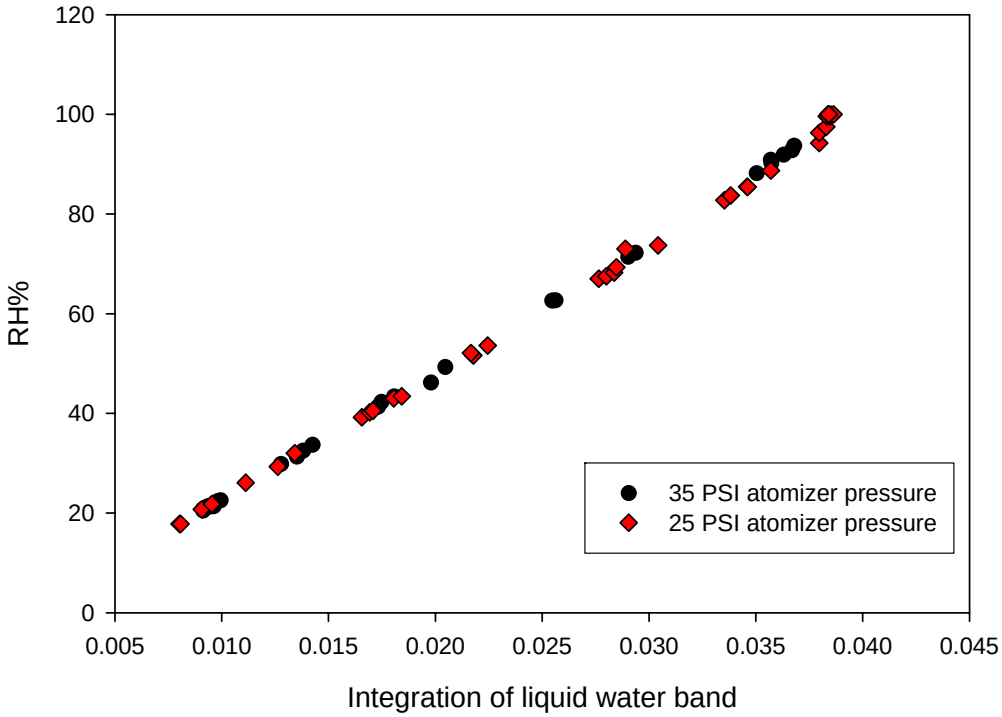

Figure 3.8: Calibration of the IR signal as a function of the RH for two different operating conditions of the atomizer.

Chapter four: Determination of complex indices of refraction for crystalline ammonium sulfate

4.1 Introduction

The complex refractive indices (optical constants) for crystalline $(NH_4)_2SO_4$ at 298 K have been reported previously by Toon et al..[47] These values are widely used in remote sensing and laboratory studies of aerosols.[e.g. 48-51] Discrepancies observed when these optical constants are used in Mie fits to experimental extinction spectra[49] suggest that the values are not fully accurate, or are too coarsely resolved. The goal of this study was to improve the frequency dependent refractive indices for crystalline $(NH_4)_2SO_4$ at ambient pressure (1 bar) and 298 K. The new values obtained in this study cover the spectral range from 590 to 5990 cm^{-1} with 2 cm^{-1} resolution. The new indices of refraction are based on infrared (IR) extinction measurements of aerosol obtained in a glass aerosol flow tubes (AFT). The indices of refraction were extracted from the measurements using the inversion procedure described in Section 2.3 .[52]

4.2 Experimental

The room temperature experiments were carried out in the glass AFT, shown in Figure 4.1. The main modification relative to the generic experimental set up shown in Fig. 3.7 is that the Nafion pre-humidifier and the deliquescence reactor are replaced by 3.8 cm i.d. glass tubing. In these experiments, crystalline $(NH_4)_2SO_4$ aerosols were produced from a solution using the constant output atomizer driven by a flow of dry N_2 (35 psi, 3 SLPM). In order to generate different dry aerosol sizes, five different concentrations of $(NH_4)_2SO_4$ solution were used: 0.1, 0.2, 0.5, 1, and 2 M. Thus, for example, a 1μm droplet generated by the atomizer from a 0.1M solution contains a smaller amount of AMS than the same size droplet generated from a 2M solution. Hence, removal of water from the aerosol droplets during the drying process leads to the formation of crystalline particles of different sizes. The solutions were prepared from reagent-grade $(NH_4)_2SO_4$ (Sigma-Aldrich Co.) and Millipore®-filtered de-ionized distilled water.

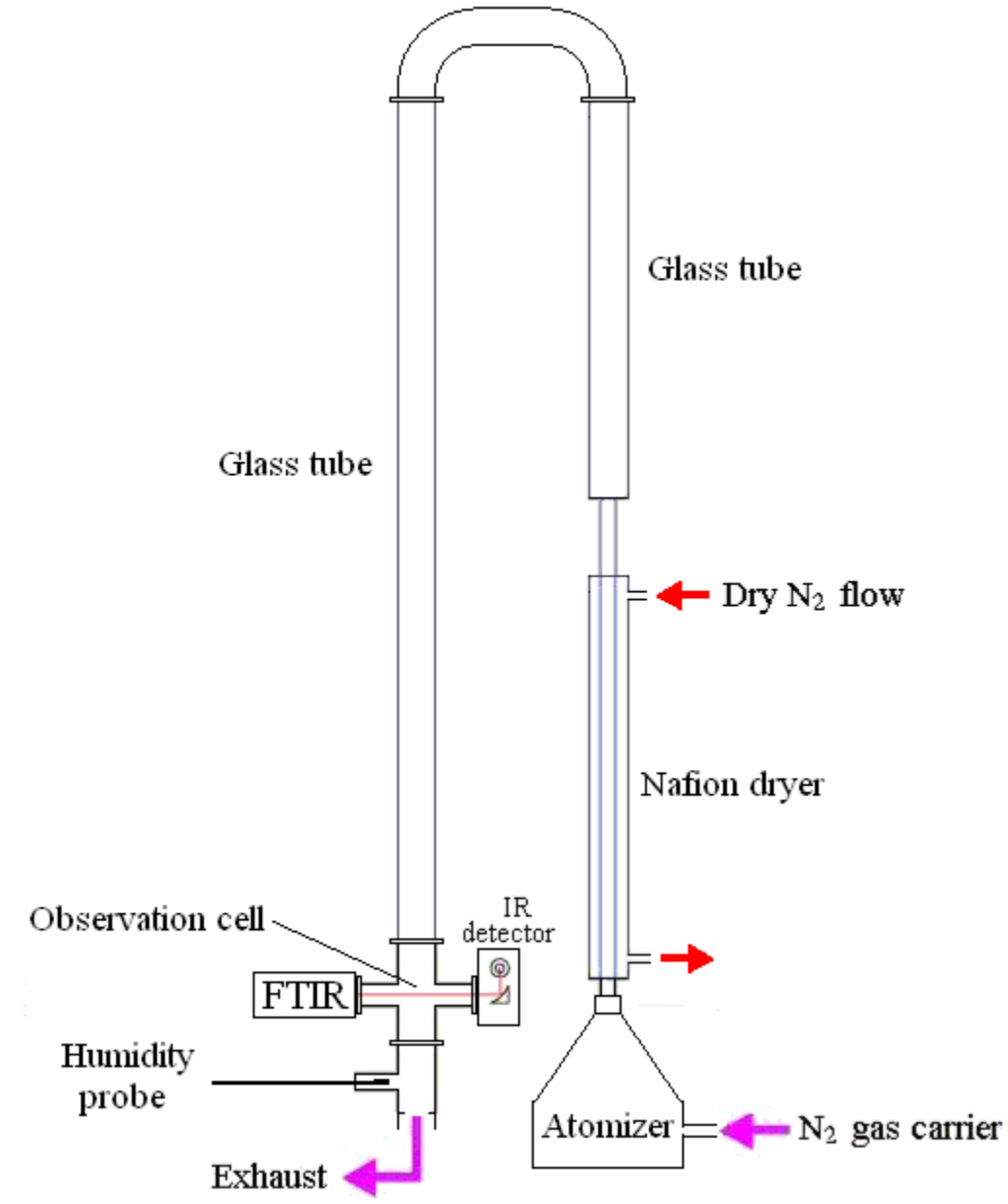

Figure 4.1: Schematic diagram of the room temperature glass flow tube used in the determination of complex indices of refraction for crystalline AMS.

The solution aerosols were evaporated in a Nafion dryer. A counter-flow of dry N_2 was passed through the jacket at flow rates between 25 and 30 SLPM, producing a high relative humidity (RH) gradient that drives the rapid diffusion of gas-phase water through the Nafion® membrane. Under these conditions, the RH in the aerosol stream was reduced to between 10% and 12%, drying the aerosols. The dry aerosols were then passed through a U-shaped glass tube.

The total reaction tube length, including the dryer, was approximately 3 m, resulting in residence times of approximately 1 minute. This time was sufficient for equilibration of water between the aerosol and vapour phases, as verified by a number of experiments carried out using longer residence times. The equilibrated aerosols were introduced into the observation cell where the windows were purged with a small flow of N_2 (less than 1% of the total flow rate) to minimize aerosol deposition. At this point extinction spectra were acquired at a resolution of 4 cm^{-1} with each spectrum being an average of 100 scans. All spectra were taken under steady-state conditions; that is, after the relative humidity reached a constant value in time. In this particular experiment, the relative humidity in the observation cell was determined using the calibration curve method.

4.3 Results and Discussion

The infrared spectra shown in Figure 4.2 were obtained at 298 K using different initial concentrations of $(NH_4)_2SO_4$ solution as described in Section 4.1, resulting in different dry aerosol size distributions. (The shown spectra are those obtained after CO_2 and water vapour subtraction). The strong absorption features at 2800-3300 cm^{-1}, 1420-1450 cm^{-1}, 1115 cm^{-1}, and 620 cm^{-1}, corresponding to the ν_3 (NH_4^+), ν_4 (NH_4^+), ν_3(SO_4^{2-}), and ν_4(SO_4^{2-}) modes, respectively,[53] are clearly visible under all conditions. As would be expected, there is an increase in the aerosol extinction with the concentration of $(NH_4)_2SO_4$ solution. The increase in extinction above 3500 cm^{-1} is due to particle scattering, which increases for larger sizes.[54]

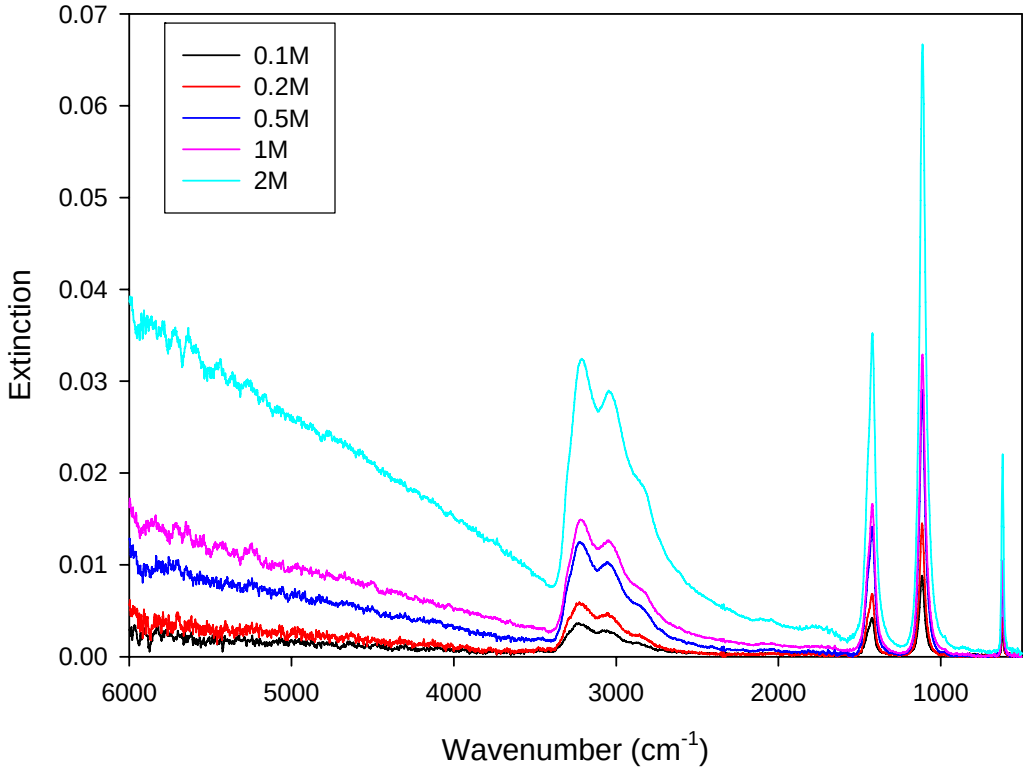

Figure 4.2: Examples of typical IR spectra recorded for different sizes aerosols.

Each extinction spectrum shown in Figure 4.2 was used to compute a new set of optical constants using the procedure described in Section 2.3. Initially, we chose the smallest AMS particles spectrum obtained in our laboratory earlier in a separate experiment, as an initial guess for $k(\nu)$, the imaginary part of the refractive index. In that particular experiment, ammonium sulphate aerosols were generated by the TSI atomizer from a 0.1mol/L ammonium sulphate solution and dried by passing through the silica gel diffusion dryer. Before using the spectra, in general, CO_2 and water vapour spectra should be subtracted from the original recorded (AMS) (extinction spectra). The "small particle spectrum" proposed as a first guess is presented in Fig. 4.3, before and after the subtraction of gas phase water and CO_2 absorption features.

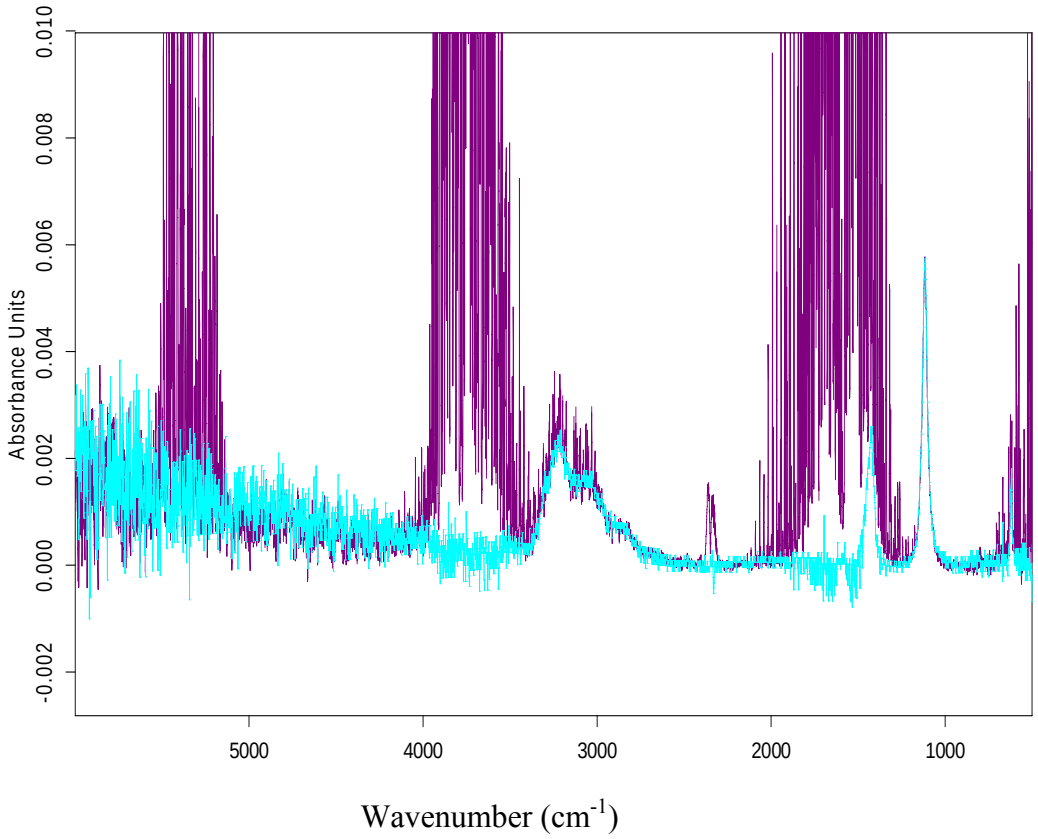

Figure 4.3: A "small particle spectrum" original (magenta) and after subtraction of CO_2 and water vapor (light blue).

Figure 4.4 shows a fit to the ammonium sulphate (2 M) spectrum obtained employing the optical constants generated from the experimental spectrum and the "small particle spectrum" from the Figure 4.3 as the initial guess. As demonstrated in Figure 4.4, there is a good overall agreement between the experimental spectrum (2 M) and the fit, with the exception of the 25% difference in the intensity of the $\nu_3(SO_4^{2-})$ peak at 1115 cm^{-1}.

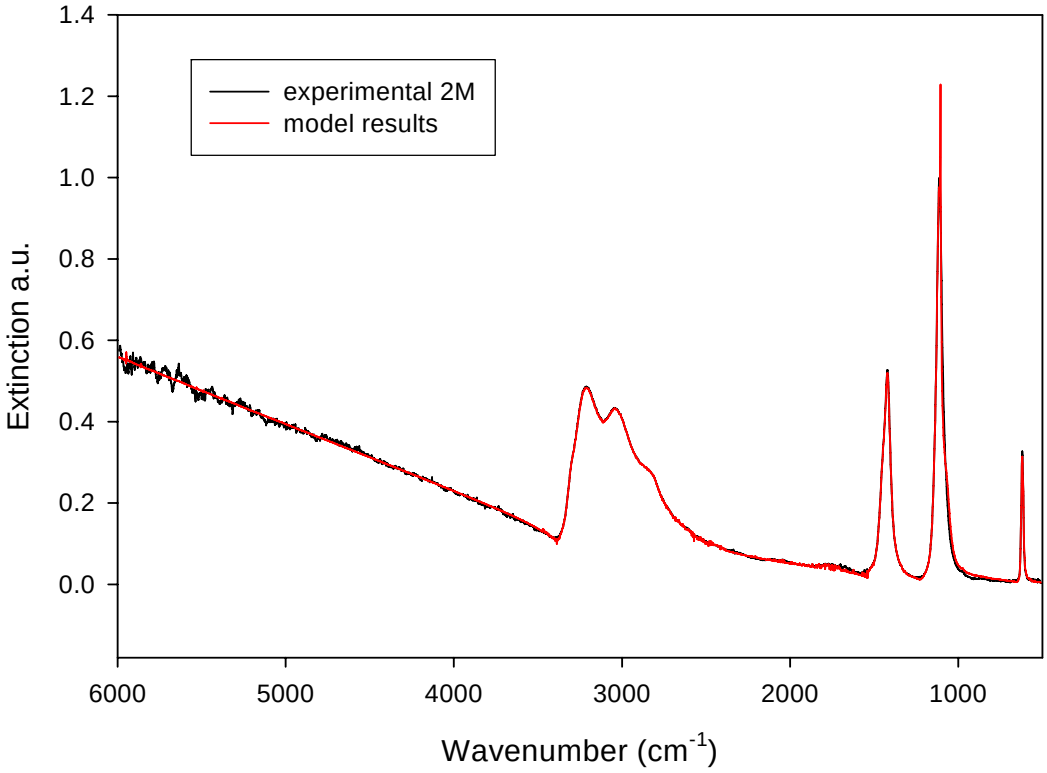

Figure 4.4: $(NH_4)_2SO_4$ experimental (black) and the calculated spectrum (red) for 2M generated using a small particles spectrum as a first guess.

Figure 4.5 shows the optical constants derived from all five experimental spectra (from Fig. 4.2), using the "small particle spectrum" shown in Figure 4.3 as the initial guess.

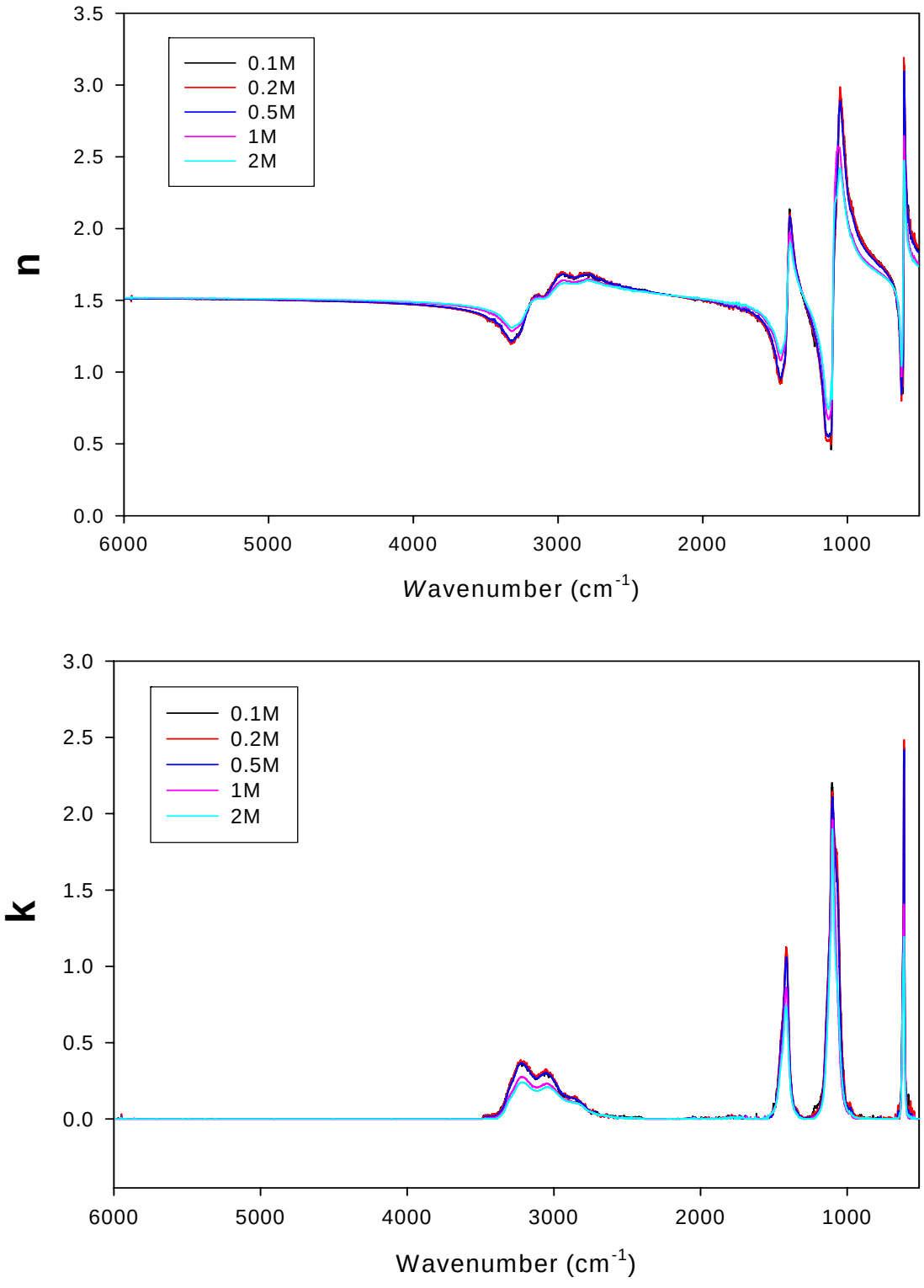

Figure 4.5: The imaginary and the real part of the refractive index (for all experimental spectra) determined in the first step.

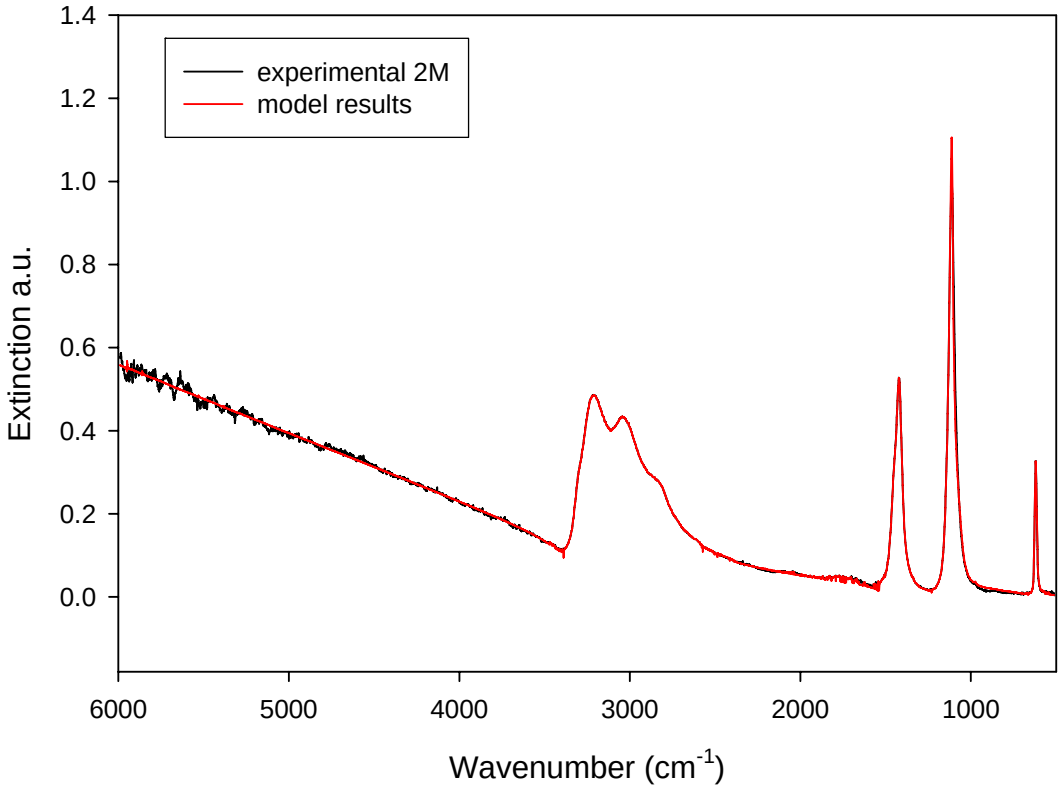

Figure 4.6: $(NH_4)_2SO_4$ experimental spectrum (black) and calculated extinction spectrum (red) obtained using the new set of optical constants as a first guess $\Delta\chi$= 0.005.

As can be seen from Fig. 4.5, there are obvious discrepancies between the retrieved imaginary part, *k*, and real part, *n*, values for aerosols with different size distributions, especially in the regions corresponding to the ν_3 (NH_4^+) and ν_4(SO_4^{2-}) absorption peaks. To determine if these significant deviations are due to the choice of the initial guess or inherent to (the) experimental spectra due to their different aerosols sizes, a new initial guess for k0(v) was chosen. In this case the smallest particle spectrum from the set, the 0.1 M AMS spectrum, was chosen as an initial guess (for the calculation of optical constants from all experimental spectra). Figure 4.6 shows the experimental and the newly computed spectrum for 2 M AMS, using the new initial guess for $k_0(\nu)$. In this case, the difference in the intensity of the ν_3(SO_4^{2-}) peak between the computed and recorded spectrum is reduced down to 11%, as seen in the figure.

The optical constants derived in this second trial are shown in figure 4.7. A very good agreement, much better than in the previous case, is evident for all aerosol sizes.

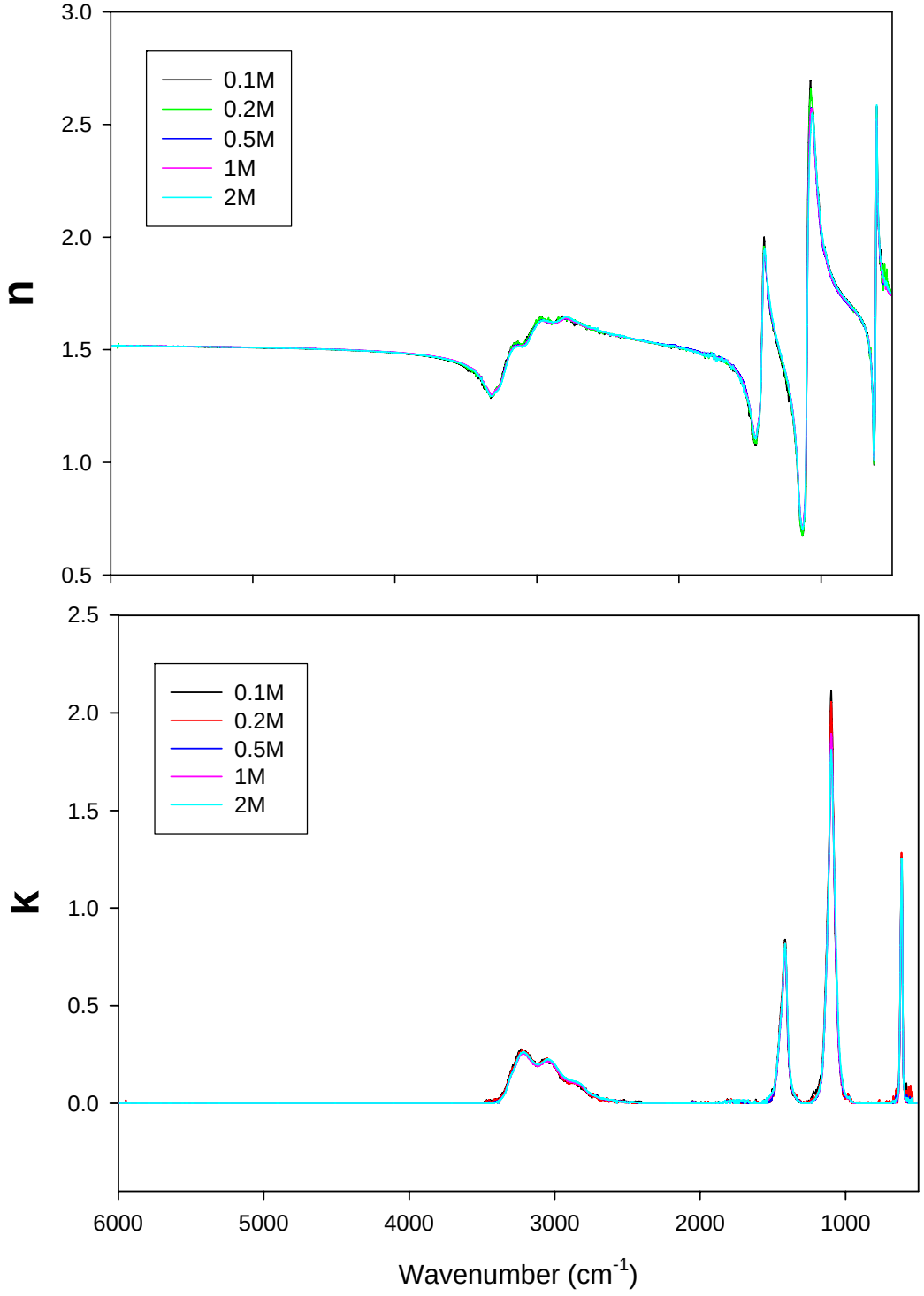

Figure 4.7: A comparison between the optical constants retrieved in the second step, for all experimental spectra.

The averaged values of *n* and *k* are shown in Fig 4.8 against the values by Toon *et. al*.[2,47], which were the only other available data before this study.

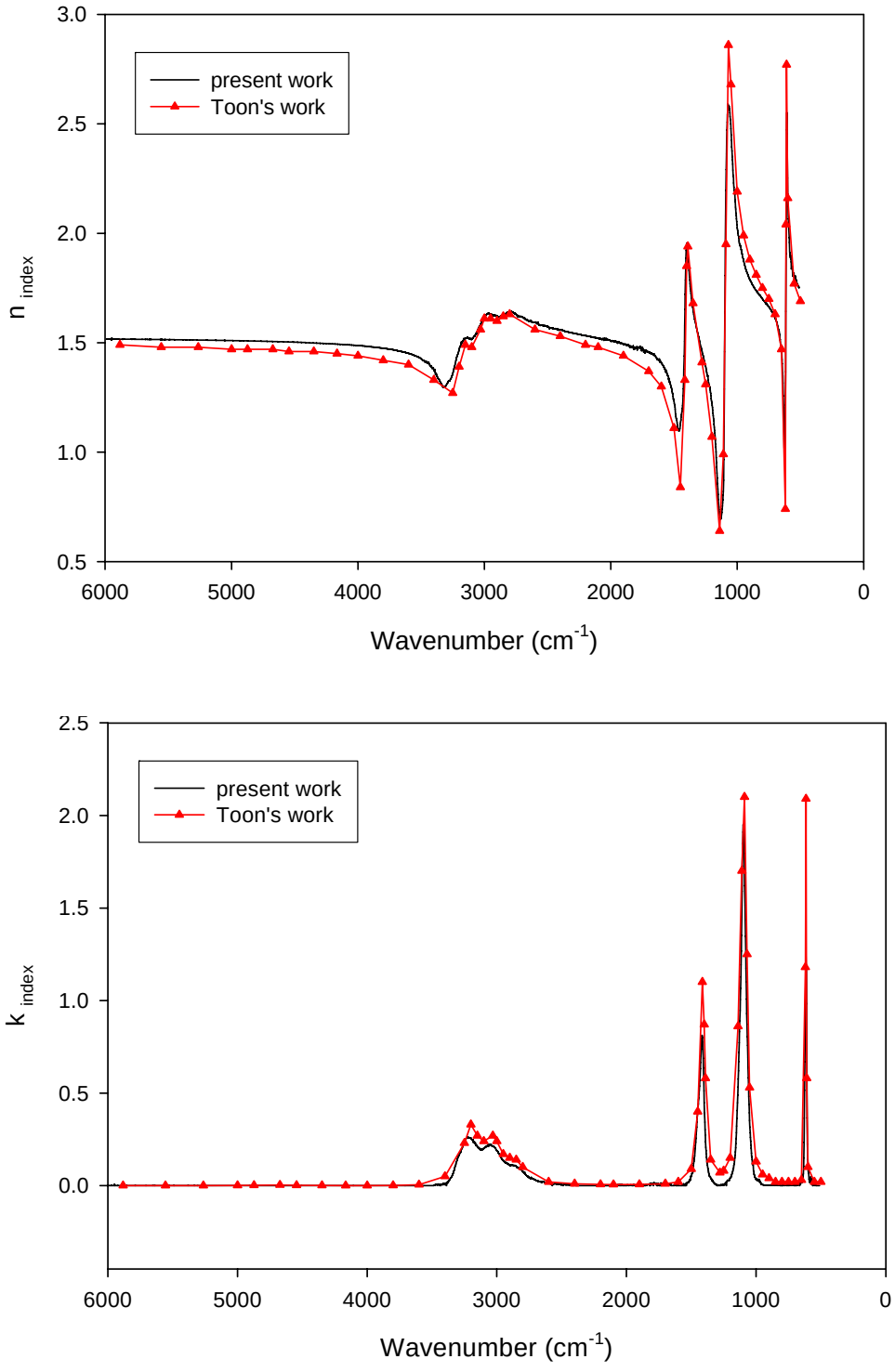

Figure 4.8: A comparison of the newly derived optical constants and Toon's data.

Compared to our averaged values, which cover the range 590 to 5990 cm^{-1} with 2 cm^{-1} resolution, the values of Toon *et al*. are poorly resolved, with only 58 values between 500 and 6000 cm^{-1}. In addition, there are significant differences in *n* and *k* values between the two data sets. Differences in *k* are limited to the absorption band regions, while the differences in *n* cover most of the spectral range. As a result, the values of Toon *et al.* are insufficient to accurately reproduce $(NH_4)_2SO_4$ extinction spectra, explaining the fitting errors observed previously.[49] This is demonstrated in Figure 4.9, which shows that a measured $(NH_4)_2SO_4$ spectrum (black curve) is reproduced exactly using our averaged optical constants (red curve), whereas the optical constants of Toon *et al.* do not give as good a fit to the measured spectrum (green curve).

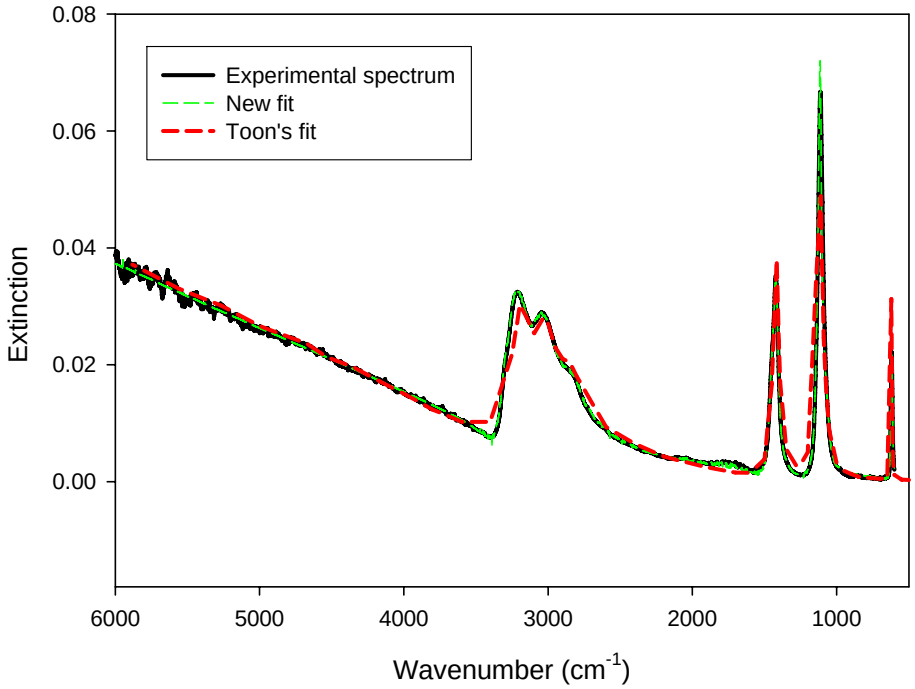

Figure 4.9: Calculated fits to a measured extinction spectrum of 2M $(NH_4)_2SO_4$ at 298K using our averaged optical constants and the values of Toon *et al.*

The pre-existing complex refractive indices of crystalline $(NH_4)_2SO_4$ obtained at 298 K by Toon *et al*., though widely used, are inadequate to reproduce experimental extinction spectra accurately. We have determined a new set of optical constants at 298 K which better reproduce extinction features in $(NH_4)_2SO_4$ spectra, owing to more accurate, higher resolution values.

Chapter five: Validation of the shape and size distribution of ammonium sulfate aerosols using SEM technique

5.1 Introduction

The iterative retrieval procedure described in Section 2.2.1 is a commonly used method in our laboratory for *in situ* characterization of aerosols particles from their IR extinction spectra. The procedure is used to determine the number density, composition, phase and size distribution of laboratory aerosols, and with certain modification, atmospheric aerosols by means of remote sensing.[33,34] The capabilities of this method were tested in our laboratory, on six different types of aerosol particles. The tests were performed on aerosols of different shapes and sizes, including: spherical SiO_2, solid NaCl, $(NH_4)_2SO_4$, ice, liquid water, and nitric acid trihydrate. In the case of solid $(NH_4)_2SO_4$ aerosols, the good agreement observed between the experimental and calculated spectra using the new optical constants (see Chapter 4) suggests that the use of Mie theory in this method is appropriate, and hence, implies that the assumption of spherical particles is valid. To verify this assumption and the overall effectiveness of this numerical fitting procedure in the retrieval of aerosol size distribution, solid $(NH_4)_2SO_4$ aerosols were imaged using scanning electron microscopy (SEM) and the results of the two methods were compared. This study is done to confirm that under the experimental conditions used in this work, the aerosols were indeed spherical or near-spherical, which is consistent with the findings of previous studies of crystalline $(NH_4)_2SO_4$ particles.[55-57]

5.2 Experimental

The apparatus used in the SEM experiments is shown in Figure 5.1. The system is essentially the same as the one used in the optical constants experiments (Figure 4.1) with a few modifications which allow simultaneous collection of SEM samples and recording of infra red spectra. For the aerosol collection, an aluminum stub (1cm diameter) attached to a movable rod is placed in the center of the flow tube, 3 cm down stream from the observation cell. Special glue in the form of double sided carbon adhesive tab (Soquelec International) is applied on top of the aluminum stub, to increase the collection efficiency of the probe. A cooling system for the Nafion drying gas and a KOH dryer are added in order to improve drying and reduce particle agglomeration to minimum.

In this experiment ammonium sulfate aerosols were generated using solutions of 0.1M, 2M, and 3.5M. For all experiments the backing pressure of the atomizer was 35 PSI, but the sampling time and the drying flow rates were varied according to the concentration of the initial solution. The generated liquid droplets were dried in the Nafion dryer operated at 10-30 SLPM counter-flow rate. Prior to entering the Nafion dryer, the nitrogen gas is passed through the cooling system. This cooling system consists of a copper coil (2 m long with a 0.5 cm i.d) and an ice bath and decreases the temperature of the nitrogen flow to 10^0C. Previous experiments, where the efficiency of Nafion dryer under different operating conditions was tested (Annex 1), showed that at drying flow temperature of 10^0C the RH of the aerosol flow decreased to 7-10%. The drying process continues in the horizontal KOH dryer (50 cm long, 20 cm i.d., 1/3 filled with drying agent), positioned downstream from the Nafion dryer and connected to the flow system by flexible silicone tubing. At the exit of KOH dryer, the RH of the aerosol flow can be as low as 7-8% depending on the initial concentration of the atomized solution.

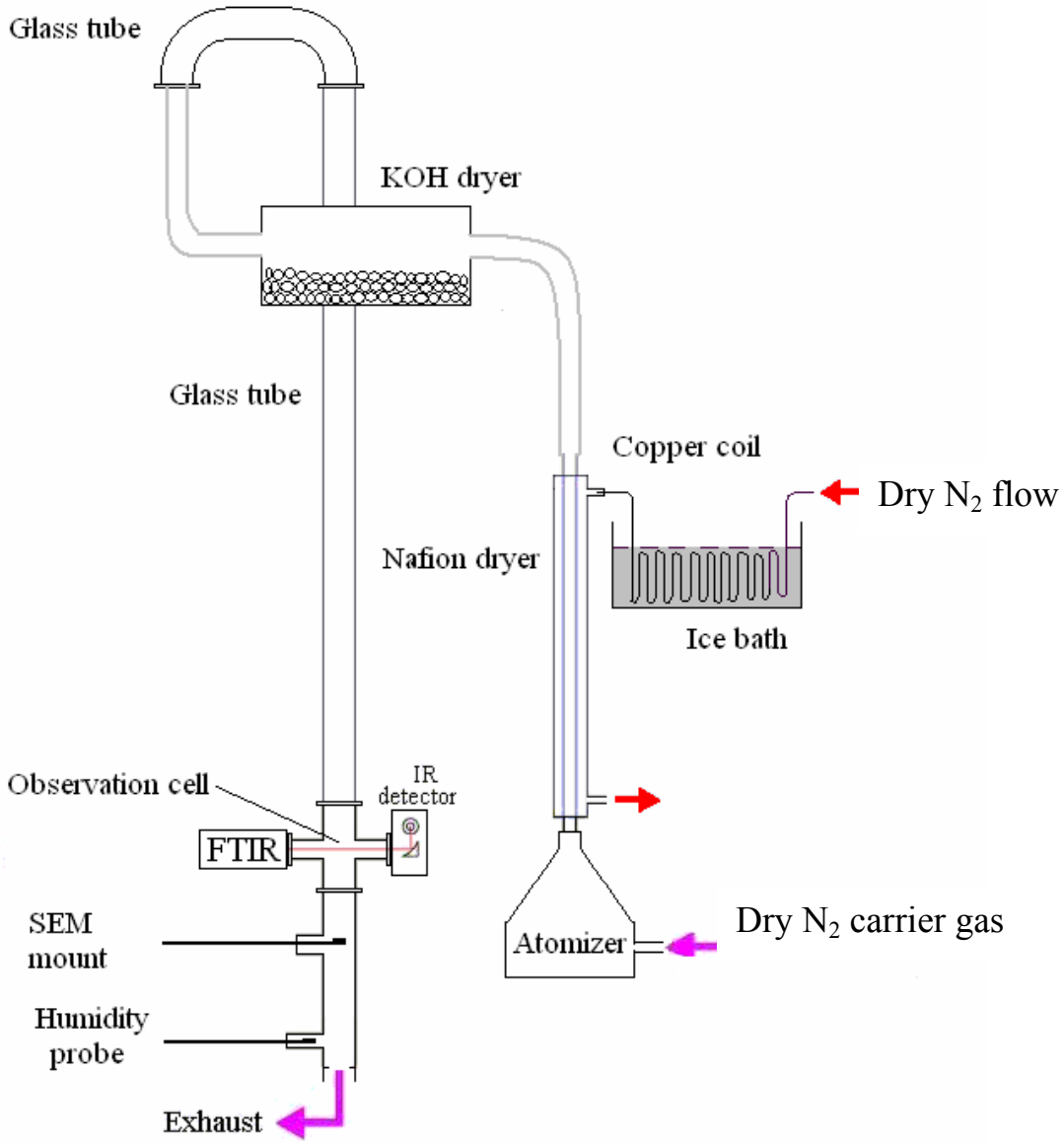

Figure 5.1: Schematic diagram of the room temperature glass flow tube used in the ammonium sulfate SEM experiments.

As already noted, ammonium sulfate solutions with three different concentrations were atomized to obtain different size aerosol particles and for each concentration a number of samples were acquired and analyzed. The operating conditions, including drying rates and sampling times, were optimized with respect to the concentration of solutions used. In the case of 0.1M solution, the RH of the aerosol flow was lowered down to 7% by using 30 SLPM cooled dry nitrogen and the sampling times were 30 and 60 minutes. In the experiments where a 2 M solution was atomized, sampling times were reduced to 10 and 15 minutes to reduce the number of agglomerates (that we suspected would increase with increasing particle size and concentration).

During sample collection, the RH of the aerosol flow was around 10%, reached by using a dying nitrogen flow rate of 10 SLPM. Further increase in the drying flow rate did not result in a decrease in RH. The aerosols produced from a 3.5 M solution were collected over 15 and 10 minutes sampling times. In this case, the RH of the aerosol flow and the flow rates are similar to the ones described for the 2 M solution experiment. To remove residual water, the obtained samples were kept in a $CaCl_2$ desiccator until further analysis. The aerosol samples prepared this way were then coated by a few nm of gold and imaged using a SEM.

5.3.1 Results and discussion

Figures 5.2.a and 5.2.b show SEM images of the samples obtained using a 0.1 M AMS solution and sampling times of 30 and 60 min. As it can be observed, there is a significant number of agglomerates on the samples collected over 60 min. However, as expected the 30 minutes sample had just a few agglomerates and the size and shape of individual particles was similar to that on the 60 minutes sample. A sharp decrease in the number of agglomerates with decreasing sampling time leads us to the conclusion that the coagulation of particles in the flow tube is highly unlikely. It appears that the agglomerates are primarily formed upon particle deposition on the probe during the collection process.

In the experiments where a 2 M solution was atomized, we noticed that a 15 minutes sampling time results in the appearance of a few agglomerates on the probe, whereas a 10 minute sampling time leads to a high number of well separated particles. Figures 5.3.a and 5.3.b show SEM samples obtained for 10 minutes sampling time and different magnifications. Zoom in images of this sample (Fig 5.3.b) shows that crystalline ammonium sulfate aerosols are indeed compact, near spherical particles.

It should be also noted that in the SEM images presented, some individual particles are bigger than it is likely to be produced by the atomizer. This can be attributed to the coalescence of liquid particles at the exit of the atomizer, the drying of which results in the occurrence of big spherical particles. In any case, the conclusion is that the SEM results do confirm that under the experimental conditions used in this work, the aerosols were indeed spherical or near-spherical, which is consistent with the findings of previous studies of crystalline $(NH_4)_2SO_4$ particles.[55-57]

a)

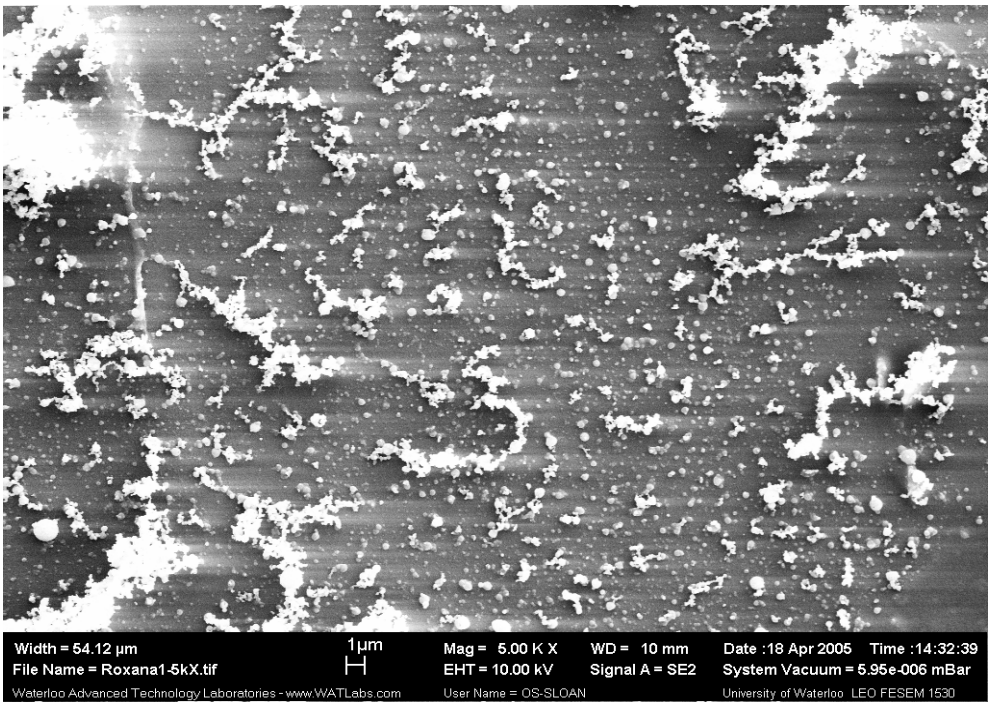

b)

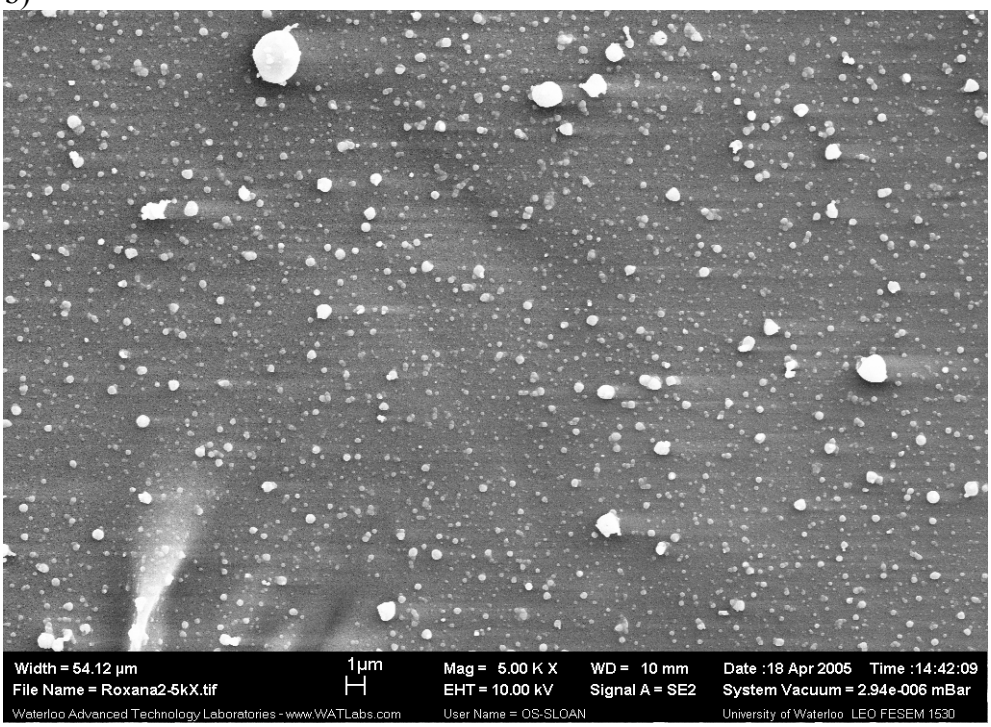

Figure 5.2: SEM images of ammonium sulfate particles generated from a 0.1M solution. a) sampling time 60 minutes, b) sampling time 30 minutes

a)

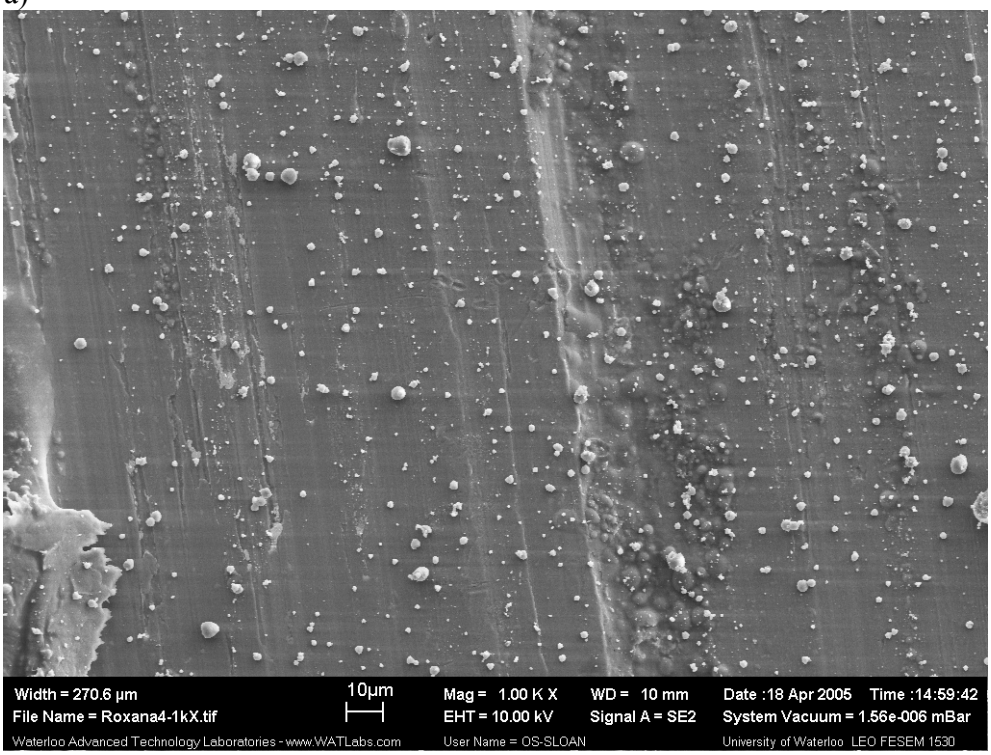

b)

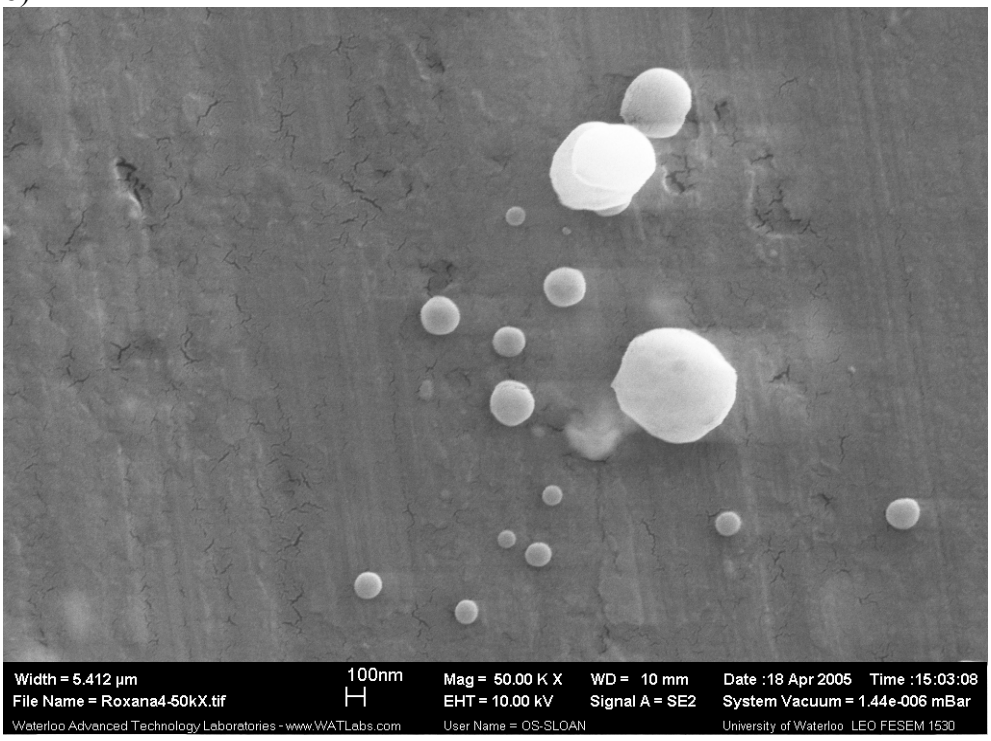

Figure 5.3: SEM images of ammonium sulfate particles generated from a 0.1M solution. a) magnification 1KX, b) magnification 50 KX.

5.3.2 Validation of size distribution (retrieval)

The SEM samples collected during this experiment were also used to obtain information about aerosol size distribution and compare it with the distribution retrieved from the IR experimental spectra, recorded during SEM sampling. It should be pointed out that the optical constants employed in the inversion method here are our newly derived optical constants, reported in Chapter 4.

The particle size distribution from SEM spectra was obtained by manually compiling a histogram for individual SEM images. The number of particles on the obtained and analyzed samples varies from 50 to 350 particles. By looking into a number of spectra we were able to conclude that the approximate location of the modes is obvious in samples as small as 50 particles and at least 150 particles are needed to obtain well defined, reproducible shapes of the modes. The sample showed in Figure 5.3 is one of the largest samples we had available, with 350 particles. We also checked the dependence of the size distribution on the presence of agglomerates. This was done by observing the difference in the histogram when agglomerates were simply excluded from the picture and the remaining particles counted, or when the particles comprising the agglomerated were also counted in individually. No visible effect was noticed on the shape of the retrieved distribution.

Figure 5.4 illustrates how the distribution obtained from the SEM image (histogram) and the distribution retrieved from the IR spectrum (solid line) compare. There is apparently a very good agreement between the two. The size distribution obtained applying the iterative method is multimodal with maxima at approximately 0.3, 0.6 and 1.0 μm, while the corresponding distribution obtained from SEM images also has a similar shape with two identifiable modes in the same locations as those obtained from FTIR. The agreement between the two size distributions gives evidence that the FTIR inversion method can be successfully used in determining the multimodal size distribution of the aerosol particles generated in our experimental setup.

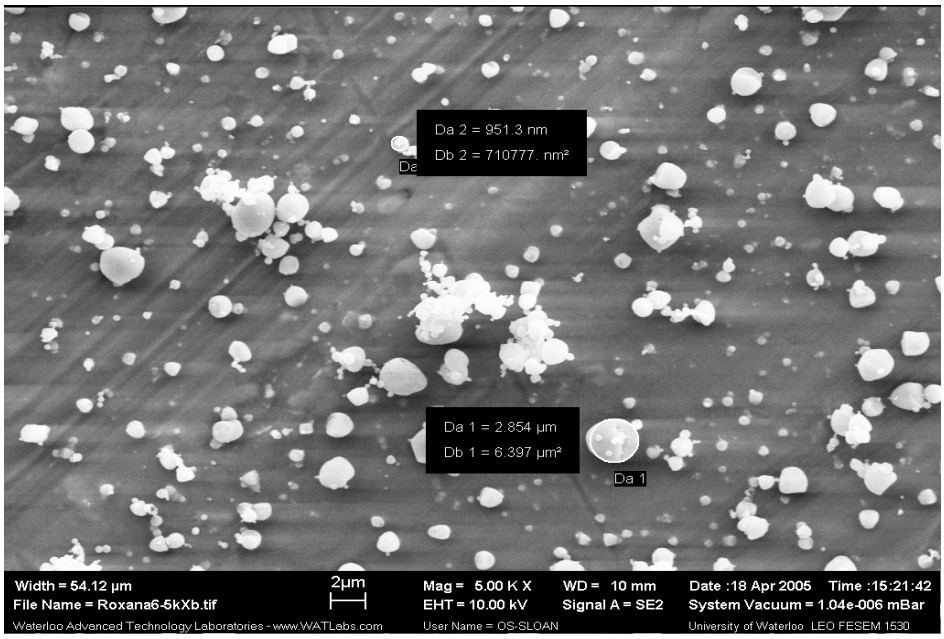

Figure 5.3 SEM image of ammonium sulfate crystalline particles generated by atomization of a 3.5M solution.

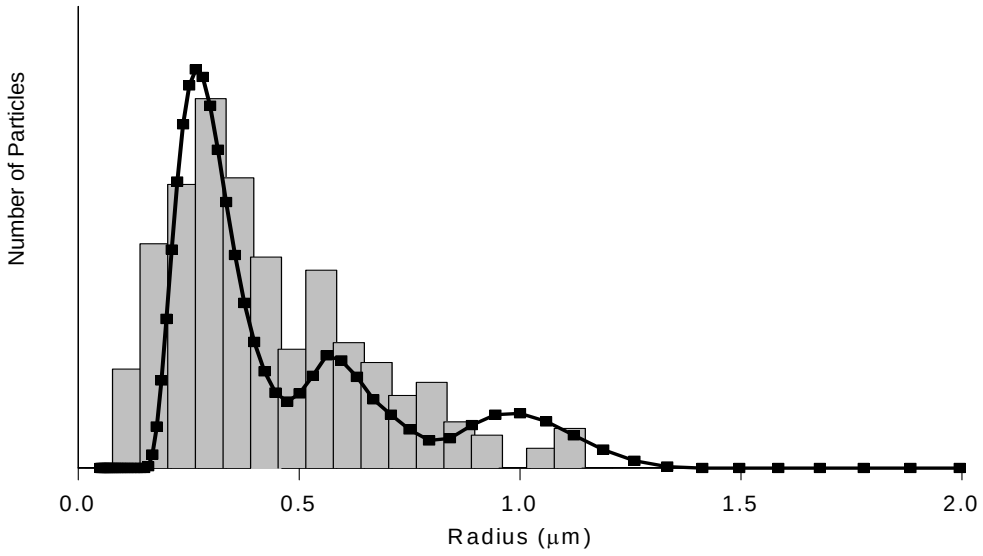

Figure 5.4 Number distribution of $(NH_4)_2SO_4$ particles retrieved from an experimental extinction spectrum (3.5M solution atomized) recorded during SEM sampling.

Chapter six: Determination of complex indices of refraction for ammonium sulfate solution

6.1 Introduction

It is well known that the aerosol optical constants change with particle phase and composition. In the most general sense, accurate optical constants for both solid and aqueous form of hygroscopic atmospheric aerosols are needed in order to "properly" estimate their effect on the radiative transfer. [47,58] In the case of this study, having accurate optical constants for the two phases is essential for the characterization of aerosols *in situ* (see Section 2.2.1) and the studies of their deliquescence process. In 2001 Martin et al. reported optical constants for aqueous ammonium sulfate derived from IR spectra at 298 K.[59,60]Previously, optical constants for ammonium sulfate were reported for 10% wt, 25% wt and 40% wt in the 14280-3780 cm^{-1} spectral range, at 24^{o}C (Gosse at al)[61], for 39% wt in the 2200-980 cm^{-1} spectral region, at 23^{o}C (Remsberg)[62] and for 18.5% wt, 28 %wt, and 35% wt in the 5200-400 cm^{-1}spectral range (Downing).[63] These spectra were recorded in a ATR experiment and cover a frequency range from 816 cm^{-1} to 3926 cm^{-1}. To test the quality of the available optical constants, a spectrum of liquid ammonium sulfate aerosol recorded in our apparatus was fitted by applying the procedure described in Section 2.3. The experimental spectrum shown in Figure 6.1 in black corresponds to 40% wt. liquid AMS aerosol, as determined indirectly from its equilibrium RH and AIM model (see Section 2.2.2). For the fitting, we used the most complete set of optical constants published by S. Martin.[60] In this particular case the optical constants for 40%w/w ammonium sulfate solution. The result is shown in Figure 6.1, where the calculated extinction spectrum is represented with a red line. It is apparent that S. Martin's optical constants are not accurate enough to generate a good fit and to be used for a reliable characterization of aerosols. The purpose of the work presented in this chapter was to obtain a more accurate set of optical constants for a range of compositions of ammonium sulfate solution and use them for the characterization and the deliquescence studies of AMS aerosols.

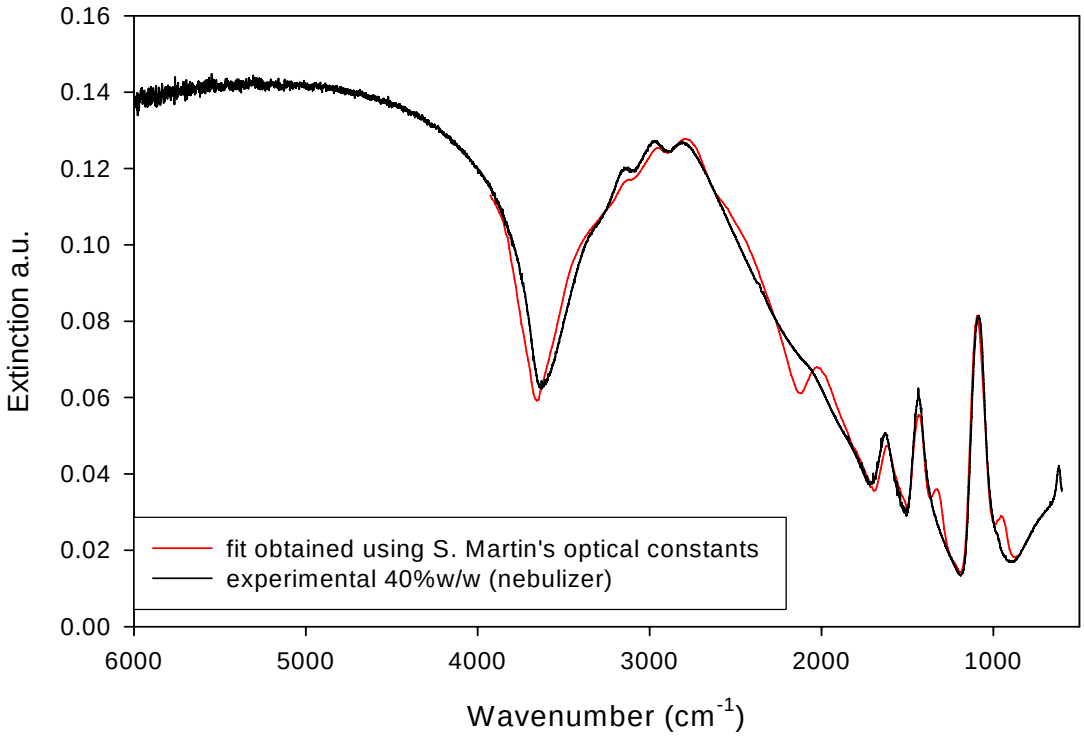

Figure 6.1: An example of the fit (for an experimental spectrum) obtained using S. Martin's optical constants

6.2 Experimental

The experimental set up used in this study was essentially the same as the one used in the study for determination of optical constants for crystalline AMS, described in Chapter 4. The difference is that, in this study, the Nafion dryer was used either as a dryer or a humidifier, depending on the experimental conditions required. 0.1M, 0.5M, 1M and 2M ammonium sulfate solutions were atomized to produce aerosols of 40%, 35%, 30%, 25%, 20%, 15%, 10%(w/w) aqueous concentration. Table 6.1 summarizes operating conditions used in the experiments for each of the above listed aerosol concentration.

Table 6.1: Operating conditions used in experiments for different aerosol concentration

Aerosols concentration (w/w)	Concentration of the atomized solution (M)	Drying N_2 flow (SLPM)	Humid N_2 flow (SLPM)	Experimental RH of the gas in equilibrium with aerosols (±0.5%)	Theoretical RH of the gas in equilibrium with aerosols (%)
40%	1M	0.25	-	82.3	82.8
35%	0.5M	0.5	-	86.1	86.4
30%	0.5M	0.25	-	89.0	89.3
25%	2M	0	-	91.5	91.8
20%	1M	-	1	93.9	93.8
15%	0.1M	0	-	95.6	95.6
10%	0.1M	0	-	97.2	97.1

The carrier gas flow rate was constant, around 3.3 SLPM in all the experiments. Prior to the experiments, a calibration curve is generated and the water vapor spectra recorded in this experiment were used to subtract water vapor (absorption features) from the ammonium sulfate spectra. During experiments the RH of the aerosol flow was also measured directly by the Vaisala probe. The total length of the flow tube of around 3 m, was chosen so that the aerosols reaching the observation cell are well in equilibrium with the carrier gas and with the glass walls. The recorded RH of aerosols is their RH at equilibrium and this value was used to determine the aqueous concentration of the aerosol particles using the AIM thermodynamic model. The theoretical RH (column 6, Table 6.1) is the humidity at which aerosol droplets, in equilibrium with their surroundings, will have the concentration specified in the first column of Table 6.1.

Figures 6.2 through 6.5 show the original and "subtracted" (water vapor and CO_2 absorption lines are removed from the spectrum) AMS spectra ranging from 40% to 10% wt. solution concentration, used to derive the new set of optical constants. The recorded spectral range from 6000 to 500 cm^{-1} includes all four absorption modes corresponding to ammonium sulfate.

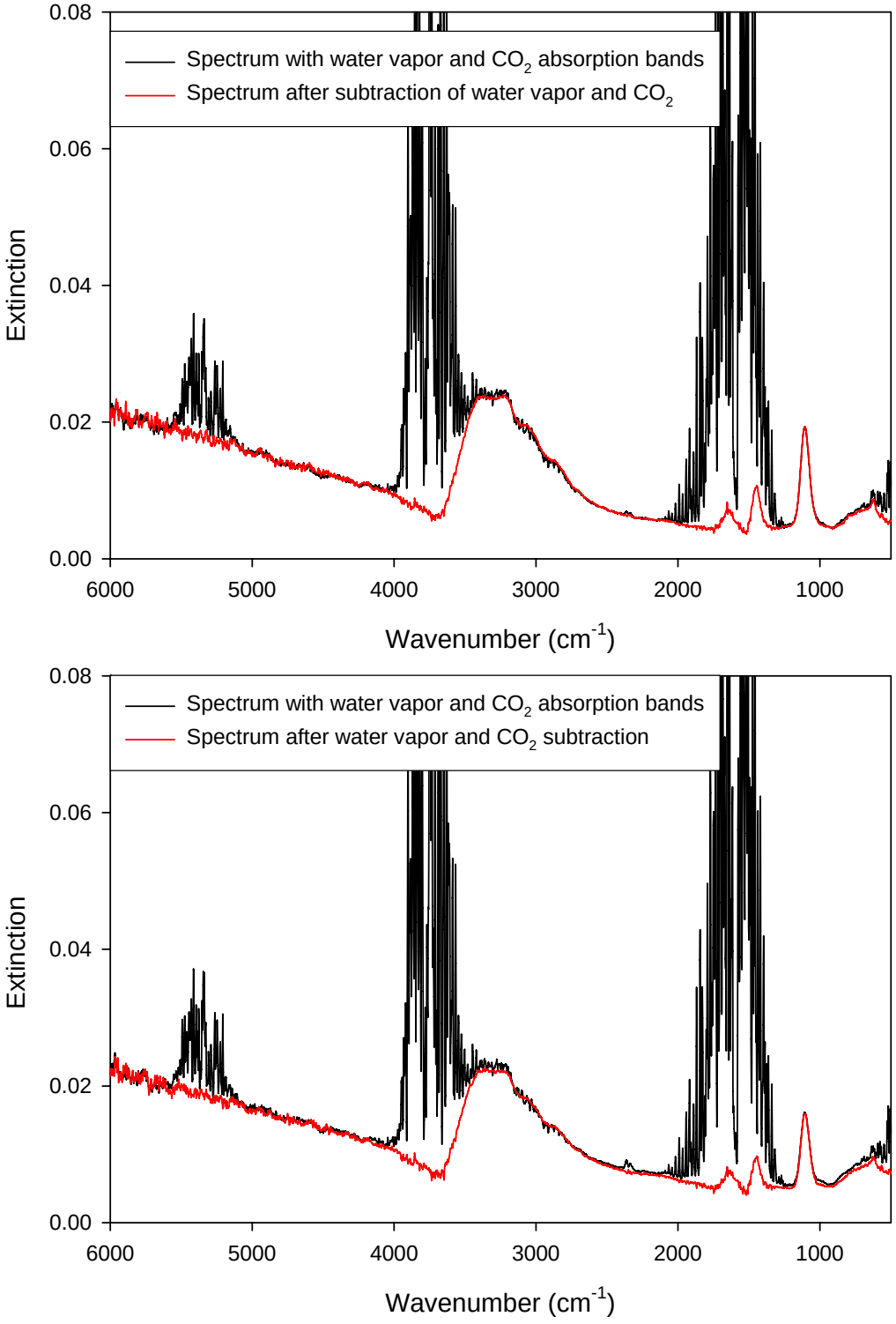

Figure 6.2: Experimental spectra of 40% wt $(NH_4)_2SO_4$ (top) and 35 wt % $(NH_4)_2SO_4$ (bottom) particles.

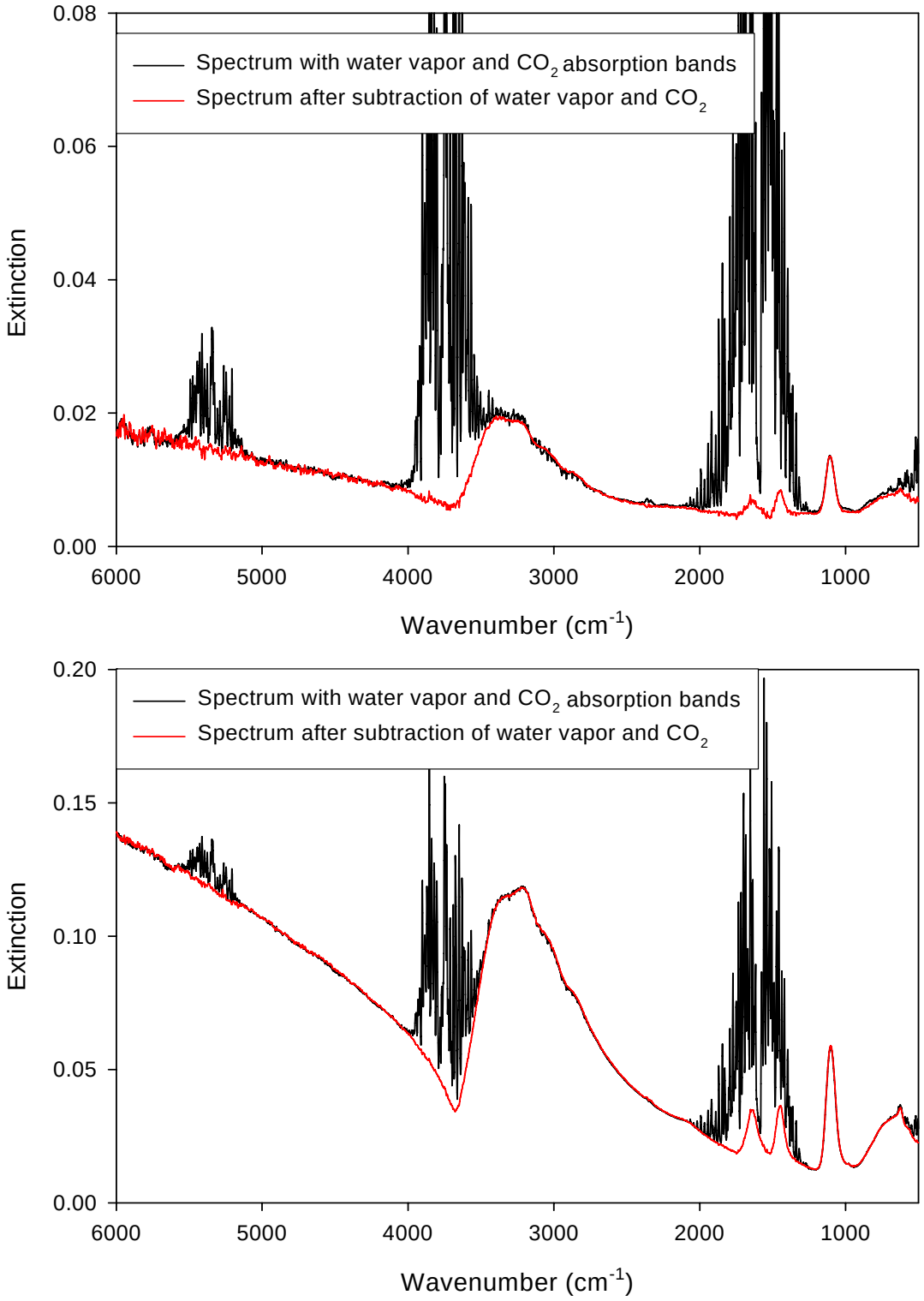

Figure 6.3: Experimental spectra of 30% wt $(NH_4)_2SO_4$ (top) and 25% wt $(NH_4)_2SO_4$ (bottom) particles.

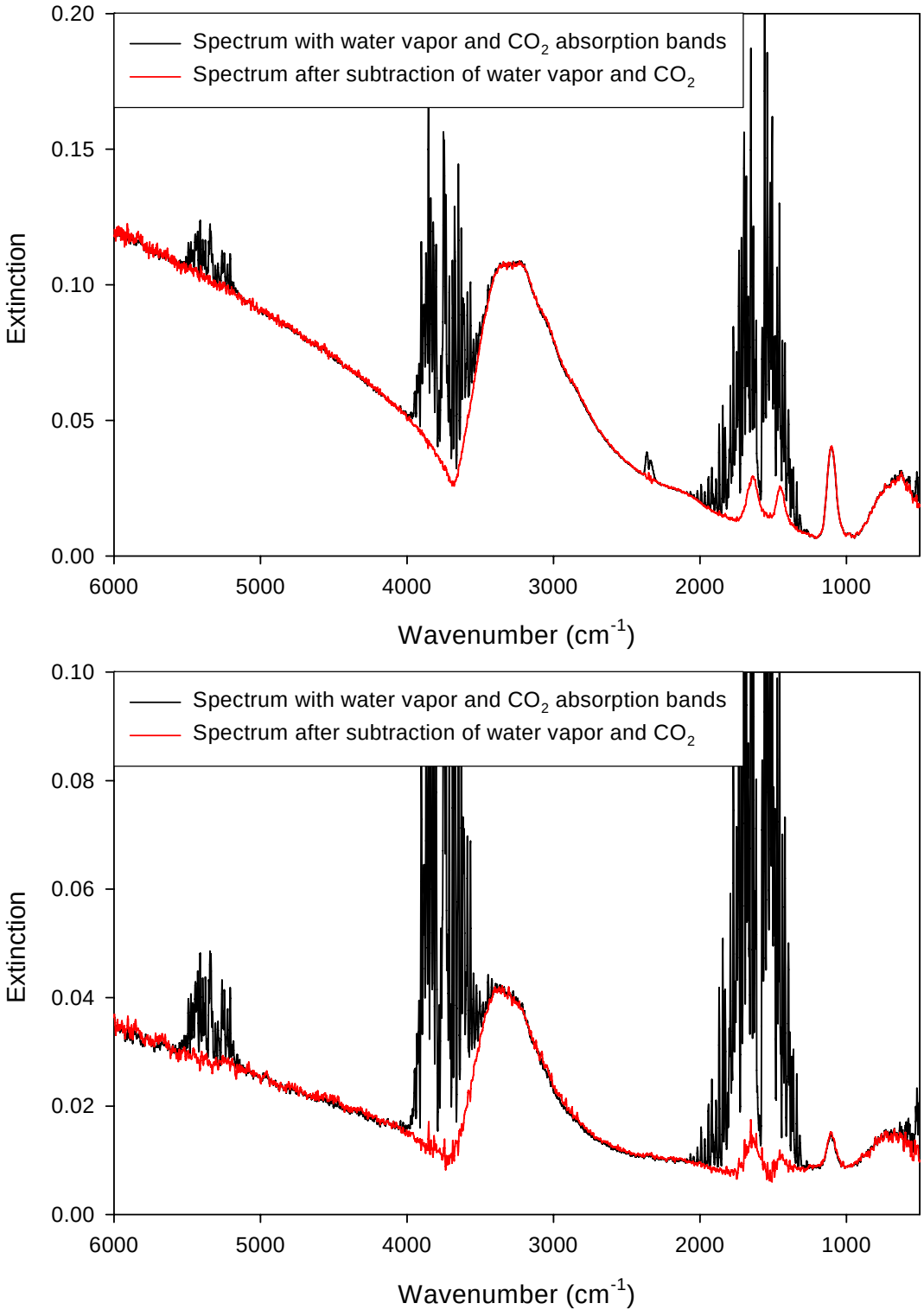

Figure 6.4: Experimental spectra of 20% wt $(NH_4)_2SO_4$ (top) and 15% wt $(NH_4)_2SO_4$ (bottom) particles.

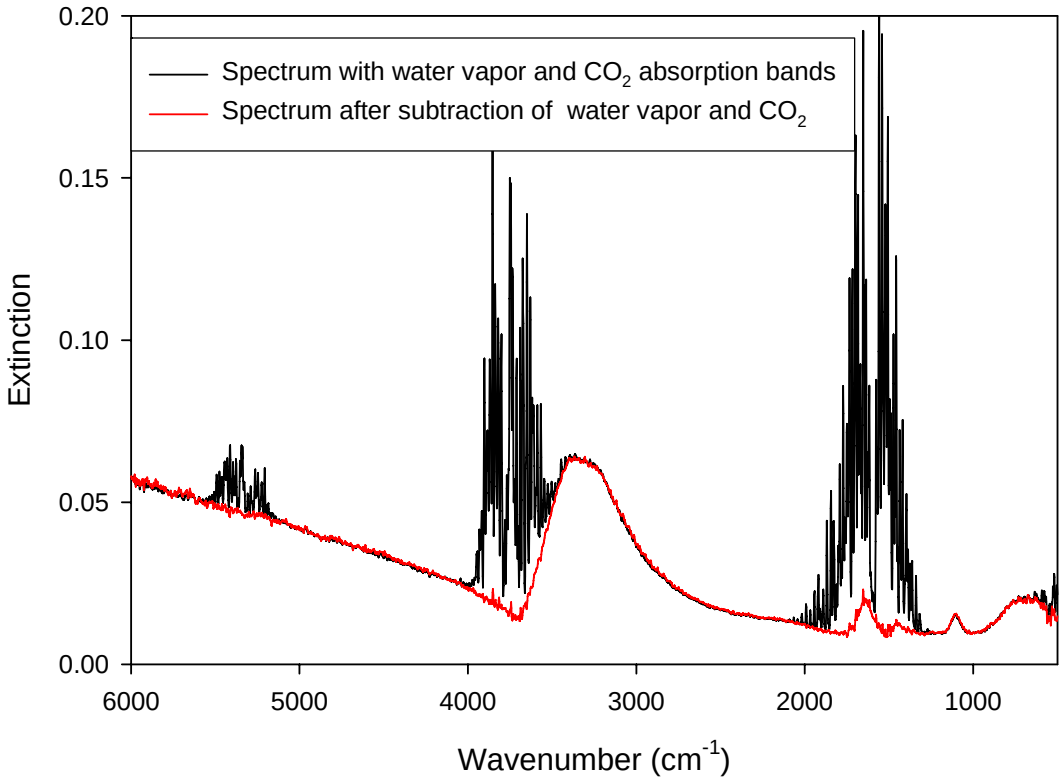

Figure 6.5: Experimental spectra of 10% wt $(NH_4)_2 SO_4$.

It can be seen that the experimental spectrum generated from 0.1M has noticeably more noise than the one from 2 M, which is expected since a high initial solution concentration leads to the generation of bigger aerosol particles and subsequently to a higher S/N ratio.

In principle, it would have been advantageous if all the aerosol compositions could have been obtained from 2 M or 1 M solutions, which would have resulted in spectra with minimal noise. In practice, however, that was not possible to achieve due to frequent clogging of the TSI atomizer when working with highly concentrated solutions.

In addition to the dry $(NH_4)_2SO_4$ spectral features described in Chapter 4, the extinction spectrum for aqueous ammonium sulfate shows the presence of condensed phase water absorption bands superimposed on the ammonium sulfate absorption bands.

The absorption bands corresponding to condensed phase water (OH-stretch, HOH-bend and H bond) located at 3450, 1640 and 650 cm^{-1}, have a similar position as in the pure water spectrum. As the concentration of ammonium sulfate in the aerosol particles decreases, the absorption bands of $\nu_4\left(NH_4^{+}\right)$ and $\nu_3\left(SO_4^{-2}\right)$ broaden and shift to a higher frequency (by a few wavenumber)[64,65].

6.3 Results and discussion

As discussed earlier, the inversion method for the retrieval of refractive indices requires an initial guess for k(v). In order to employ the imaginary part of the refractive index from Martin's data as an initial guess for the calculation of new optical constants, the Scott Martin's data were extended from 816-4000 cm^{-1} to our experimental range of 600-6000 cm^{-1}. This is essential since the data in the missing spectral ranges contain valuable qualitative and quantitative information on the ammonium sulfate sample. The region 600-816 cm^{-1} includes the $\nu_4\left(SO_4^{-2}\right)$ absorption peak that gives information about the composition of the aerosol particles, whereas the region above 4000 cm^{-1} (especially significant in the case of bigger particles, with increased scattering activity) could be important when determining the size of the aerosol particles. The imaginary part of Scott Martin's optical constants was thus extended to 600 cm^{-1} using two Lorentzians and an exponential curve given by:

$$A/(f^2+f2^2)+B/(f^2+f3^2)+C*e^{(D*(f1-f)}$$

where A,B,C are amplitude factors. The high frequency end was extended to 6000 cm^{-1} based on the assumption that in this wavelength range the imaginary part values are equal to those at 4000 cm^{-1}.[60] The new optical constants are then calculated applying the procedure described in Section 2.3. The anchor point n_∞ for each concentration of ammonium sulfate solution is calculated from Koop's data in VIS, for the real part of the refractive index, at 298 K and 1μm. No change in the optical constants was noticed when derived again using n_∞ values at 0.35 μm. The values of the anchor points at 1 μm, used in the final calculations, are presented in Table 6.2.

Table 6.2: The anchor point used for each concentration

AMS aerosols aqueous concentration w/w	Anchor point, n_∞
40%	1.393072
35%	1.385033
30%	1.377207
25%	1.369579
20%	1.362132
15%	1.354840
10%	1.347742

New optical constants for seven different compositions are thus generated for the extended frequency range of 600-6000 cm^{-1} at the resolution of 2 cm^{-1}. The *n* and *k* values derived in the present work for 40% AMS are presented in Figure 6.6 along with the original S. Martin's data. The comparison shows a good agreement for both n and k in the spectral region from 1700 to 2650 cm^{-1}. By examining the real part of the refractive index it can be observed that in the region below the 1700 cm^{-1} HOH-bend, $\nu_4\left(NH_4^{+}\right)$ and $\nu_3\left(SO_4^{-2}\right)$ peaks retrieved in this study are systematically lower than S. Martin's data, by up to 3 %. In the region 2650-3250 cm^{-1}, corresponding to $\nu_3\left(NH_4^{+}\right)$ peak, the intensity of our peak about 1% higher. The biggest discrepancy between the two data sets is in the spectral region from 3400 to 3700 cm^{-1}. In the case of the imaginary part, we observed a slight difference in the shape of the $\nu_3\left(SO_4^{-2}\right)$ peak, this peak being broader in our case. Furthermore, in the spectral region between 2700 and 3500 cm^{-1}, S. Martin's curve overshoots ours by almost 4%. These observations are valid for all concentration.

Once the optical constants are retrieved, an extinction spectrum can be calculated applying Mie theory and the procedure previously described in Section 2.3. Figure 6.7 illustrates the difference between the experimental spectrum of 40% AMS aerosols and the fits calculated using data from the present work data and S Martin's data.

An excellent agreement was observed between the experimental spectrum and our fit, whereas S. Martin's fit apparently underestimates the extinction values at 2050-2250, 1375-1400 and 1125-1200 cm^{-1} and overestimates them at around 1500 cm^{-1}.

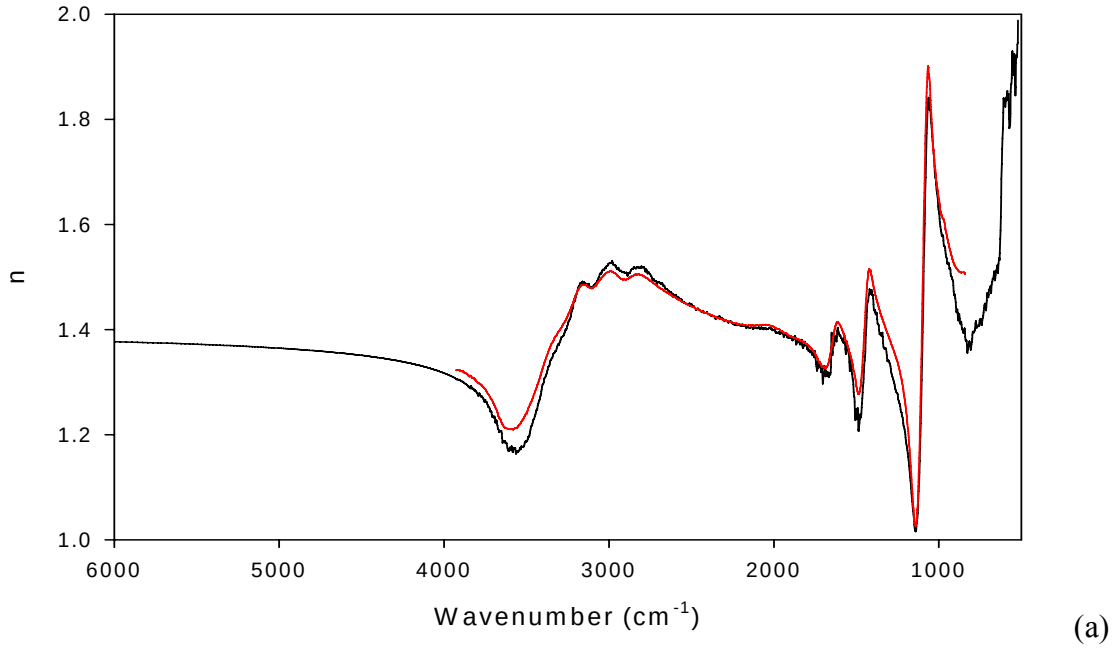

(a)

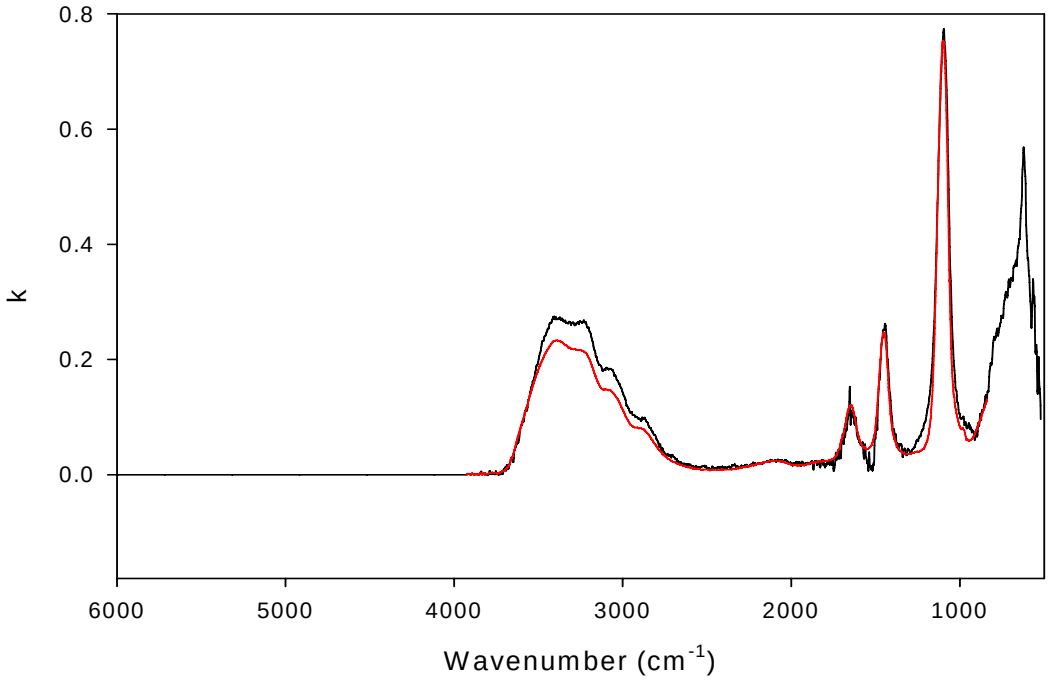

(b)

Figure 6.6: Comparisons between S Martin's and present work, real part (a) and imaginary part (b) of the refractive index at 40% w/w AMS. The black line represents the result of the present work for 40% AMS, while the red line represents S Martin's data.

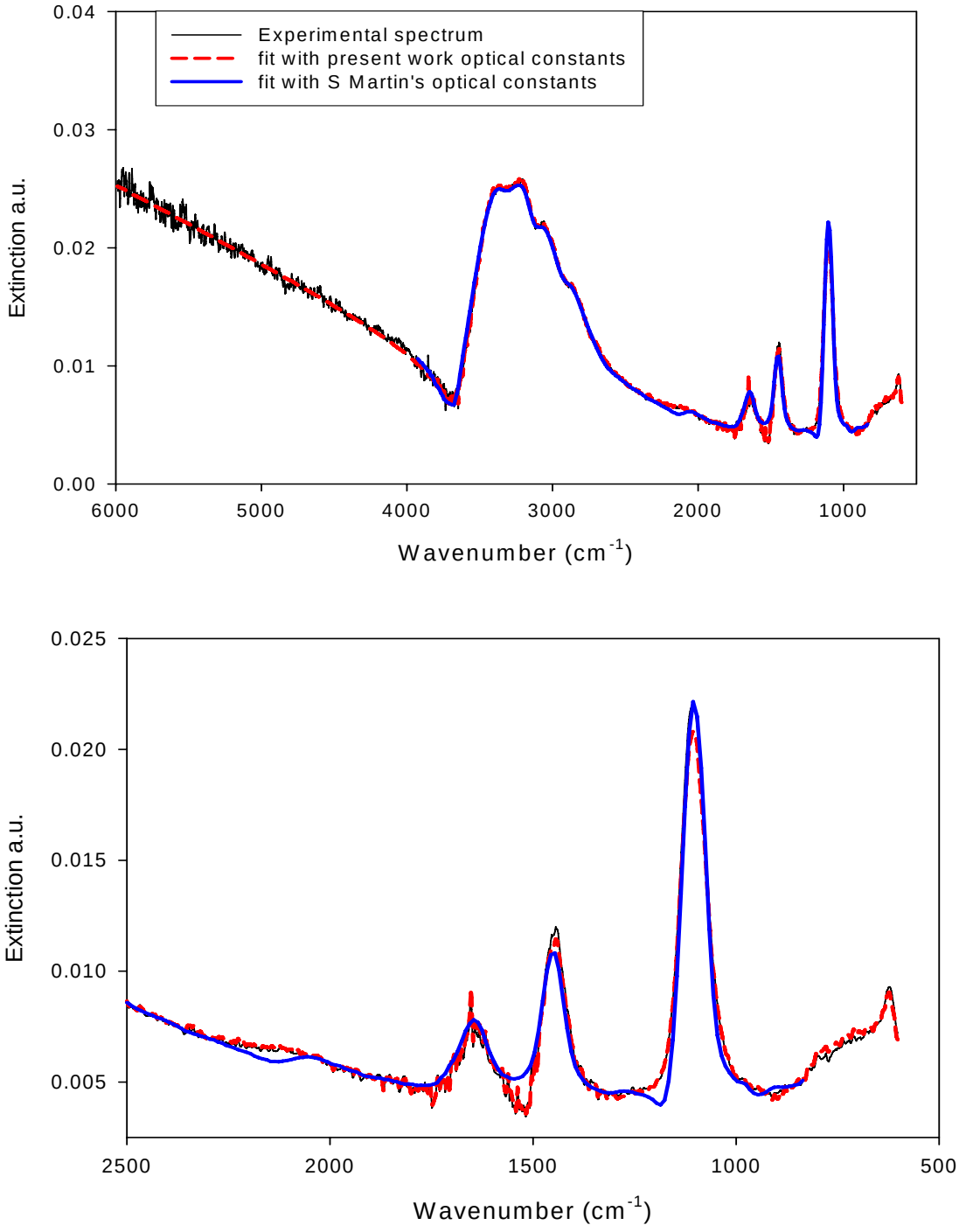

Figure 6.7: Experimental extinction spectrum for 40% AMS aerosols (black line) with fits from present work data (dashed red line) and S Martin's data (blue line)

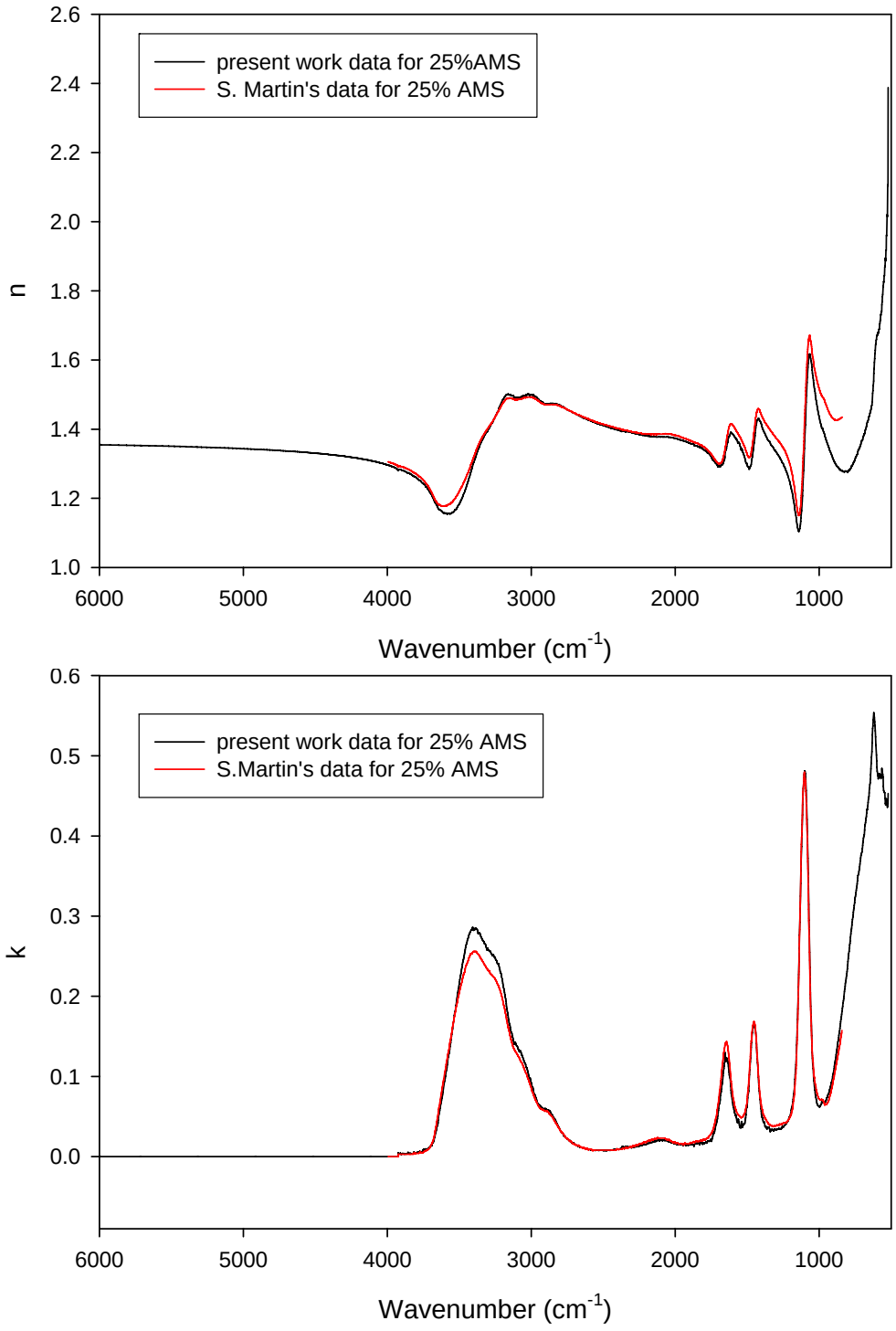

Figure 6.8: Comparison of S. Martin's and present work, real part (a) and imaginary part (b) of the refractive index at 25% w/w AMS. The black line represents the result of the present work for 25% AMS, while the red line represents S Martin's data.

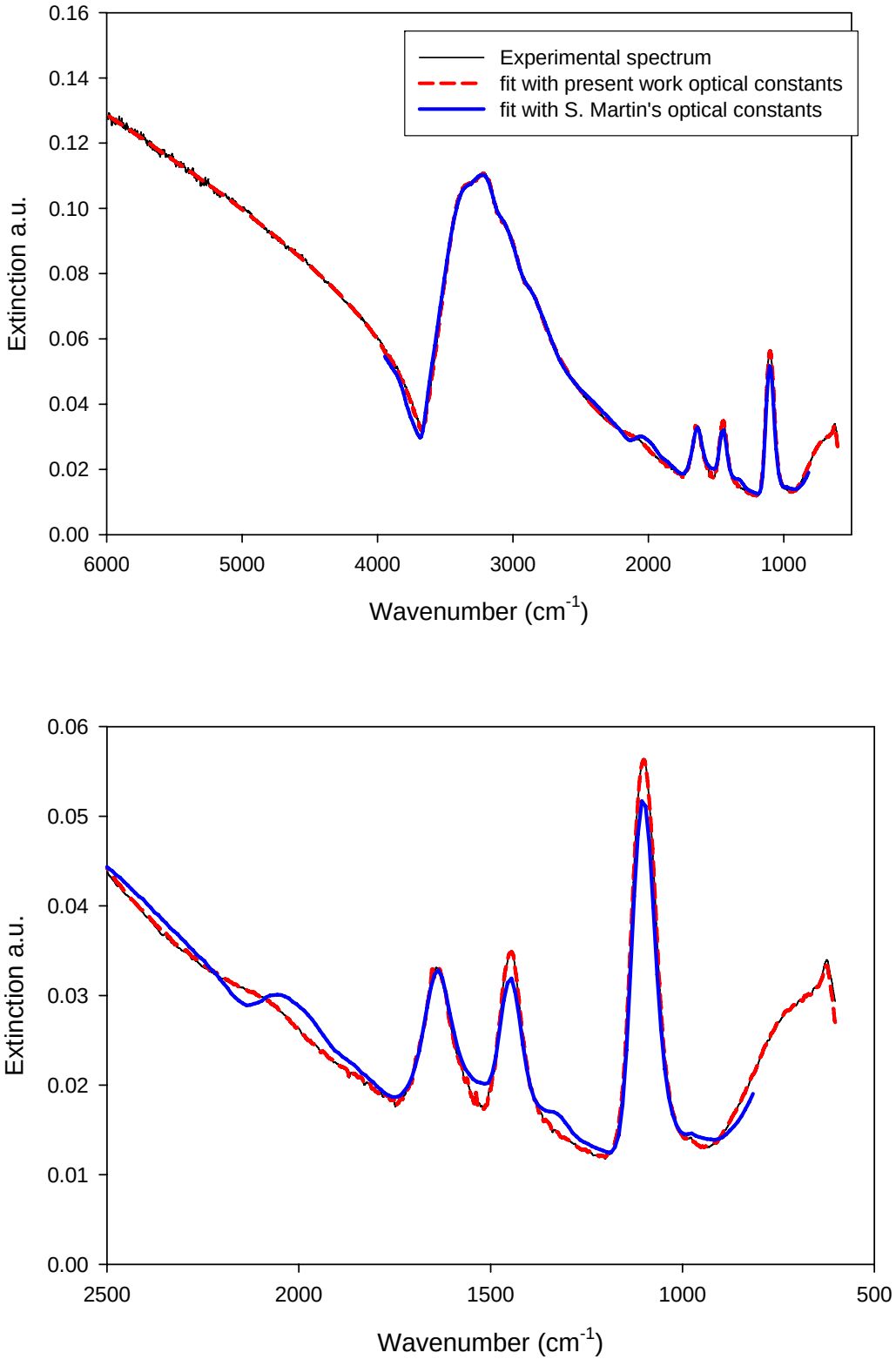

Figure 6.9: Experimental extinction spectrum for 25% AMS aerosols (black line) with fits from present work data (dashed red line) and S Martin's data (blue line)

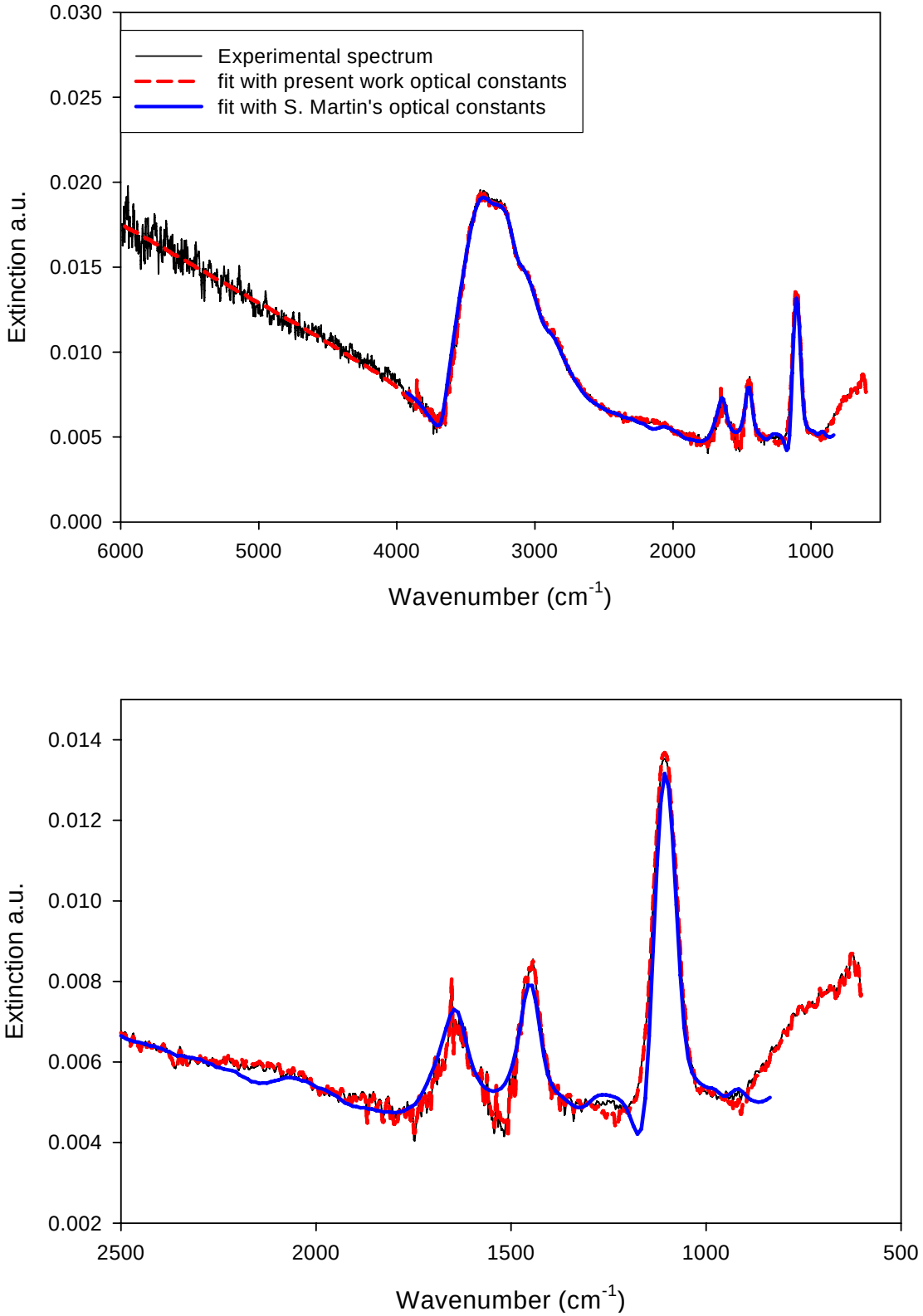

Figure 6.10: Experimental extinction spectrum for 30% AMS aerosols (black line) with fits from present work data (dashed red line) and S Martin's data (blue line)

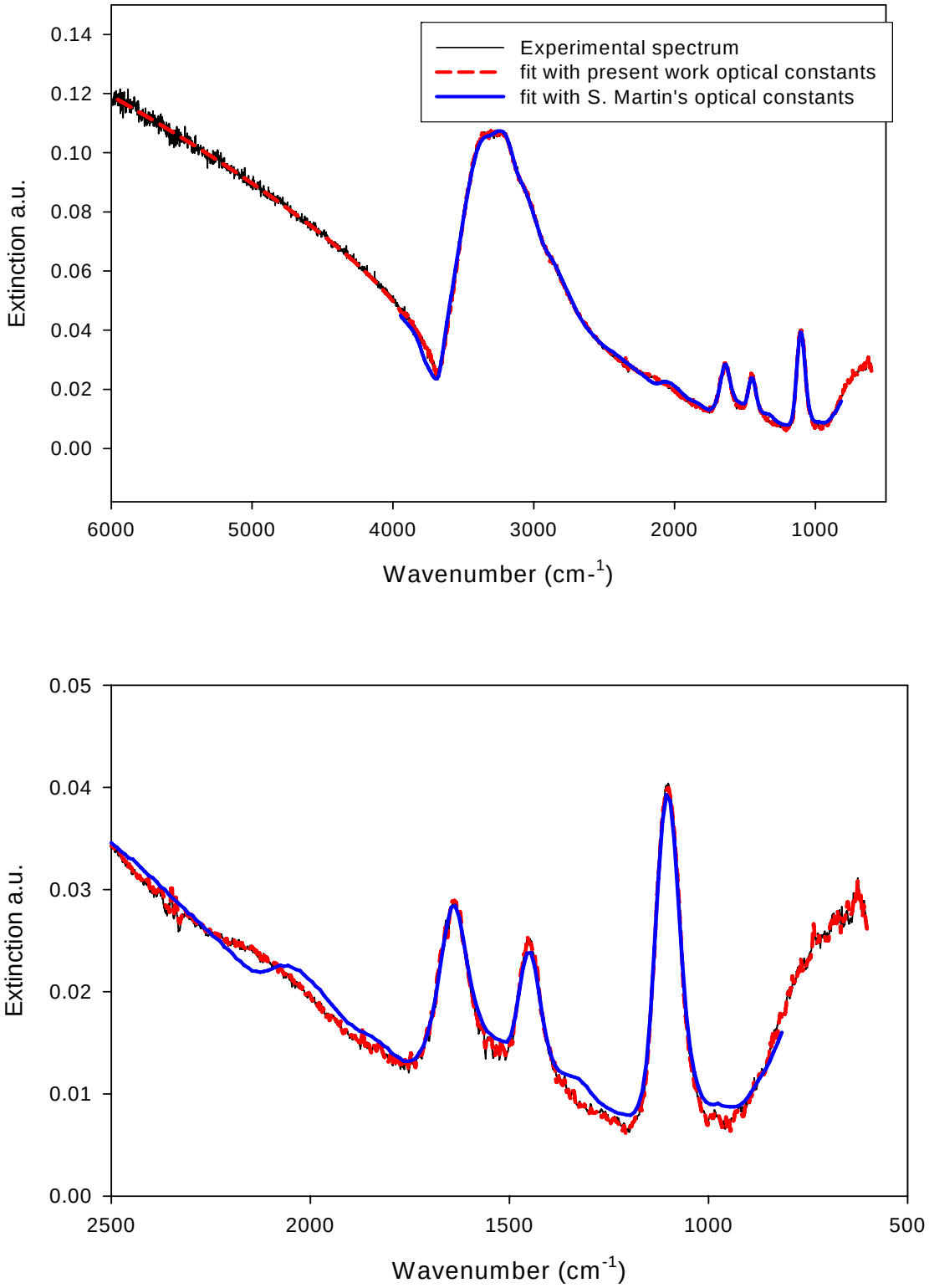

Figure 6.11: Experimental extinction spectrum for 20% AMS aerosols (black line) with fits from present work data (dashed red line) and S Martin's data (blue line)

6.4 Retrieval sensitivity to spectral range

The size and the number density of the aerosol particles is determined by applying the retrieval procedure, described in Section 1.4, to an experimental IR extinction spectrum. When illuminated by an infrared beam, ammonium sulfate particles scatter and absorb light. Previous studies showed that the computed scattering cross-section gives information about the size of the aerosol particles, whereas the measured absorption cross-section provides valuable information on the aerosol composition. [66] Scattering and absorption cross sections are functions of the real and imaginary part of the refractive index and as shown in Section 1.4 the optical constants vary strongly with frequency. Therefore the accuracy of the retrieved size distribution might be affected by the frequency range of the IR extinction spectrum.

To test the sensitivity of the retrieval method to different spectral ranges (within the 600-6000 cm^{-1} where ammonium sulfate exhibits scattering and absorption) we applied it to the experimental extinction spectra of a 25% wt AMS solution aerosol, shown previously in Figure 6.3 (bottom). Figure 6.12, again shows the same experimental spectrum for 25% wt AMS aerosol particles (represented here by the black line), and the fits calculated using the entire spectral range (red line), and sub-ranges 840-3930 cm^{-1} (green line) and 840-6000 cm^{-1} (dashed blue line). All fits were computed using the new optical constants for 25% wt AMS reported in this chapter. An excellent agreement between the experimental spectrum and the fit is observed in all cases. The corresponding retrieved size distributions are shown in Figure 6.13. The red line again shows the retrieved size distribution when the entire range (600-6000 cm^{-1}) is employed. The solid green and dashed blue lines represent the size retrieved when the range is limited to 840-3930 cm^{-1} and 840-6000 cm^{-1}, respectively.

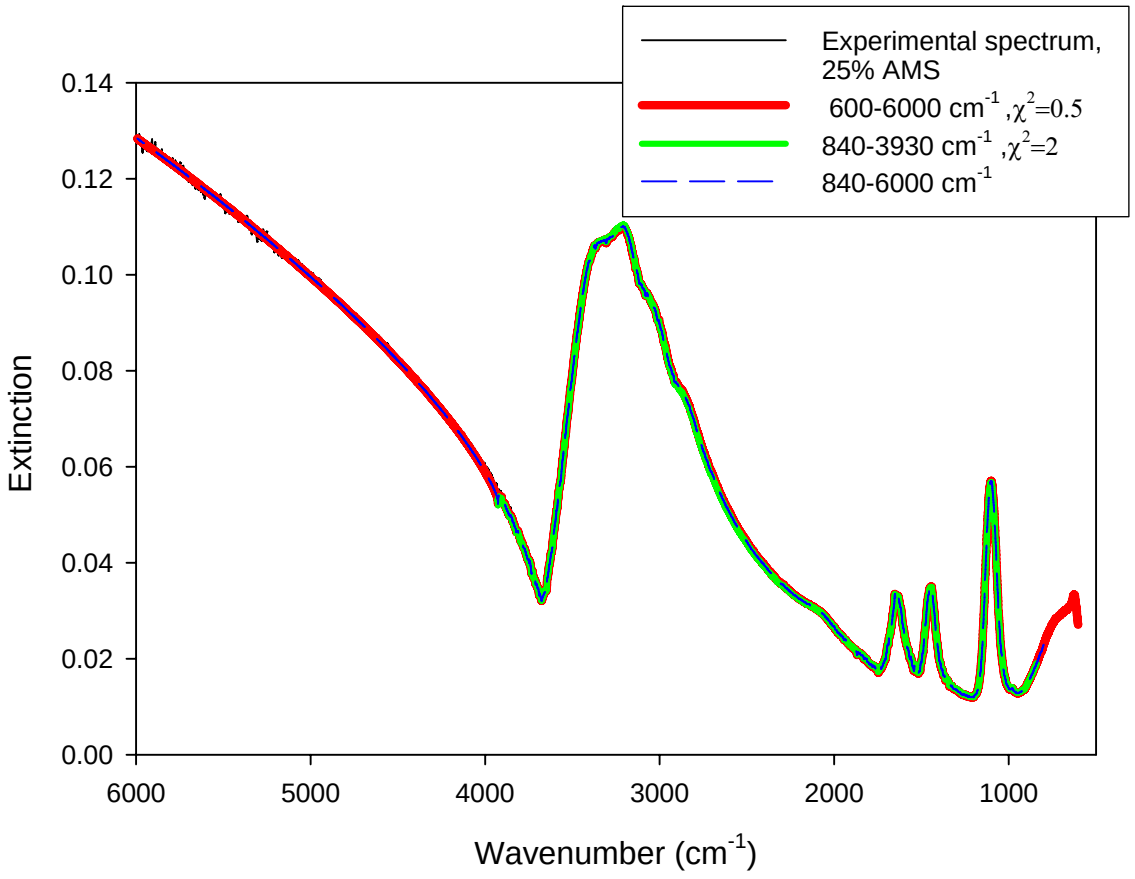

Figure 6.12: Extinction spectra of $(NH_4)_2SO_4$ aerosols with best calculated fits for different spectral ranges.

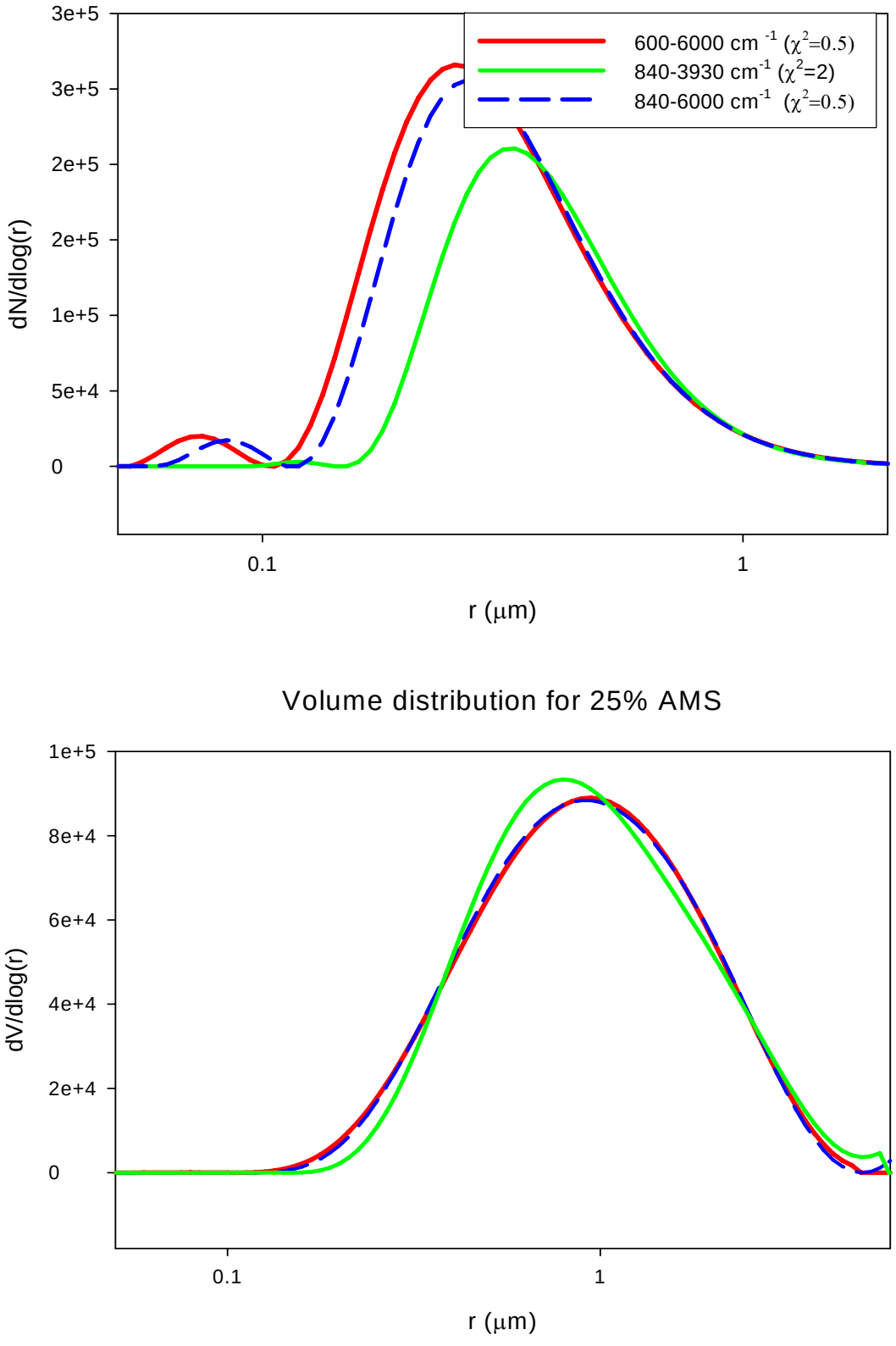

Figure 6.13: Number (top) and volume (bottom) distribution retrieved from an IR experimental spectrum of 25 wt % $(NH_4)_2SO_4$ particles.

In the frequency range above 4000 cm^{-1}, the scattering efficiency of a particle increases with increasing frequency, thus excluding this part of the spectrum is expected to effect primarily the size distribution. The composition of aerosol is not affected by the removal of this spectral range because ammonium sulfate has no absorption bands in this region (the imaginary part of the refractive index in this range is almost zero - as it can bee seen in Figure 6.8). Both the number and volume distribution retrieved for ammonium sulfate aerosol particles support this idea. Figure 6.13 shows no significant difference in the size distribution when the spectral rage is reduced to 840-6000 cm^{-1}.The excluded part of the spectrum is thus important in retrieving information about the composition and phase of aqueous aerosols. A noticeable change in the size distribution is seen when the frequency is in the range between 840 to 4000 cm^{-1}.In this case the mean radius of the number distribution shifts up by 20-25% and the total volume by up to 3%.These results lead to the conclusion that a higher spectral range increases the accuracy in determining chemical composition, phase and size of aerosol particles.

Chapter seven: Deliquescence of ammonium sulfate aerosol

7.1 Introduction

To test our newly designed flow tube and the tools developed for aerosols characterization, a standard deliquescence experiment on ammonium sulfate aerosols was performed as a preparatory step for the kinetic study. The ammonium sulfate deliquescence was extensively studied in the past (by several groups), using a tandem differential mobility analyzer [67,68] and a temperature controlled flow tube system [17,23,69,70]. An example of an ammonium sulfate deliquescence curve obtained by Tang and Munkelvitz (Figure 1.6) in one of such studies was already shown in Section 1.5. In that particular study, the deliquescence process was observed at 80% RH. The DRH values reported in numerous studies somewhat differ (e.g. Gysel,80±1.2%; Colberg,80±2%; Biskos,79±2.5%), however within the given uncertainties, they are all in good agreement, including with the theoretical value of 79%, obtained from thermodynamic calculations.[71-73]

The goal of this experiment was to generate our own deliquescence curve and compare the results with those reported by other groups, obtained using different experimental methods. The result of this test-study is expected to give us a better insight into the accuracy and sensitivity of our experimental method, and of the procedure used for the determination of aerosol composition. Since the deliquescence curve depicts the change in liquid water content in an aerosol particle as a function of the ambient relative humidity, it is essential that both these properties be measured or determined accurately. For that purpose, the RH in this particular experiment is determined by both direct measurements using Vaisala probe and the integration of water vapor absorption band from IR spectrum. The aerosol composition is determined by employing the retrieval method described in Section 2.2.2, as well as by applying Clegg's AIM thermodynamical model.

7.2 Experimental setup

The schematics of the apparatus used for the room temperature deliquescence experiments are shown in Figure 6.1. The set up consists of two Nafion dryers connected in a series, a humidifier, a glass tube (120 cm long) and the deliquescence reactor, leading to the observation cell. The ammonium sulfate aerosols were generated by a Burgener Mira Mist nebulizer from 2 M aqueous solution of AMS. The Vaisala humidity probe was placed downstream from the observation cell, as earlier described in the general experimental set up (see Section 3.8). The aerosol droplets were dried by passing aerosol flow through a series of two Nafion dryers (100 cm and 50 cm long, respectively). The RH of the aerosol at the exit of the dryers was determined by closing off the humidifier (i.e. by closing the inlet and outlet of the humidifier jacket) and measuring the humidity of the flow at the exit of the observation cell by Vaisala probe and from IR spectra using calibration curve. The humidity of the dried aerosols was less than 12% which is, for practical purposes, considered dry.

In operational mode, the humidifier jacket is supplied with a flow of (humid) nitrogen (humidified in atomizer), as described in Section 3.6, while the deliquescence reactor is kept closed. During the experiment, the humid sheath flow of the Nafion humidifier was increased stepwise starting from 2 l/min to 4 l/min, resulting in a gradual increase of the RH of aerosol leaving the humidifier from 57.7±0.5% to 81.2±%. Downstream from the humidifier there is no more exchange of water vapor, allowing the aerosol to reach (thermodynamic) equilibrium with the carrier gas by the time their IR spectra are recorded in the observation cell. This should be a realistic assumption considering the time necessary to saturate an aerosol particle is estimated to be a few tenths of a second,[64] almost three orders of magnitude smaller that the residence time of aerosols in the flow tube (the residence time of aerosols particles in the flow tube, from the exit of the humidifier to the observation cell, is 162 s for the experimental conditions mentioned for this study).

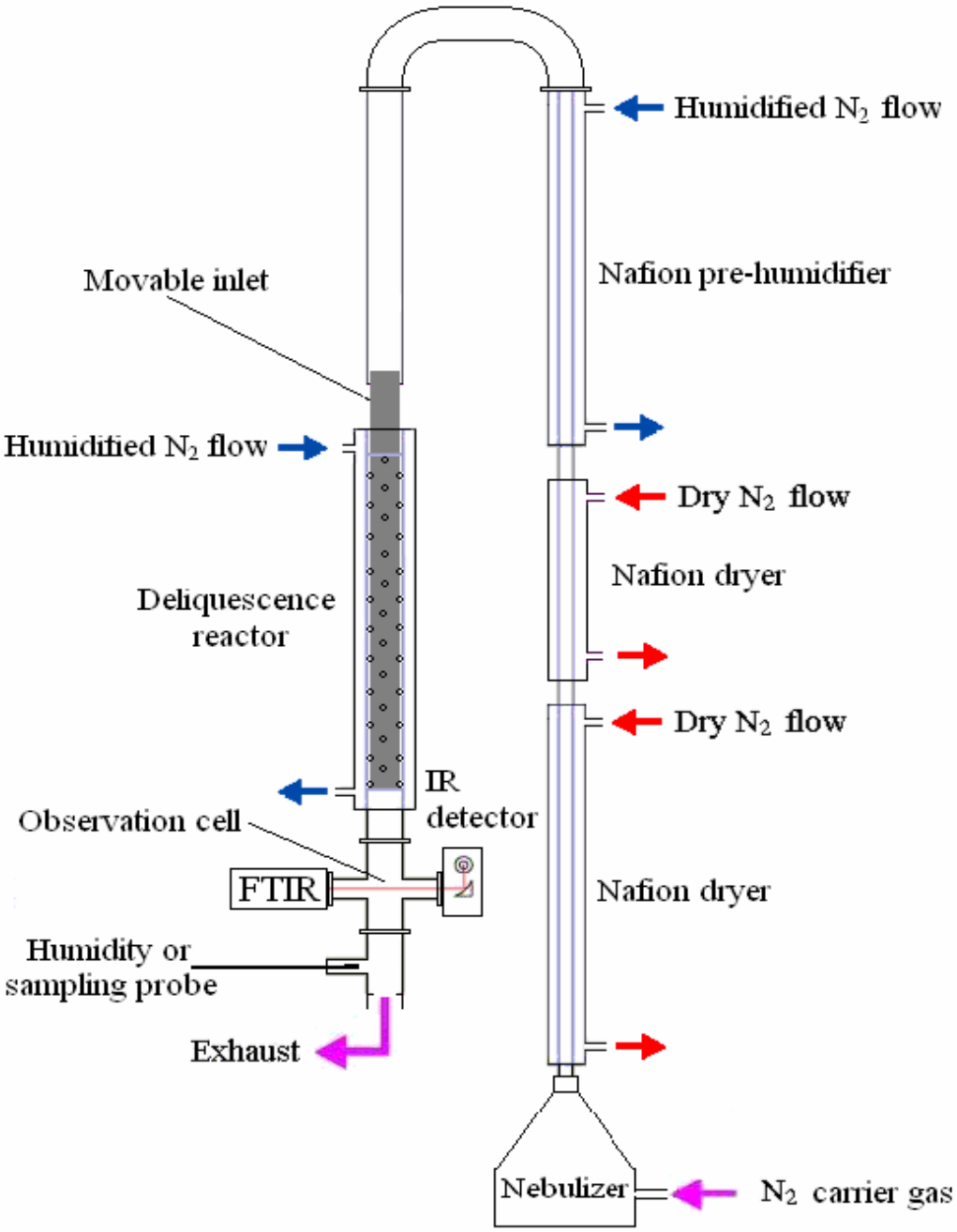

Figure 7.1: Schematic diagram of the room temperature glass flow tube used in the deliquescence of $(NH_4)_2SO_4$ experiments.

7.3 Results and discussion

A total of 57 aerosol spectra were recorded in the 75-81% RH range. Once the RH of each spectrum is determined by integrating the 1883 and 1897 cm^{-1} water vapor band, water vapor and CO_2 spectral features are removed from the raw spectra. A sample of the "clean" ammonium sulfate spectra obtained in this way is shown in Figure 7.2. The relative humidities, determined from the integration and the calibration curve, are compared to those acquired by the Vaisala humidity probe and the difference between the two methods, in this particular experiment, was assessed to be within ±0.5 % RH.

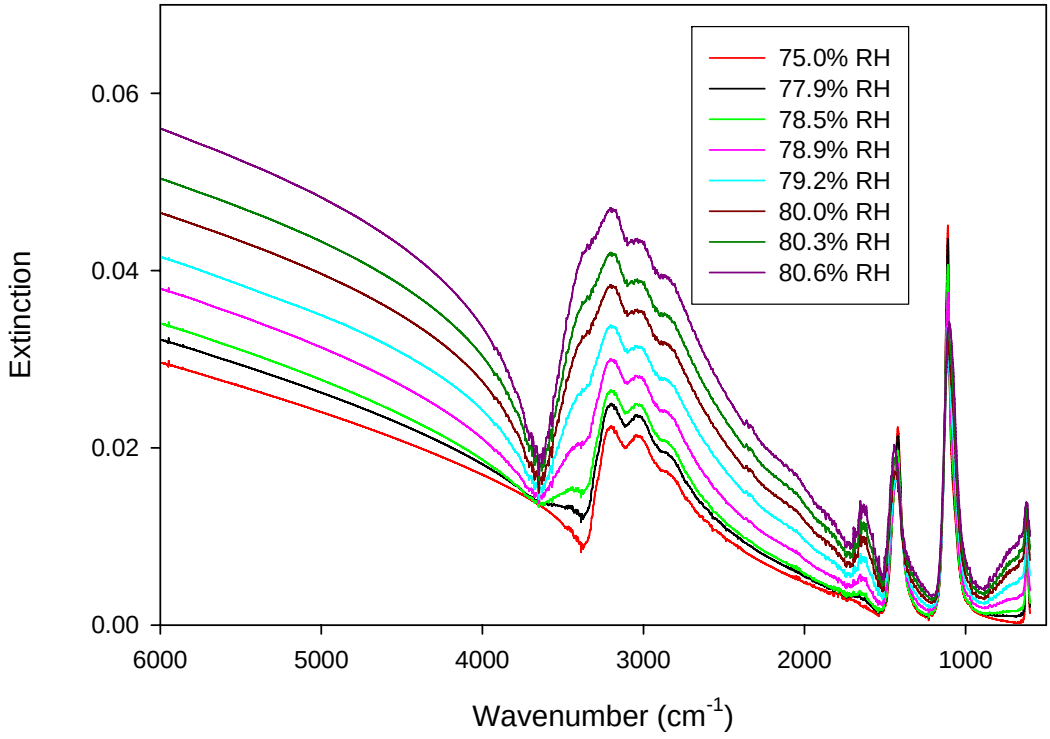

Figure 7.2: Examples of $(NH_4)_2SO_4$ spectra recorded during a deliquescence experiment.

As it can be seen in Figure 7.2, the evolution of the IR spectra and changes in the absorption features as a function of increasing RH are evident by simple visual inspection. Up to 78% RH, there are no changes in the shape and position of the absorption features with increasing RH. However, at approximately 78%, NH_4^+ and SO_4^{-2} peaks become wider and condensed water bands appear, as it can be seen from Figure 7.2. This point is considered the onset of water uptake by the aerosol particles, that is, the aerosol deliquescence. From this point on, the liquid water absorption features including 3450 cm^{-1} OH-stretch, 1640 cm^{-1} HOH-bend and 1640, 650 cm^{-1} H bond, become more prominent with increasing RH. As noted earlier, the spectra were recorded in the RH range 57.7-81.2%. At humidities higher than 80.6%, the losses of aerosols became evident, as witnessed by a sudden decrease in the amount of AMS detected in the spectra, and the increase in white AMS deposits on the inner-lower wall of the glass U-tube section. As it will be shown later at this point aerosols are fully deliquesced, their increasing mass and inertia leading to higher deposition rates.

A deliquescence curve, which describes the change of the liquid water uptake by aerosols as a function of RH, was generated using two different methods. In the first case, the liquid water content (LWC) was determined by integration of the 2300-3600 cm^{-1} liquid water band in IR spectra. Alternatively, the water content was determined from the volume distribution retrieved by the fitting procedure described in Section 2.2.1. Since during the deliquescence process AMS aerosol changes composition from solid particles (100% wt.) to saturated solution (≈40% wt.), the spectra were in this case fitted using the basis set(s) for solid and 40% wt. AMS solution, generated from our new optical constants (see Chapters 4 and 6). Samples of the fitted spectra and the corresponding distributions are shown in Figures 7.3 through 7.8. As can be seen, there is excellent agreement between the experimental and the calculated extinction spectra. The volume distribution plots clearly demonstrate the increase in the amount of 40% AMS at the expense of solid, with increasing RH. The corresponding LWC of the aerosol is subsequently determined by the integration of the 40% AMS volume distribution, given known density of the solution.

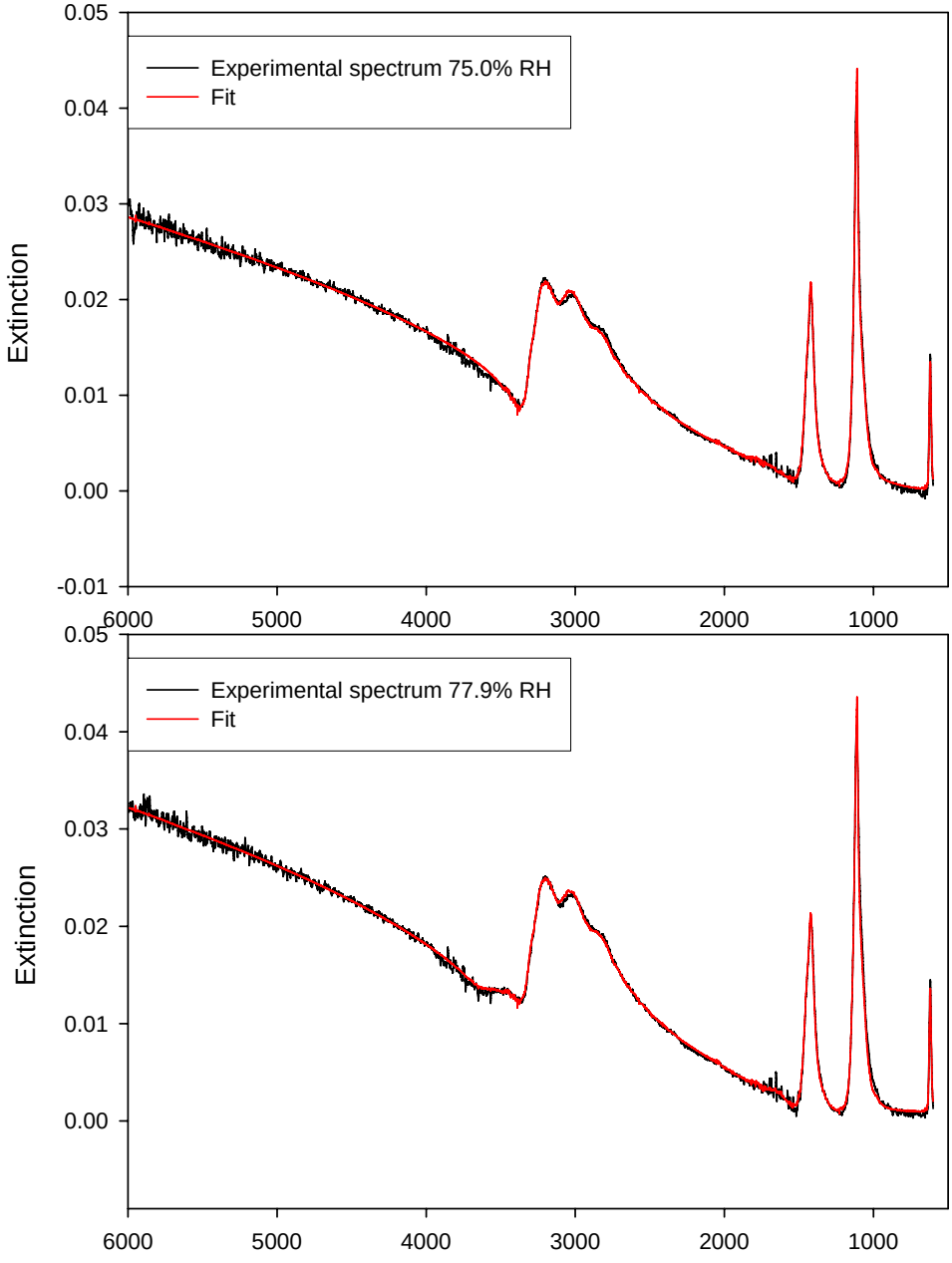

Figure 7.3: $(NH_4)_2SO_4$ experimental spectrum (black) and calculated extinction spectrum (red) of aerosol particles in an environment of 75.0% RH (top) and 77.9% RH (bottom).

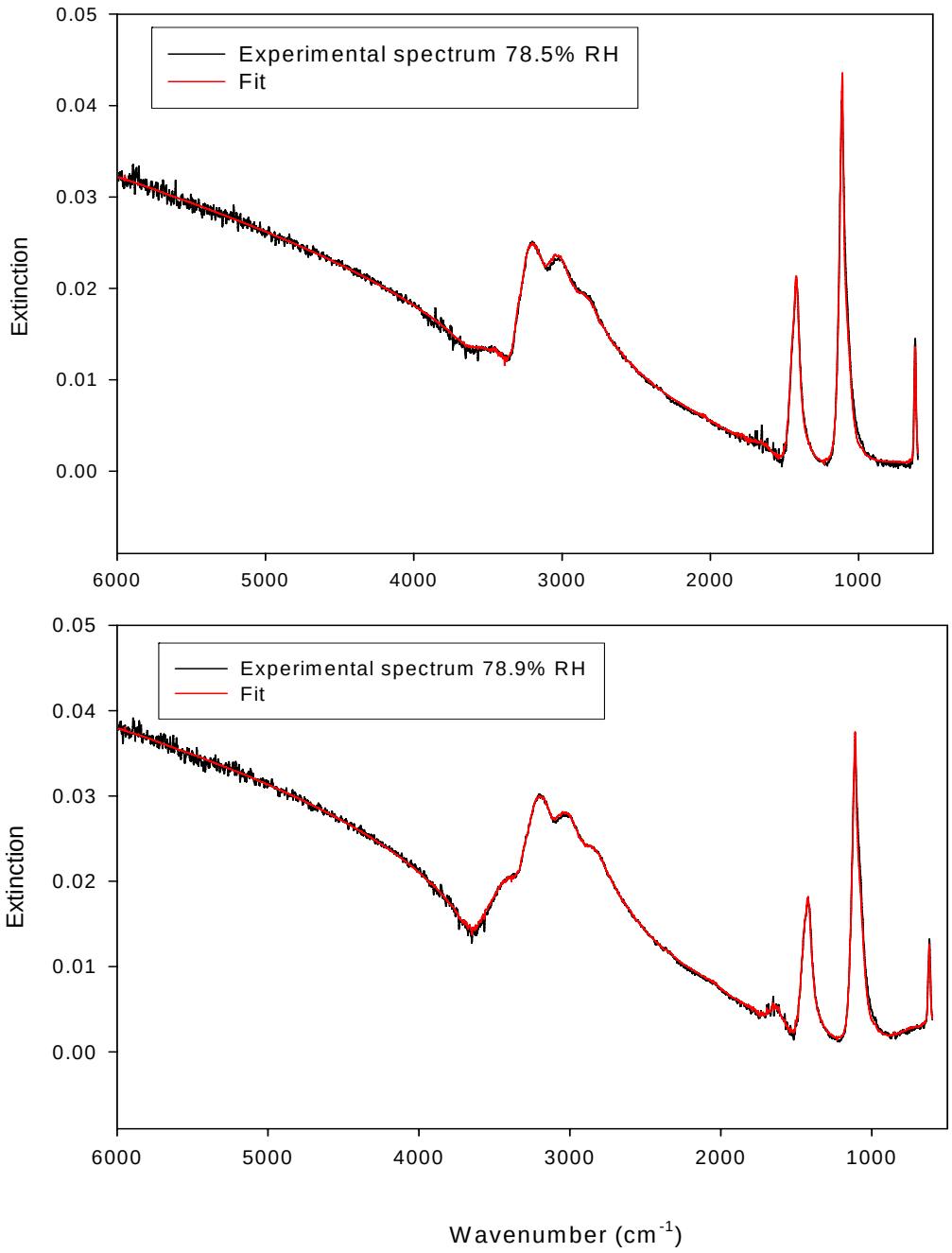

Figure 7.4: $(NH_4)_2SO_4$ experimental spectrum (black) and calculated extinction spectrum (red) of aerosol particles in an environment of 78.5% RH (top) and 78.9% RH (bottom).

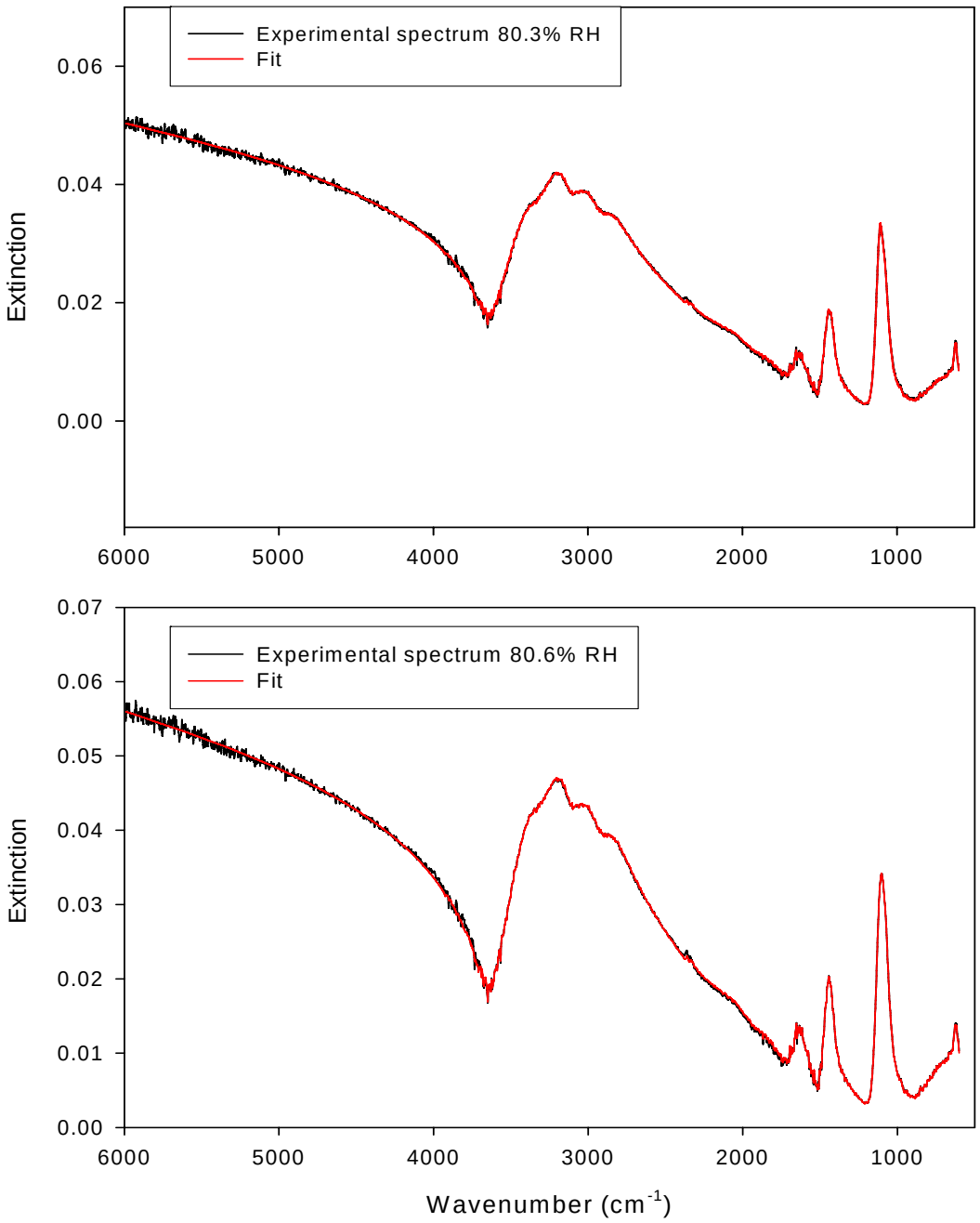

Figure 7.5: $(NH_4)_2SO_4$ experimental spectrum (black) and calculated extinction spectrum (red) of aerosol particles in an environment of 80.3%RH (top) and 80.6%RH (bottom).

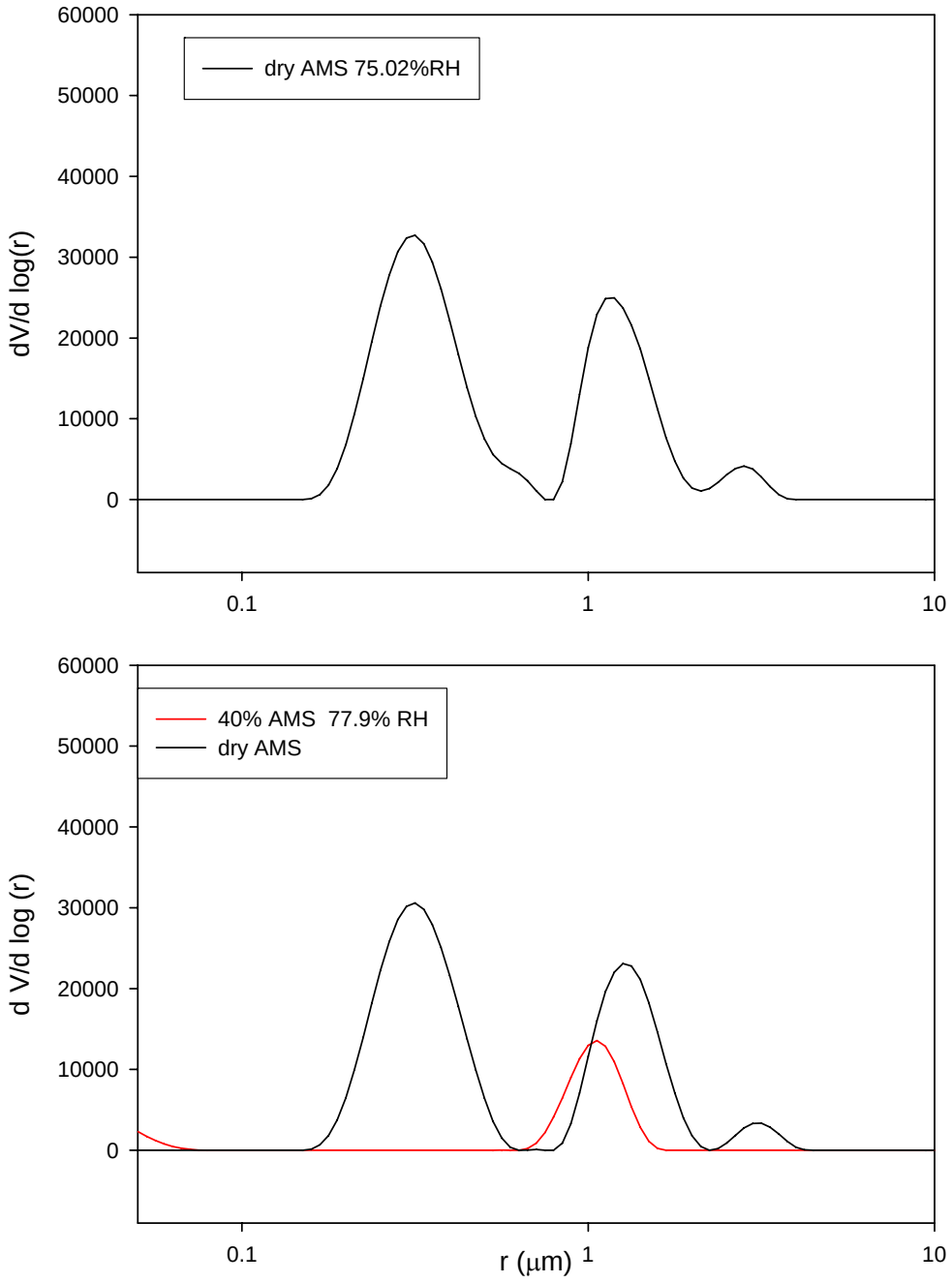

Figure 7.6: Volume distribution retrieved from an experimental IR $(NH_4)_2SO_4$ spectrum of 75.0% RH (top) and 77.9% RH (bottom).

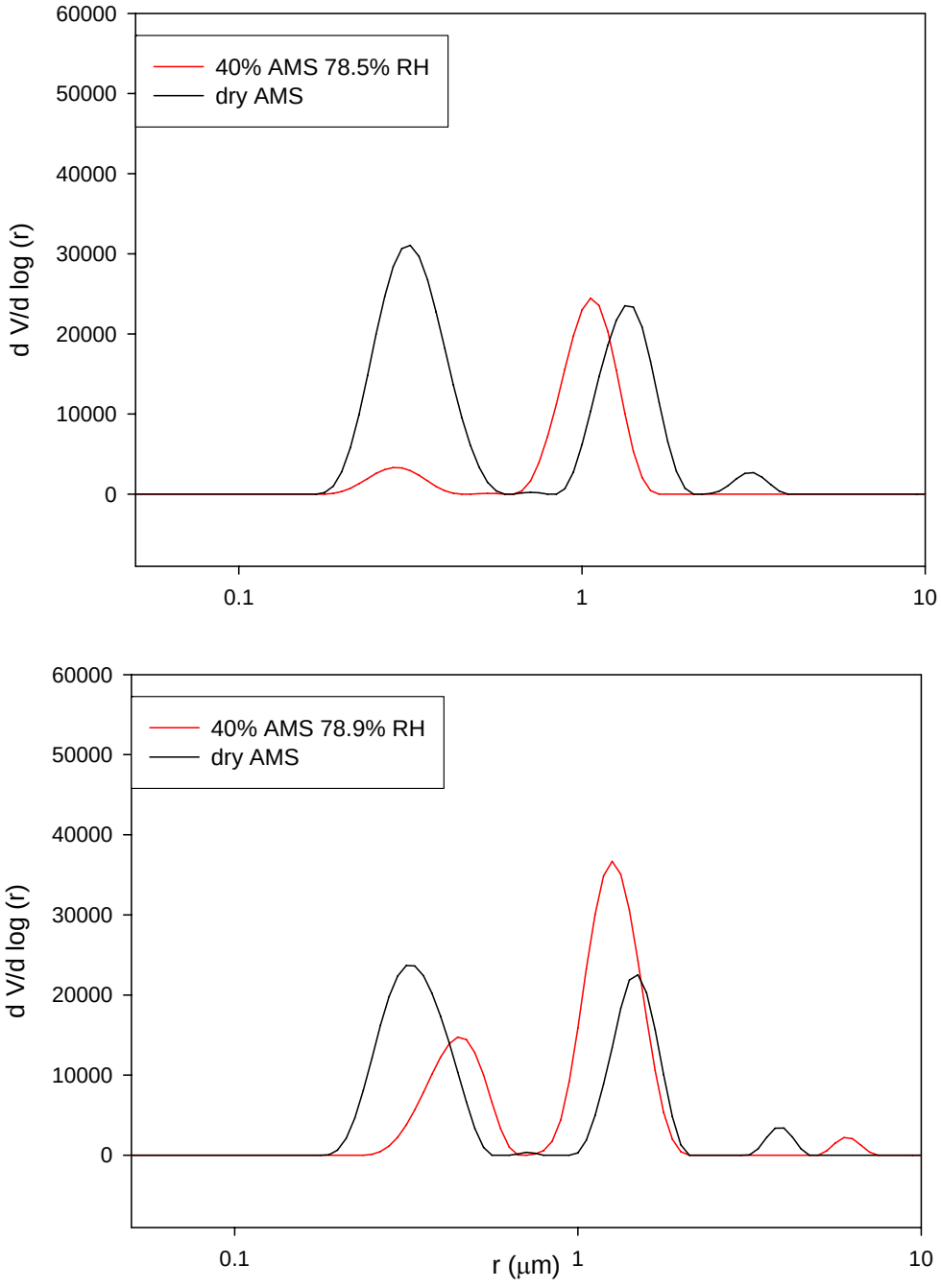

Figure 7.7: Volume distribution retrieved from an experimental IR $(NH_4)_2SO_4$ spectrum of 78.5% RH (top) and 78.9% RH (bottom).

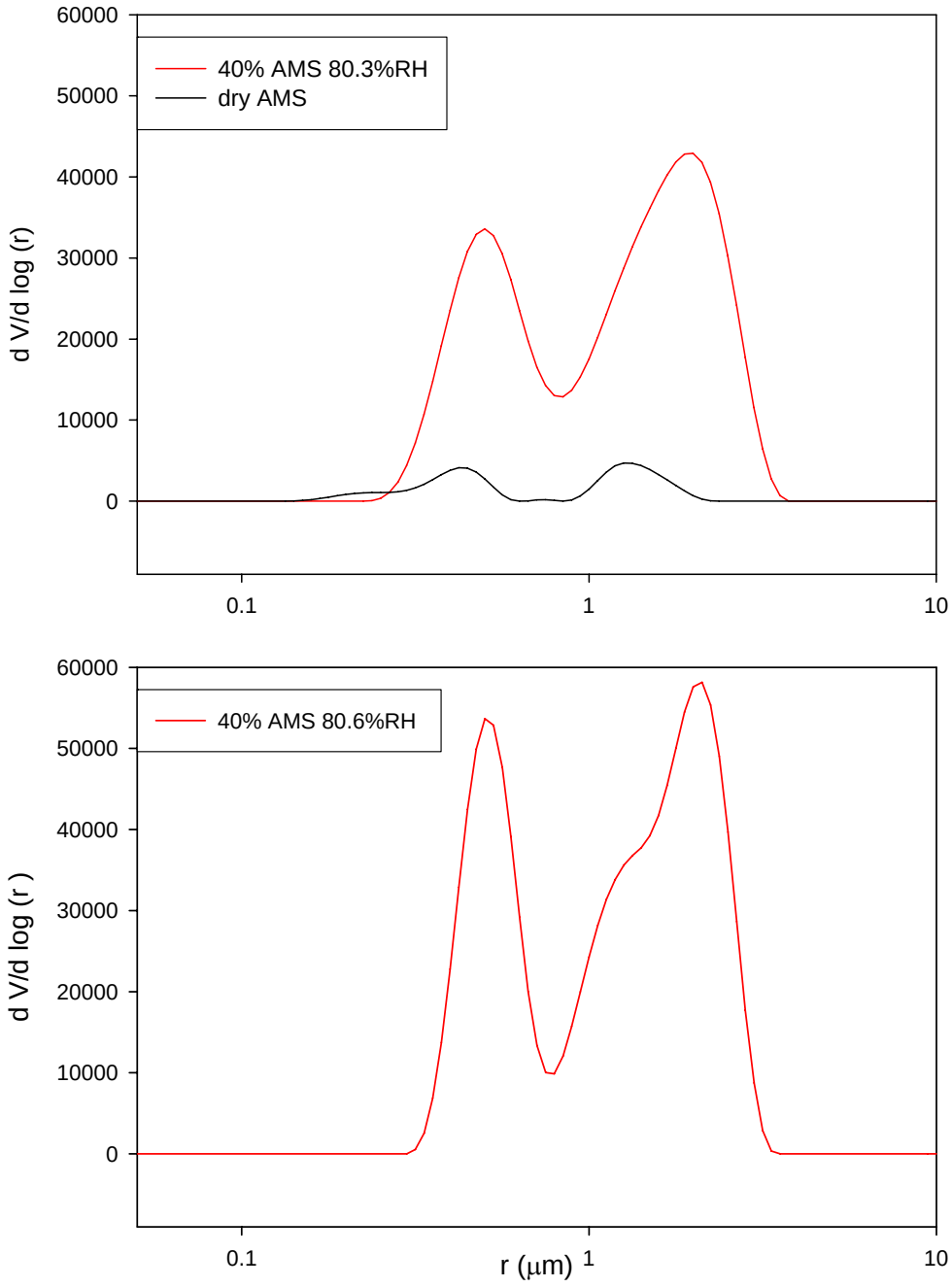

Figure 7.8: Volume distribution retrieved from an experimental IR $(NH_4)_2SO_4$ spectrum of 80.3% RH (top) and 80.6% RH (bottom).

It is apparent from the size distribution that particles within 0.45-1μm size range deliquesce first resulting in the 40% wt AMS solution mode seen in Figure 7.6 (bottom). Other modes corresponding to deliquesced particles appear later on, at higher RH. This observation might be related to the morphology of different size particles. As a result of the drying process, smaller particles could be tightly packed crystals, while bigger ones might be more irregular due to the presence of pores and water inclusions.

The deliquescence curves generated using the two methods are presented in Figure 7.9 In both cases, the RH values represented on the abscissa are those obtained from the RH calibration. As can be noted, the results obtained from the two methods are in very good agreement, demonstrating the applicability of our retrieval method in the determination of aerosol composition. As can be seen from the plots, the DRH range determined in our experiment is 79.6 %±0.85 which is, within experimental uncertainty, in a very good agreement with the previously reported values. This, again, demonstrates the capability of the experimental design and the reliability of methods used in this work.

As noted previously, the humidograms derived in this study indicate that the deliquescence process occurs within 3.3 % RH range. The onset of deliquescence was determined to be at 77.9 % RH, (which is at the lower end, relative to the other studies in which the onset was reported to be at 79±1%). Although this is still within the experimental uncertainty and accuracy limits of the instruments and methods used for the RH measurements, the early onset can be also due to the morphology of AMS aerosol particles. As discussed in Chapter 6, we performed the experiment to study the shape but not the morphology of AMS particles. Since AMS particles are formed by drying liquid droplets, it is possible that during the nucleation process liquid water be trapped (imbedded) in the concave pores even at humidities much lower than efflorescence RH.[20,72]As shown in the study by Colberg *et al.*, the shielding degree of the imbedded water is determinant in whether the water uptake begins below DRH.[72] When the liquid water in the pores comes in contact with the water vapor in the environment, it can trigger the deliquescence of particles at humidities (even) lower than DRH.

a)

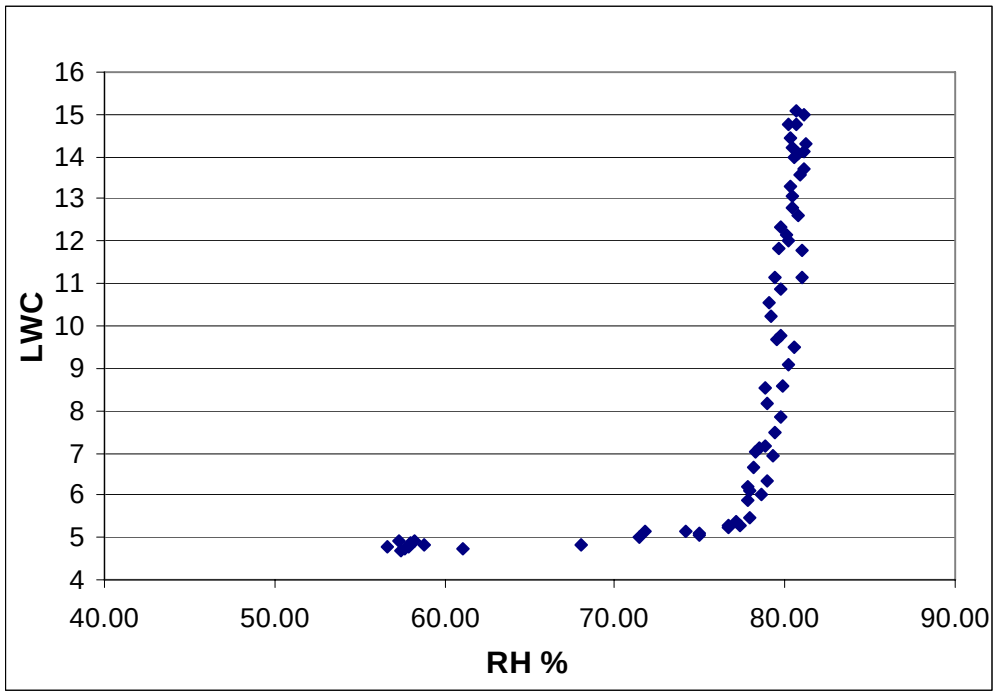

b)

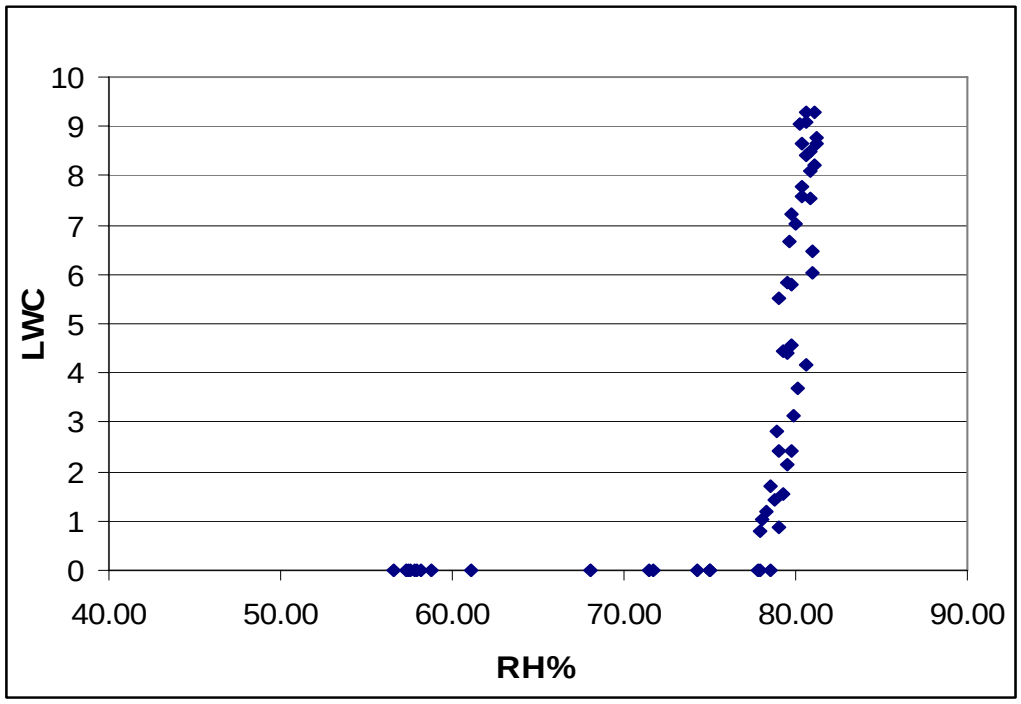

Figure 7.9: Deliquescence curve for AMS. Liquid water content: a) obtained from the integration of liquid water bands (2300-3600 cm^{-1}); b) obtained from the volume distribution; as a function of RH.

Chapter eight: Kinetics of deliquescence of ammonium sulfate

8.1 Introduction

While the thermodynamic aspect of the deliquescence process was studied extensively, both theoretically and experimentally, the kinetics of the process is still largely unknown. It is only in the past 15 years that new theories on the kinetics of deliquescence process have been introduced. One of them, proposed by Shchekin, Rusanov and Kuni, was developed in the framework of capillarity approximation using classical thermodynamics.[74-77] To avoid the use of surface tension for small particles, Ruckenstein and Nowakowski developed a theory that describes the kinetic process by determining the rate of absorption and emission of molecules (solute and water vapor) from the thin film of solution formed on a solid core.[78-81] This theory was applied to a monodisperse sample of (model) spherical aerosols with core material molecules that do not dissociate in water (in the thin film). The deliquescence curve (maximum external radius as a function of vapor saturation ratio) obtained using this approach shows a non-sharp transition of aerosols from a solid core surrounded by a thin liquid film to a saturated solution droplet.[82] This new theory was able to explain the non-sharp deliquescence observed experimentally in the case of NaCl and KCl aerosol particles.

While there has been a steady advance in the theoretical work done to describe and quantify the kinetics of deliquescence, the experimental kinetic measurements of it are still very scarce. The goal of this study is precisely to experimentally determine the kinetics of water uptake by aerosols, in particular, on ammonium sulfate particles. Studying the kinetics of any process, including deliquescence, requires that an appropriate kinetic model be adopted or developed, and an experimental design which will closely simulate the model's assumptions. The description of the kinetic model, the apparatus and the experimental design used in this work are given in the following sections.

8.2 Deliquescence Kinetic model

The deliquescence kinetic model used in this study is based on the calculation of the overall water uptake γ_{net} by the aerosol particles. The overall uptake is the end result of a series of processes that take place once the solid aerosol particle comes in contact with a humid environment. These processes include diffusion of water vapor to the aerosol surface, accommodation and evaporation at the interface, and diffusion of absorbed molecules into the bulk liquid. The overall effect of all these processes is best described by the resistance model.[83]The resistance model can be applied to solid aerosol particles that are coated with at least a monolayer of water molecules and can be expressed by:

$$\frac{1}{\gamma_{net}} = \frac{1}{\Gamma_g} + \frac{1}{\alpha} + \frac{1}{\Gamma_l} \qquad \textbf{(8-1)}$$

where $\frac{1}{\Gamma_g}$ is the resistance associated with the (diffusional) gas transport to the surface, α is the mass accommodation coefficient and $\frac{1}{\Gamma_l}$ is the resistance associated with the diffusion and solubility in the bulk liquid.

The first term, Γ_g, in eq. (8-1), calculated for the diffusion of gas molecules to a sphere of diameter *d*, accounts for the gradient in concentration of gas at the aerosol-gas interface and is given by:

$$\frac{1}{\Gamma_g} = \frac{\bar{c}\,d}{8D_g} \qquad \textbf{(8-2)}$$

where $\bar{c}$ is the mean molecular speed (in cm/s) and D_g is the diffusion coefficient of gas molecules to the aerosol particles (in cm^2/s). Since in our experiments water vapor molecules diffuse to aerosol particle surface in nitrogen (atmosphere), the D_g represents the diffusion coefficient of water vapor in nitrogen gas, which is at ambient conditions 0.22 cm^2/s.

The second term, α, describes the probability of a gas molecule colliding with the surface of the aerosol, to be absorbed by the liquid phase and it is defined as:

$$\alpha = \frac{no.of\ gas\ molecules\ absorbed\ by\ the\ liquid\ phase}{no.of\ molecules\ colliding\ with\ the\ surface}$$

The third resistance term in eq. (8-1), accounts for the solubility limited uptake, and under equilibrium conditions between the gas and the liquid phase can be expressed as:

$$\Gamma_l = \frac{4HRT}{\pi^{1/2}\bar{c}}\left(\frac{D_l}{t}\right)^{1/2} \qquad \textbf{(8-3)}$$

In the eq. (8-3) H is Henry's constant (mole liter^{-1}atm^{-1}), D_l is the liquid phase diffusion coefficient and t is the exposure time of the liquid to gas molecules (s). This uptake decreases in time and becomes zero when the rate of absorption equals the rate of evaporation of gas molecules in and from the liquid film surrounding the solid core of the aerosol particle.

As previously mentioned, we are interested in calculating the overall uptake γ_{net} by applying a kinetic model to the data obtained from the flow tube experiments. The kinetic model used in our calculations was based on the low–pressure reactor model developed previously by Remorov.[84] The model assumes that the flow tube design is such that low Reynold's numbers and a fully developed Poiseuille profile are achieved by the time the aerosol flow reaches the observation cell. In this case, the steady state mass transfer of gas molecules to the aerosol particles, in the cylindrical flow tube can be described by the following mass balance equation:

$$2\tilde{V}\left(1-\frac{r^2}{R^2}\right)\frac{\partial n_w}{\partial t} = D_g\left(\frac{\partial^2 n_w}{\partial r^2}+\frac{1}{r}\frac{\partial n_w}{\partial r}+\frac{\partial^2 n_w}{\partial z^2}\right)-kn_w \qquad \textbf{(8-4)}$$

$\tilde{V}$ - average flow velocity

D_g - diffusion coefficient of the gas

k - pseudo- first order rate constant for the uptake of water vapor molecules by the aerosol particles

r - radius of the aerosol flow

n_w - concentration of the water vapor

R -flow tube radius

t -contact time

The mass balance equation indicates that changes in the gas concentration profile in the flow tube are due to diffusion in the radial direction, given by the term $D_g\left(\frac{\partial^2 n_w}{\partial r}+\frac{1}{r}\frac{\partial n_w}{\partial r}\right)$, diffusion in axial direction, given by $D_g\frac{\partial^2 n_w}{\partial z^2}$, and the uptake of water vapor molecules by the aerosol particles, kn_w. This mass balance equation can be directly applied to our own flow tube - deliquescence reactor, the cross section of which is shown in Figure 8.1. In this case, eq. (8-4) is subjected to the following boundary conditions:

$$\left(n_w\right)_{r=R} = n_{H_2O(nafion\,wall)} \qquad \textbf{(8-5)}$$

and

$$\left(\frac{\partial n_w}{\partial r}\right)_{r=0} = 0 \qquad \textbf{(8-6)}$$

the first corresponding to the assumption that concentration of water vapor at the reactor walls is equal to that on the Nafion (membrane), and the second one describing a symmetrical profile of water vapor at the center of the aerosol flow.

As it can be seen from the schematics of the deliquescence reactor shown in Fig. 8.1, the model assumes that there are two distinct zones (in the reactor) relative to water vapor loss. In the central region of the reactor, in which relative humidity did not yet reach the deliquescence value, the rate of water vapor consumption by aerosol is zero. In the boundary layer itself, which is defined as the region in which RH is the same or higher than the DRH, the rate loss of water vapor, *k*, is finite and can be determined from Fuchs-Sutughin expression:[85]

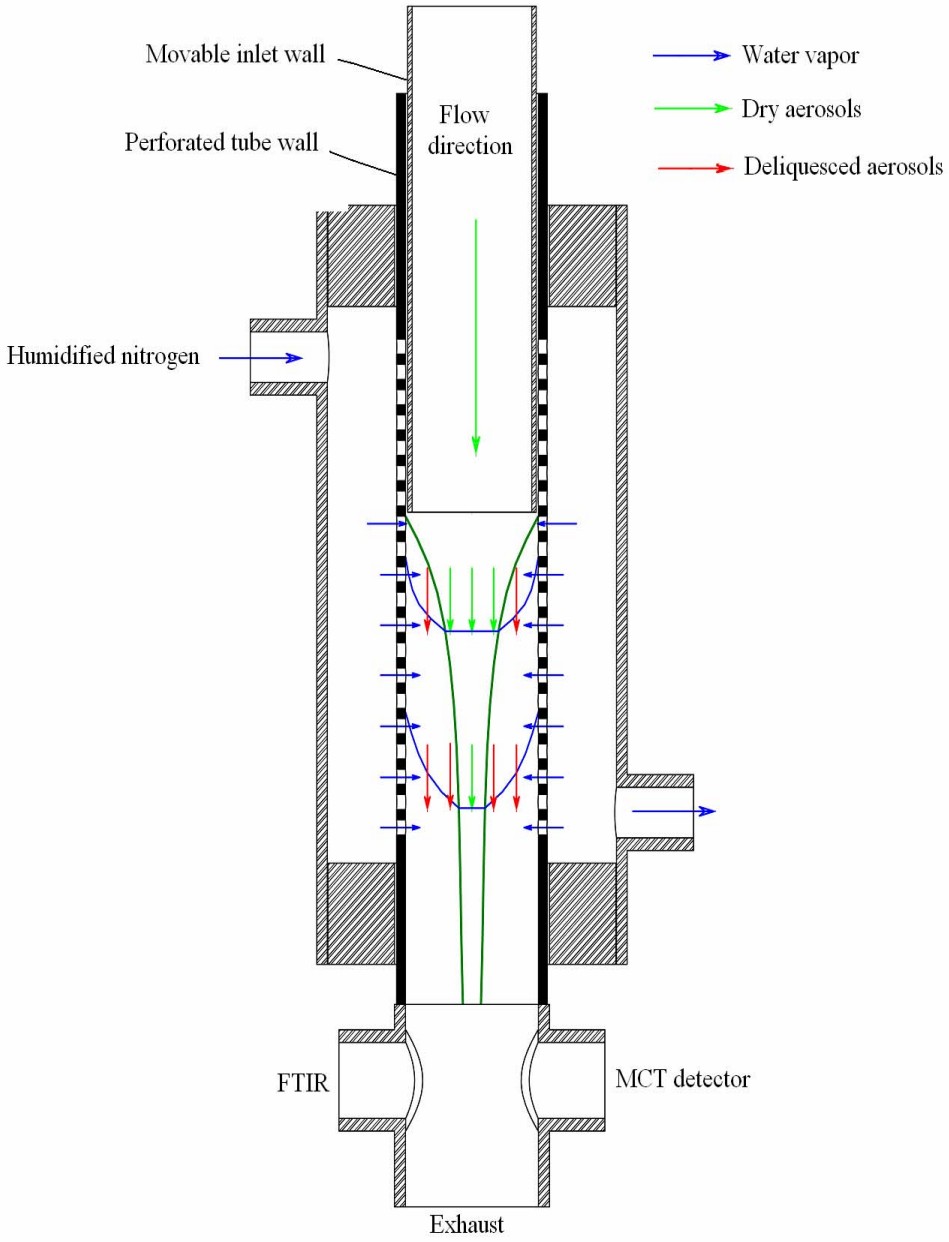

Figure 8.1: Schematic diagram of the (partially open) deliquescence reactor cross-section. The blue arrows show the water vapor profile at a certain position of the movable inlet. The green arrows show the aerosols flow laminar profile.

$$k = \sum_i \frac{\pi r_i^2 N_i \gamma_{net}(r_i, t)\bar{c}}{1 + \gamma_{net}\frac{0.75 + 0.283 \cdot K_n}{K_n(1 + K_n)}} \qquad \textbf{(8-7)}$$

In eq. (8-7) r_i is the aerosol radius, N_i the number density of the aerosol particles and K_n the Knudsen number, given by:

$$K_n = \frac{3D_g}{\bar{c}\, r_i} \qquad \textbf{(8-8)}$$

By treating the (loss) rate constant, k, in the mass balance equation this way, the net uptake γ_{net} can be calculated given that the contact time, the radius and the number density of the deliquesced aerosol particles are known.

As described in more detail in the experimental section, the experimental design and operating conditions were chosen in a way that further simplifies the model given by Eq. 8-4. For instance, the employed flow conditions allowed that the axial water vapor diffusion term be neglected. Further, application of the initial conditions for the differential equation was significantly simplified due to the fact that a uniform water concentration across the radius is achieved before the aerosol flow enters the reactor, and kept constant during the experiment. In addition, the model includes several important assumptions such as that the radial diffusion of the aerosol particles, their agglomeration due to collision and deposition on the walls are all negligible relative to their concentration.

The differential equation (8-4) is solved using a numerical procedure based on the finite difference method, with the partial derivatives $\partial n/\partial r$ and $\partial^2 n/\partial r^2$ determined using forward central difference approximation. Assuming some initial γ value in the range between 0 and 1, the procedure calculates the water vapor concentration profile across the tube and forward in (residence) time domain. The average concentration of water in the end of the reactor is determined from the radial concentration profile and this value compared with the experimentally measured concentration. The initial value of γ is changed and the calculation repeated until the measured and calculated concentrations agree within some pre-determined precision, in this case set to 1×10^{-3}. Since calculated concentration at the exit of the reactor is a monotonous function of γ, a simple bisection method was used to obtain the solution within the 0-1 γ range.

8.3 General Experimental

The (vertical) apparatus employed in the study of kinetics of deliquescence is identical to the one used in the deliquescence experiments, presented in Chapter 7, Figure 7.1. The aerosol flow generated by the nebulizer passes through the dryers, the pre-humidifier and the glass tube before it enters the deliquescence reactor. The purpose of the pre-humidification step was to bring the RH of the aerosol flow close to the DRH, for which we previously determined in the same apparatus to occur at 79.6%±0.85 (see Section 7.3). The humidity is typically brought to around 2 % of the DRH, value at which no or very few aerosols have already deliquesced (maximum of 0.1% by number). Such aerosols were then passed through the long glass tube, with the residence time long enough to allow the aerosol flow to reach equilibrium before entering the deliquescence reactor. For this type of experiments the aerosol flow rate is about 1 SLPM. The Reynold's number for this particular flow rate and tube diameter is 0.327, which would result in a fully developed laminar profile in 5.15×10^{-3} cm from the entrance of the aerosol flow in the glass tube.

As previously mentioned, the deliquescence reactor consists of a Nafion membrane wrapped around a perforated tube enclosed in a glass jacket and a sliding stainless steel inlet. A humid flow of nitrogen is flown through the jacket, under which conditions the reactor acts as a humidifier. The presence of the sliding inlet allows that contact times between the aerosol and water vapor be easily varied and the uptake coefficient measured at different stages of the deliquescence process (The design and the operational principle of the reactor were already explained in Chapter 3, Section 3.4.)

A cross-section of the deliquescence reactor, presented in Figure 8.1, shows the water vapor profile in the aerosol flow for a particular position of the sliding inlet. The aerosol flow has a fully developed laminar profile by the time it reaches the reactor's entrance. As previously mentioned we assume a negligible diffusion of the aerosols in the radial direction, therefore the profile of the flow is maintained throughout the reactor and into the observation plane. For the position of the movable inlet portrayed in Figure 8.1 the residence time of the aerosols, at (and close to) the center of the reactor, is shorter then the time required for water vapor flow to diffuse to the center, therefore only the aerosols near the wall are deliquesced as shown by Figure 8.1.

With increasing contact time, an increase in the thickness of the boundary layer leads to a higher number of deliquesced particles in the flow. In this particular example by the time the aerosols reach the observation point only a fraction of them is deliquesced, a dry core remaining in the center of the flow. Thus, what we observe at the observation plane is a mixture of crystalline particles and saturated ammonium sulfate solution droplets.

This evolution of the aerosol flow composition is visible in the IR spectra recorded at the observation plane (increase in the liquid water bands and broadening of the SO_4 peak) and subsequently in the composition and size distribution of the aerosol particles.

In general, the humidification system for the deliquescence reactor jacket is set a day ahead and the RH and temperature of it monitored overnight to assure that the system is in the steady state on the day of experiment. This step is necessary due to the high absorption capacity of the Nafion membrane for water and the long times it needs to equilibrate with the surrounding humid gas. Typically, we assume that the steady state is achieved when the RH of the gas at the exit of the jacket is stable for the past several hours and it is then safe to start the experiment. During this time the inlet is kept at closed position and the flow tube (inside) is purged with a flow of dry N_2. The jackets of the two dryers and the pre-humidifier were also continuously purged with dry nitrogen to ensure that the system is kept dry.

On the day of the experiment, the general procedure is the following. Once it is established that there are no leaks from the DR jacket side and the system inside is completely dry, a background IR spectrum is obtained with dry N_2 flowing through the system (including through the dryers and the pre-humidifier). The aerosols were then introduced in the system and the remaining N_2 flows (including dry flows through the two dryers and humid through the pre-humidifier) set to already pre determined values which bring aerosol flow close to the DRH. The system is monitored until it reaches steady state, by continuously recording the IR spectra of the aerosol flow and measuring the temperature and RH of the humid flow through the DR jacket.

We consider the steady state is achieved when there is no more change in the aerosol spectra and in the RH and temperature of the aerosol and humid N_2 flow through the jacket over 30 minutes .The typical time from the start up to the system reaching a steady state is around 1-2 hrs.

With the movable inlet still in closed position, the aerosol spectrum is continuously recorded and the RH and temperature of the flow through the jacket monitored over a period of 5-10 minutes. The inlet is then moved to the first, open position and the system is monitored until it becomes steady, which typically requires about 30 to 45 minutes. The equilibration time is the time required for the Nafion membrane and the humidified nitrogen in the reactor's jacket to reach a new steady state. Once the new steady state is reached, the aerosol spectrum and the RH of the humid flow in the jacket are again recorded over a similar period of time (5-10 min). This whole procedure of moving the inlet to the next position, waiting until the new steady state is reached, and recording the spectra and the RH, is repeated until the inlet is moved at the highest open position. This position does not necessarily correspond to a completely open reactor – it is rather a pre-determined position of the inlet for which it was found that only crystalline particles and saturated solution droplets were present in the aerosol flow at the reactor's exit. The inlet is then again returned to the completely closed position, and after reaching the steady state the spectra and the RH recorded and compared to the measurements from the beginning of the experiment. This step is to verify that there has been no change in the initial conditions in the course of the experiment, in terms of both the amount and composition of aerosols and the RH of the flow. Finally, the aerosol and the pre-humidified N_2 flows are disconnected and the system dried by introducing dry N_2 flow into the reactor and all the dryers and the pre-humidifier. With system completely dry and only N_2 gas flowing through, an IR spectrum is recorded again to verify that there has been no shift in the baseline since the beginning of the experiment.

The aerosol size, number distribution and composition at each inlet position are determined by applying the retrieval procedure (described in Section 2.2) to the IR extinction spectrum recorded at those conditions.

The amount of water vapor transferred from the reactor jacket to the aerosol flow at each inlet position is determined from the change of the RH of the flow at the exit of the jacket relative to its initial RH (with inlet closed).

As previously described in Section 3.8, this humidity was measured using the Vaisala humidity probe. These values are then compared with the estimates obtained from the composition of the aerosol flow (itself), where the total water vapor taken by the aerosol flow is the sum of the water used for the humidification of the carrier gas and the water taken up by aerosols.

Similarly, the water taken by the inner gas was determined from the change in its RH, relative to that at the closed inlet position (where the humidity is determined from the IR spectra using the calibration curve, see Section 3.8). The amount of water taken by the aerosol was calculated from the aerosol composition and volume distribution, as determined by the retrieval procedure. As it will be shown in the following sections, there is an excellent agreement in the water balance determined using these two methods.

All this information, including the aerosol number distribution, its composition, and the amount of water vapor transferred to the aerosol flow at each inlet position, were used as an input to the model to calculate the uptake coefficient based on the depletion rate of water vapor in the aerosol flow.

8.4 Kinetic model test study

To test the newly developed kinetic model - how well it simulates the water vapor concentration in the deliquescence reactor and predicts the final average concentration for given initial and boundary conditions – a simplified experiment was performed using only nitrogen gas. In this experiment, the N_2 flow was pre-humidified to the initial conditions comparable to those in an aerosol experiment and then gradually humidified in the deliquescence reactor, by varying the position of the movable inlet. The model was then used to simulate these conditions and these results were compared with experimental measurements. The set up and the results of this study are described in the following section.

8.4.1 Experimental

Dry N_2 flow (at 1 SLM) was introduced to the same experimental set up shown in Figure 3.7. To bring the dry flow to a humidity near DRH before it enters the deliquescence reactor, the operating conditions and the functionality of the Nafion dryers had to be somewhat modified. For this purpose the first Nafion dryer (100 cm long) was turned into a humidifier (by supplying jacket with 0.2 SLPM of humidified nitrogen), the second dryer was closed off (by closing the inlet/outlet of the jacket) and the pre-humidifier was supplied by 3.3 SLPM of humid nitrogen.

These conditions resulted in the nitrogen flow RH of around 76% with the deliquescence reactor inlet closed. Under those conditions, when there is no water vapor transfer in the reactor, the RH at the exit of the reactor's jacket is about 90.92%, with the humid N_2 flow rate of 5.2 SLPM. Once in a steady state, the spectra of the humid flow in the reactor are taken and the RH in the jacket recorded. The inlet is then moved (up) and the reactor open, initially by 1.3 cm. The system is monitored continuously and once the system reaches a new steady state the spectra and the RH are recorded again. Following this procedure, the inlet is moved to several different positions ranging from 1.3 to 35.2 cm and the conditions recorded for each state. As mentioned earlier, in the end of the experiment a spectra of dry gas are taken again to verify that there were no shifts in the baseline in the course of the experiment.

8.4.2. Results and discussion

The calculated average amount of water taken by the inner nitrogen flow and that given off by the humid nitrogen in the jacket for different contact distances, as well as the difference between the two are shown in Table 8.1. In this case, since there are no aerosols present, the water taken by the inner flow was just due to the increase in its relative humidity. In our calculations we used the difference between the two RH measurements to estimate the amount of water gained or lost by the gas. This approach led to the elimination from our results of the 0.5% error present in the measured RH.

Column four in Table 8.1 shows that there is an excellent agreement in the amount of water transfer estimated in the two ways, with error being mainly up to around 5%. The closed water balance suggests that no significant amount of water is absorbed or released by Nafion membrane, which we know has a large capacity for water which is a function of ambient relative humidity.

Table 8.1: Comparison of the mass balance of water transferred from the jacket to the deliquescence reactor at different contact distances.

Contact distance, cm	Average amount of H_2O vapor taken by N_2 flow in the reactor, g/min	Average amount H_2O vapor given away by humid N_2 in the jacket, $\boldsymbol{F_i}$, g/min	Difference in the amount of water transferred, as determined by the two methods, **%**
1.3	2.71×10^{-4}	2.80×10^{-4}	3.2
2.8	6.08×10^{-4}	6.11×10^{-4}	0.5
5.0	7.88×10^{-4}	8.06×10^{-4}	2.2
7.5	1.15×10^{-4}	1.07×10^{-4}	- 6.9
10.2	1.37×10^{-4}	1.31×10^{-4}	- 4.3
21.5	1.92×10^{-3}	1.94×10^{-3}	1.0
35.2	2.26×10^{-3}	2.18×10^{-3}	- 3.5

The calculated water vapor flow through the membrane can be used to estimate its flux through the wall, which may be used as a boundary condition by the model. The fluxes of water vapor at the wall, determined in two different ways, are shown in Table 8.1. Column three in the table shows average values of the flux through an entire segment for each contact distance, obtained from the total water vapor flow through the segment, F_i, (Table 8.1, Column 3) and the area of the segment, A_i,(Table 8.2, Column 2) as,

$$\Phi_{\text{entire segment}} = \frac{F_i}{A_i}. \qquad \textbf{(8-9)}$$

Table 8.2: Calculated average fluxes through the Nafion for entire segments and individual segment sections.

Contact distance, cm	Contact area, A_i, cm^2	Average water vapor flux through the entire segment, $\Phi_{entire\ segment}$, $g/cm^2\ min$	Area of the individual segments, $A_i - A_{i-1}$, cm^2	Average water vapor flux through individual segment section, $\Phi_{segment\ section}$, $g/cm^2\ min$
1.3	13.74	2.04×10^{-5}	13.74	2.04×10^{-5}
2.8	30.79	1.99×10^{-5}	17.05	1.32×10^{-5}
5.0	54.98	1.47×10^{-5}	24.19	1.25×10^{-5}
7.5	82.47	1.30×10^{-5}	27.49	9.60×10^{-6}
10.2	112.15	1.19×10^{-5}	29.68	8.76×10^{-6}
21.5	236.40	8.12×10^{-6}	124.25	4.75×10^{-6}
35.2	387.04	5.62×10^{-6}	150.64	1.73×10^{-6}

The last column in the Table 8.2 shows average fluxes for individual sections of a segment determined from the differences between the flows measured at successive inlet positions and their areas as

$$\Phi_{\text{segment section}} = \frac{F_i - F_{i-1}}{A_i - A_{i-1}} \qquad \textbf{(8-10)}$$

In order to use the fluxes determined this way as boundary conditions, they are fitted as a function of contact distance to eliminate the discrete nature of the data. As shown in Figure 8.2, the dependence is well represented by an exponential function, fitted in a way that the total area under the histogram (which is proportional to the total amount of water transferred per time unit) be preserved. As expected, in a co-current exchanger the flux is highest at initial contact times and decays rapidly, in order to level off at long enough contact times.

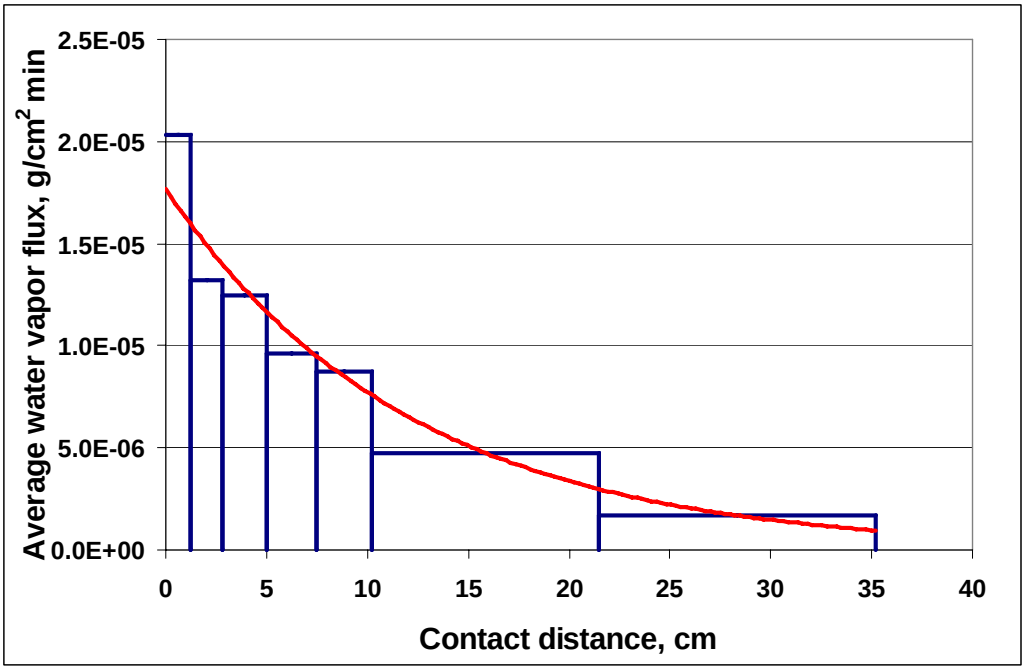

Figure 8.2: Fitted average water vapor flux for segments.

Using these two set of fluxes (averaged though an entire segment and the fitted flux) as boundary conditions and the RH in the system at closed inlet position as the initial condition, the average concentration of water vapor at the exit of the reactor was calculated for each contact distance. The results of the simulation are shown in Table 8.3 and in Figures 8.3 and 8.4. The relative errors between the experimental (Table 8.1, column 3) and calculated values for each flux profile are shown in Table 8.3. It can be seen that there is an excellent agreement between the simulated and experimental values, with errors mainly smaller than 0.5 % for either flux condition. That was rather expected, considering the closed mass balances for the water transferred in the system (see Table 8.1).

Table 8.3: Results obtained using average and fitted fluxes, to simulate water vapor concentration in the reactor.

Contact distance, cm	Contact time, s	$([H_2O]_{calc} - [H_2O]_{exp})/[H_2O]_{calc}$ using average flux, **%**	$([H_2O]_{calc} - [H_2O]_{exp})/[H_2O]_{calc}$ using fitted flux, **%**
1.3	0.72	0.41	-0.02
2.8	1.62	0.51	-0.38
5.0	2.88	0.29	0.12
7.5	4.33	0.01	0.05
10.2	5.89	0.12	-0.003
21.5	12.40	-0.23	-0.29
35.2	20.31	-0.20	-0.18

Figure 8.3 shows the simulation of water vapor concentration in the reactor for the longest (22.1 s) contact time, using average flux through the entire contact area. The red line shows the calculated average concentration in the reactor, the blue line - the calculated concentration at the wall, and the green point - the experimentally measured average concentration in the reactor. Although this model does a very good job in predicting the concentration at the exit of the reactor, it does not capture well the axial concentration profile of the flow, which is simulated as a linear function of contact time. This is clearly due to the fact that the average flux profile was used as boundary condition at the wall, which we know is not realistic in the case of concurrent transfer. This is even more apparent in Figure 8.4, which shows simulations of the concentration in the reactor for all contact times. In each case, it is evident that the end concentration was very well predicted (as also shown in table 8.3), although the realistic physical description of the reactor in between is lacking. However, as it can be also seen in Figure 8.4, when the data are observed as a collection rather then individually, they provide valuable information on the actual state in the reactor. The simulated end concentrations plotted as a function of contact distance give a more realistic picture of the axial concentration profile in the reactor.

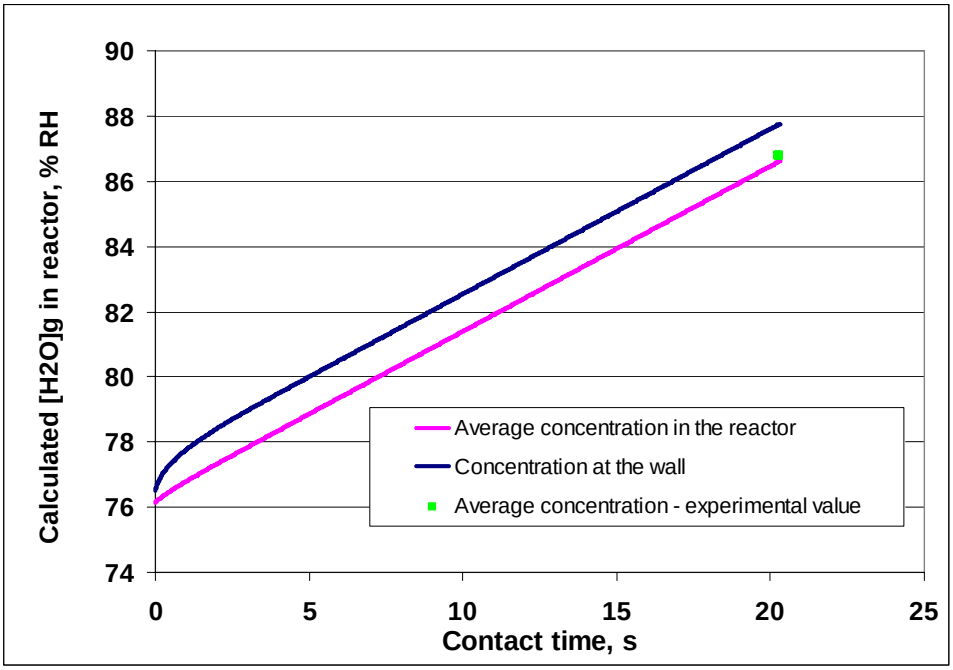

Figure 8.3: Simulation of water vapor concentration in the deliquescence reactor. The average flux through the entire contact area was used in calculating the concentration of water.

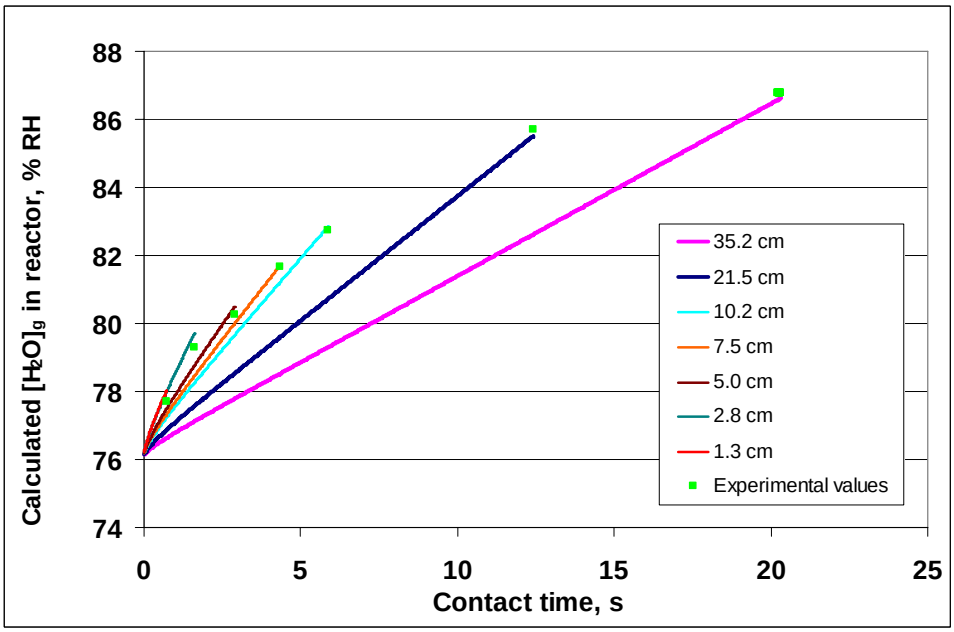

Figure 8.4: Simulated average water vapor concentrations in the reactor and at the wall and the experimental recorded values, for seven different contact times. The average flux through the entire contact area was used in calculating the concentration of water

Figure 8.5 shows the water vapor concentration in the reactor, simulated using the fitted flux profile obtained from segmented sections (see Fig. 8.2). The same flux profile was used to calculate concentrations for all contact times, so the single red line in Figure 8.5 represents the simulated average concentration profile for all cases. Again, the blue line shows the retrieved wall concentration and the green points - the experimental measurements. The benefit of using the fitted flux profile is obvious, since it not only well simulates the end concentrations, but also the concentration history in the reactor. As expected for the set up in our case, due to high fluxes at early contact times there is a sharp increase in the concentration profile initially, which gradually subsides with contact time.

Due to the apparent advantage of dealing with the fitted flux profile, similar approach will be used in the deliquescence kinetic experiment. Although the flux profile will not be used directly as a boundary condition, experiments like these will be employed to obtain wall concentrations under conditions similar to those in kinetic experiments, and those wall concentrations subsequently used as boundary conditions (b.c.).

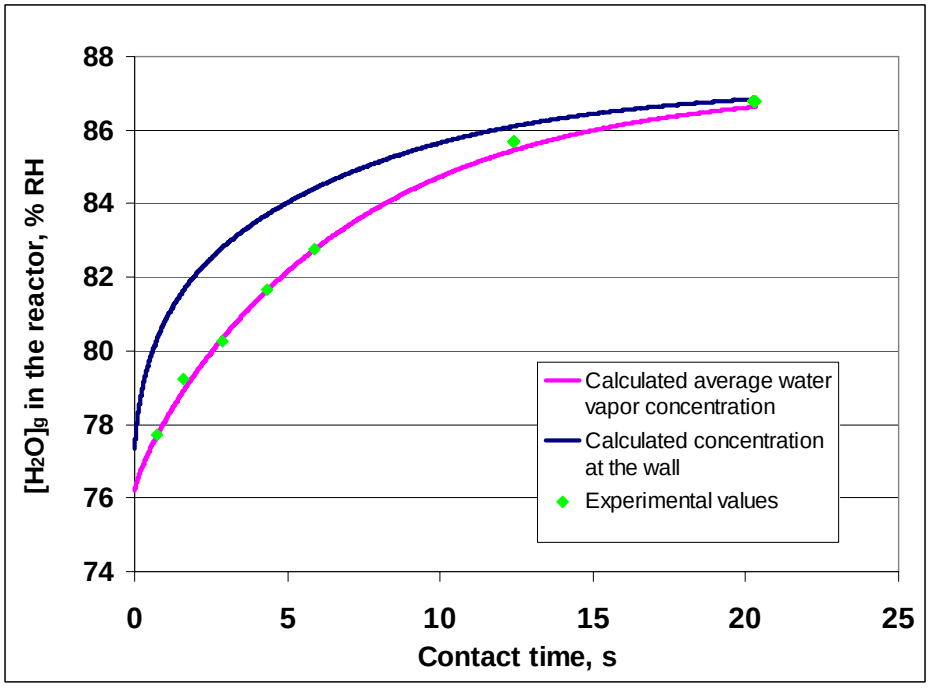

Figure 8.5: Flux profile in the reactor and at the wall, obtained by fitting calculated fluxes for each segment.

8.5 Aerosol experiment

8.5.1 Experimental

In the deliquescence kinetics experiments the aerosols were produced by nebulizing a 2 M solution ammonium sulfate (Mira Mist Nebulizer was used for this purpose). The flow rate of the generated aerosol was 0.92 l/min, obtained by operating the nebulizer at 45 PSI backing pressure. The aerosol droplets were dried by passing the aerosol thorough a series of two Nafion dryers, in order to bring its humidity down to the level below the efflorescence point (RH<35%).

To achieve this level of drying, dryer I (100 cm long) and II (50 cm long) were supplied by dry nitrogen flows at the rates of 1.5 and 0.8 l/min, respectively. This set up resulted in the aerosol flow RH at the exit of the drying system at about 27-30 %

Dry aerosol flow was subsequently passed through the Nafion-based pre-humidifier, in which its RH was raised to 77.5%. For that purpose, the jacket of the pre-humidifier was supplied with 3 l/min humid nitrogen gas (at around 93 % RH), produced using the bubblers system. As described in detail in Section 8.3, once the system reached a steady state, the spectra of the aerosols were recorded, as well as the RH and temperature of the humid flow in the reactor jacket. Such measurements were taken at seven different inlet positions including at 0 cm (inlet closed), 1.3, 2.5, 5.0, 7.5, 21.5, and 35.2 cm open inlet position. As always, all measurements were taken at steady state.

8.5.2 Results and discussions

The seven IR extinction spectra of AMS aerosols, corresponding to different inlet positions, are shown in Figure 8.6. These spectra were obtained after CO_2 and H_2O vapor subtraction. Due to the changes in the composition with increasing RH, the spectra exhibit familiar change in the shape and the position of the AMS and liquid water features, as discussed in detail in Section 7.3.

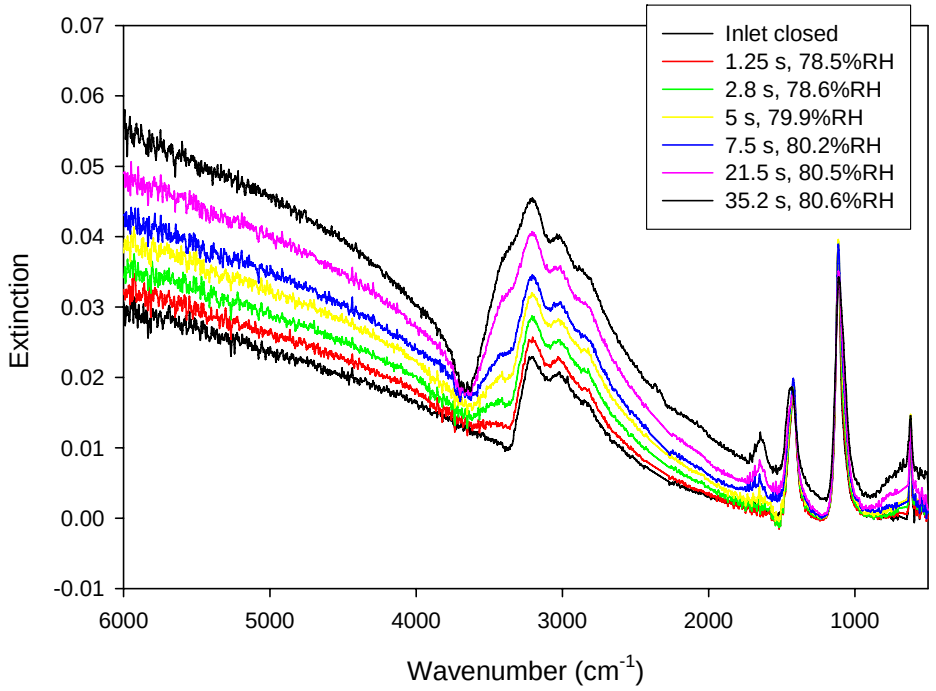

Figure 8.6: Examples of $(NH_4)_2SO_4$ spectra recorded during a deliquescence experiment.

To quantify the change in the aerosol composition and their number density with contact distance, the spectra are fitted by applying the iterative procedure. The composition of the spectra was initially analyzed using optical constants for crystalline AMS, 40% wt. (saturated) solution, 35 % and 30 % wt. solutions. The retrieved distributions indicated the presence of only solid and saturated AMS solution in the system, even at the highest humidification levels. Therefore, in further analysis of the spectra, only these two components were considered. The retrieved volume distributions, corresponding to each of the spectrum in Figure 8.6, are shown in Figures 8.7 through 8.10. As reflected by the distribution obtained at the zero contact time, Figure 8.7(a.), for practical purposes aerosols are all in crystalline phase, with liquid phase accounting for only 0.1%-0.05% aerosols (by number). The picture starts to change with increasing contact times and RHs. At longer contact distances, more water is exchanged between the jacket and the aerosol flow, and there is more time available for water vapor molecules to diffuse further into the reactor. The direct consequence of this is that more crystalline AMS particles are converted into saturated solution by taking up the water from the environment. This gradual increase in the content of liquid water in the aerosol is well illustrated in Figures 8.7 through 8.10.

a)

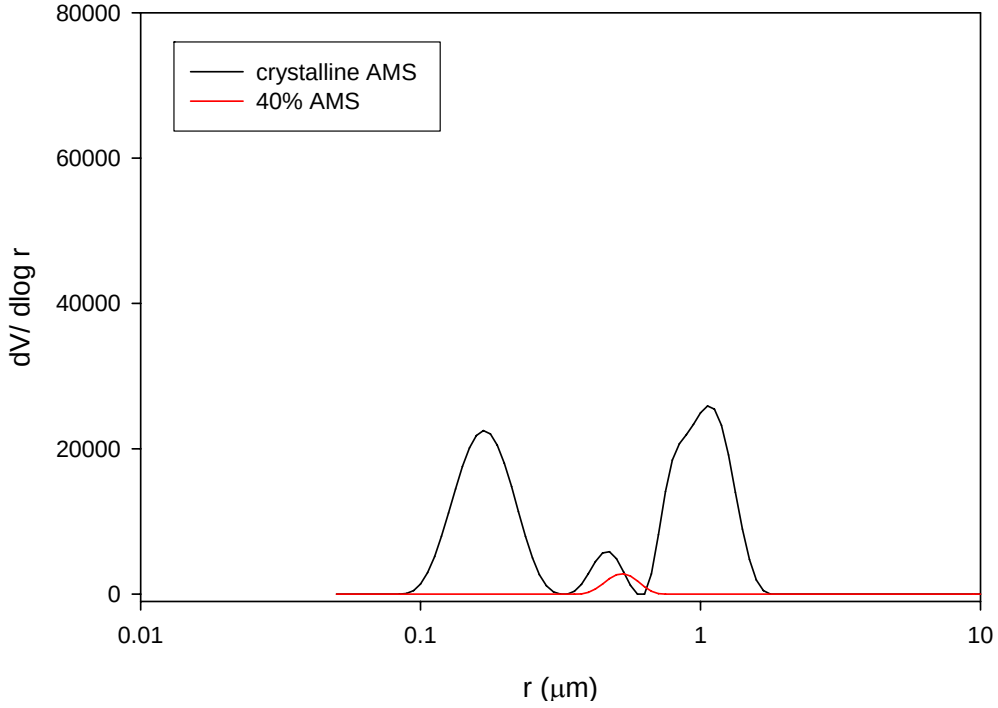

b)

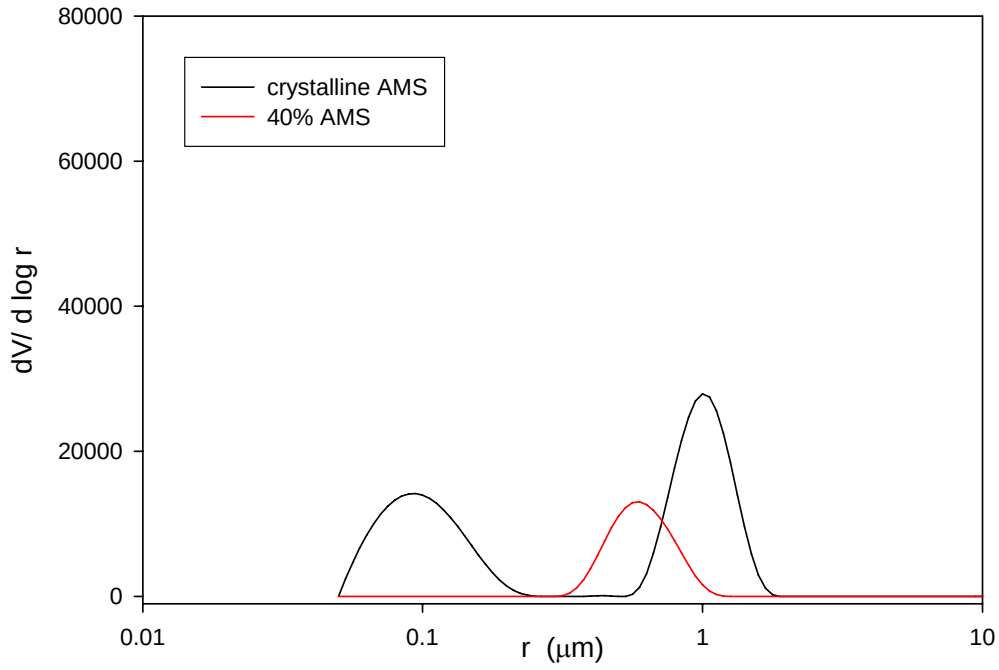

Figure 8.7: Volume distribution retrieved from an experimental IR $(NH_4)_2SO_4$ spectrum of 77.6% RH (a) and 78.5% RH (b).

a)

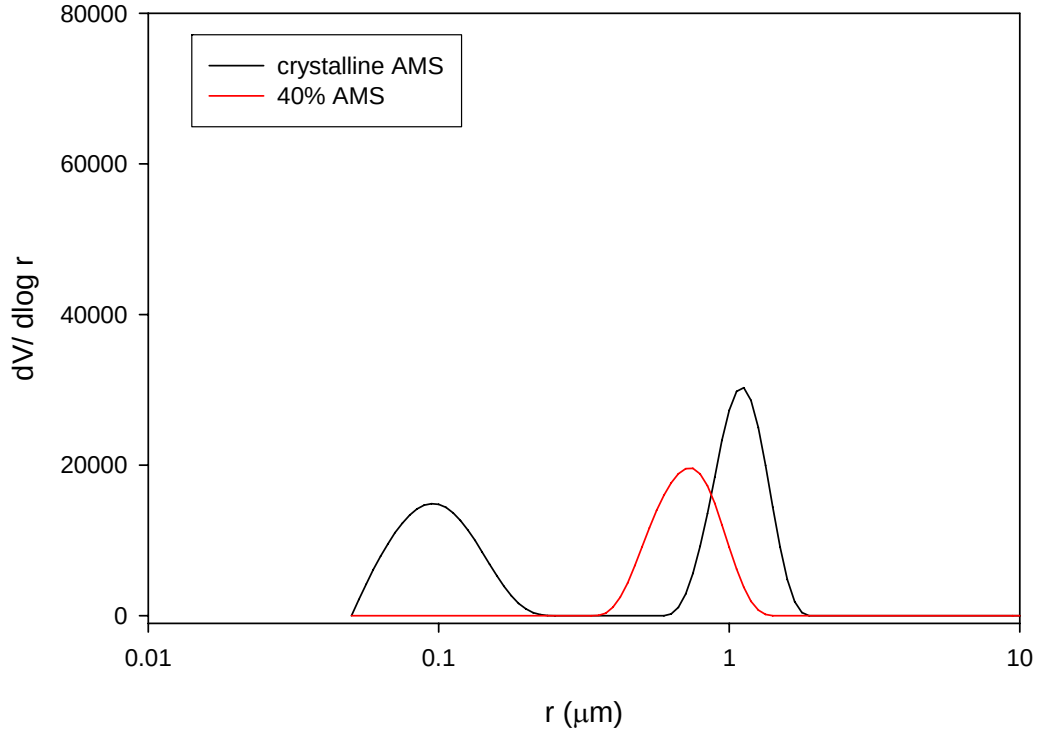

b)

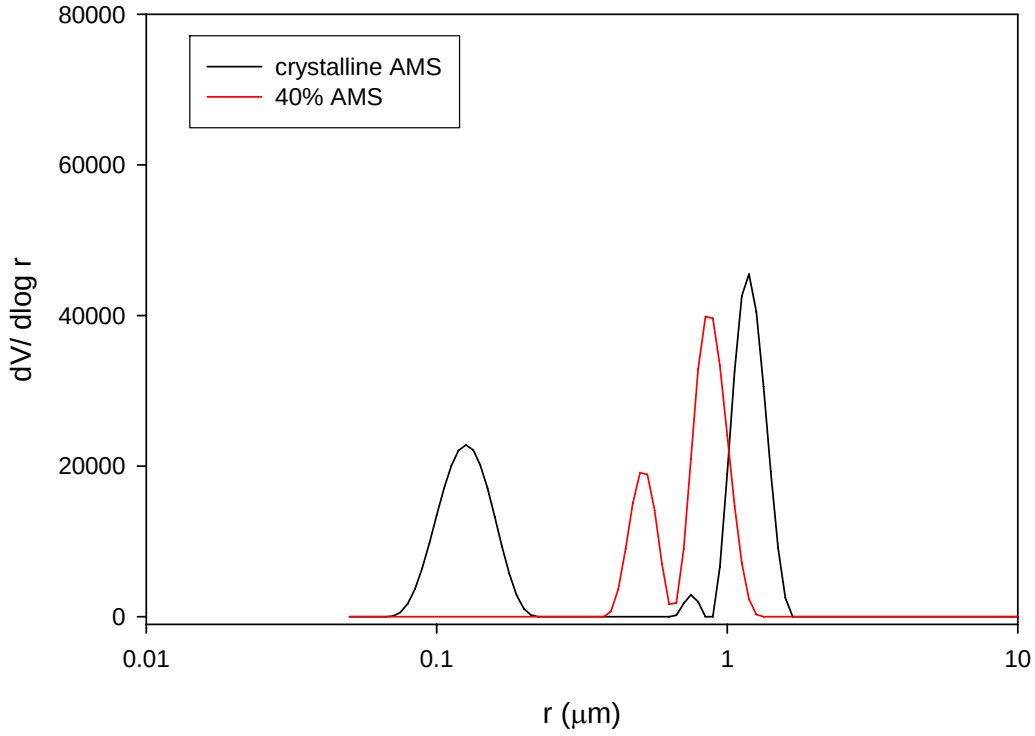

Figure 8.8: Volume distribution retrieved from an experimental IR $(NH_4)_2SO_4$ spectrum of 78.6% RH (a) and 79.9% RH (b).

a)

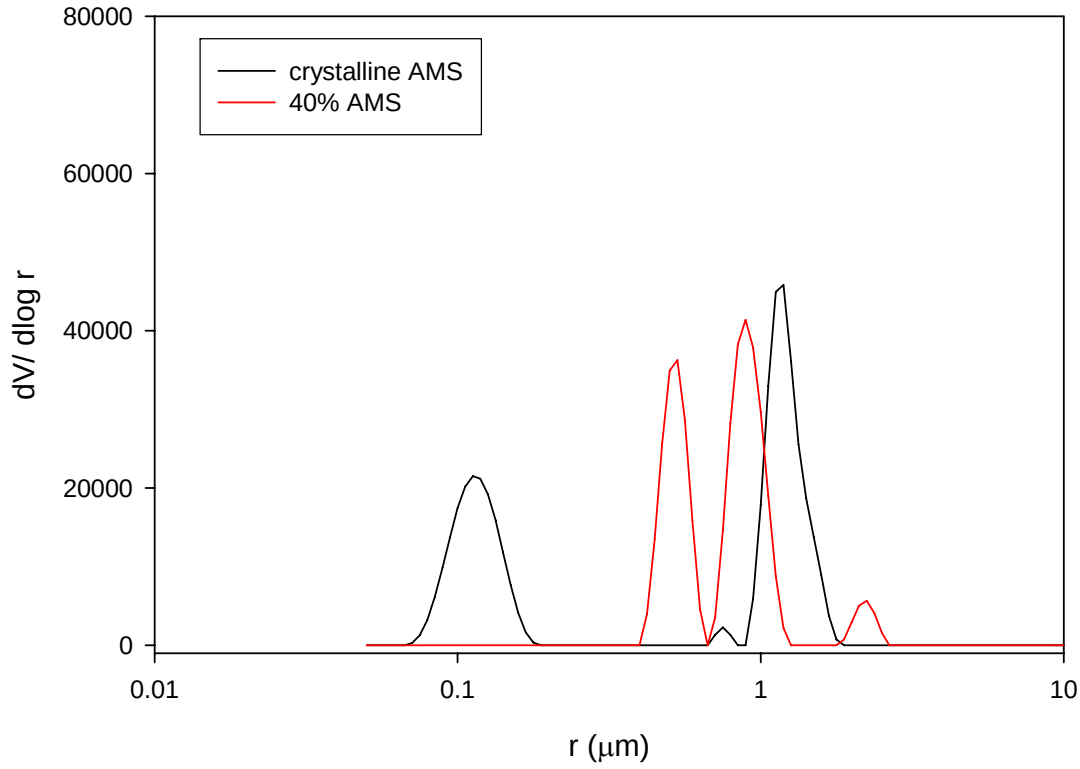

b)

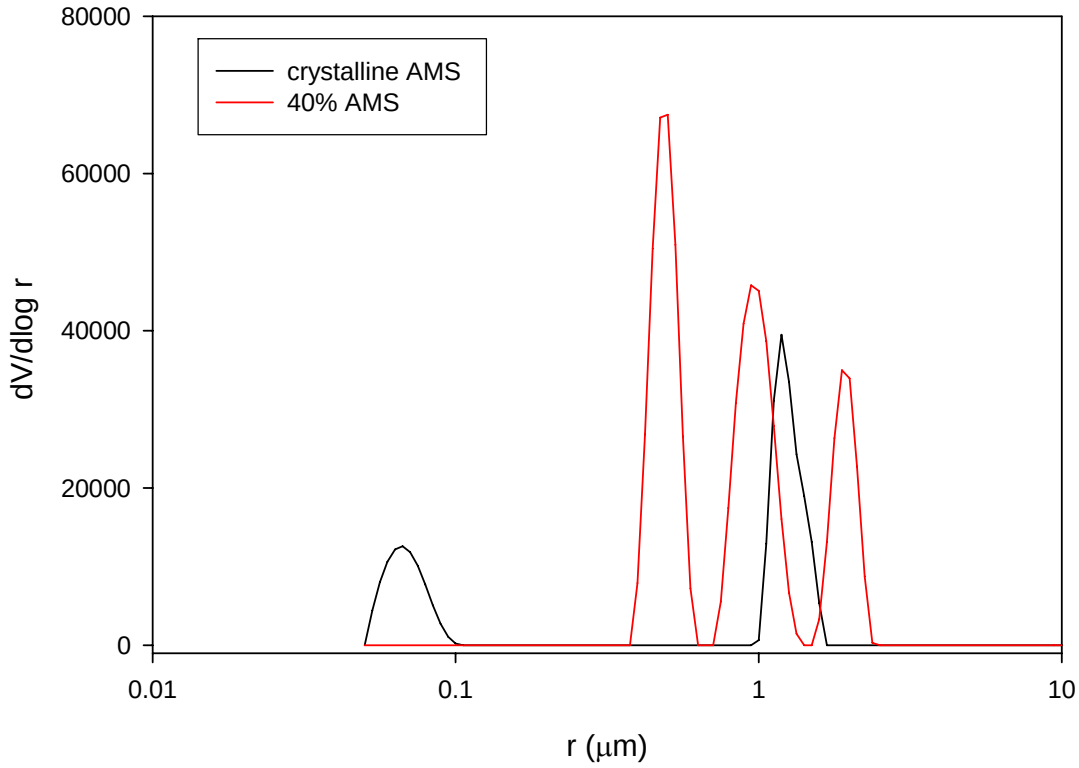

Figure 8.9: Volume distribution retrieved from an experimental IR $(NH_4)_2SO_4$ spectrum of 80.2% RH (a) and 80.5% RH (b).

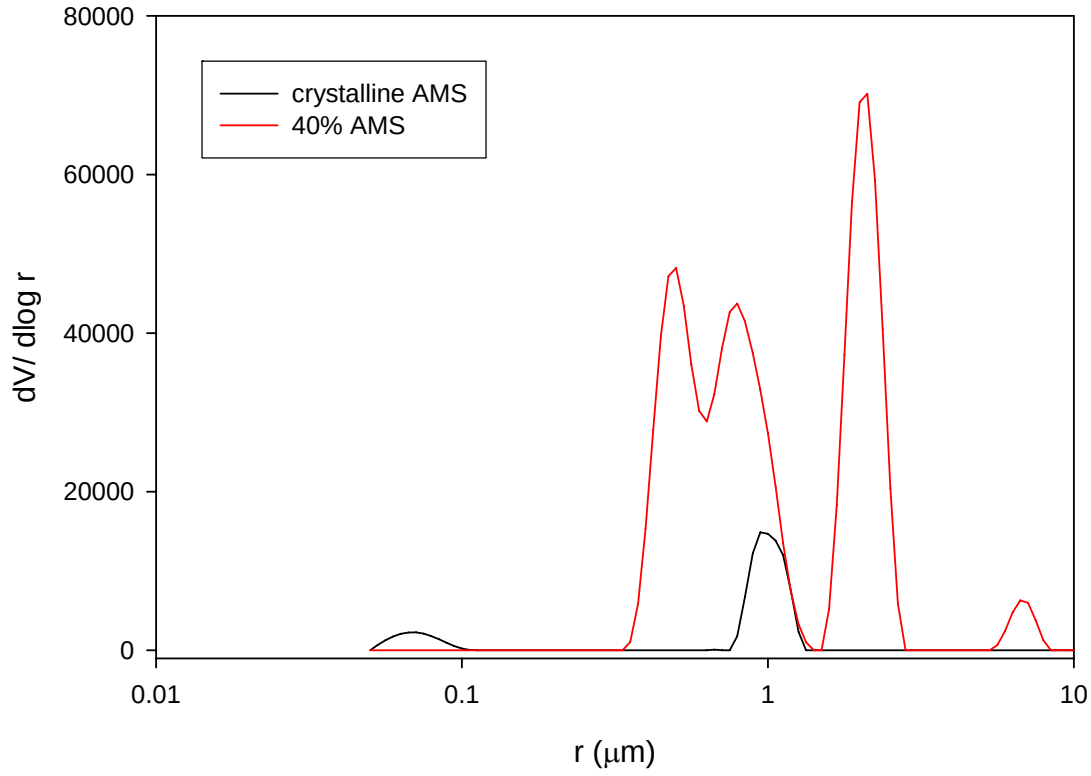

Figure 8.10: Volume distribution retrieved from an experimental IR $(NH_4)_2SO_4$ spectrum of 80.6% RH.

Table 8.4 summarizes the composition of the aerosol flow retrieved at different contact times, including the amount of AMS and liquid water in aerosols, and the amount of water vapor in the carrier gas. The amount of AMS and liquid water in the aerosol particles were obtained from the spectra, in particular, the distributions shown in Figures 8.7-8.10. The amount of water taken by the carrier gas (Table 8.4, column 3) was determined from the IR spectra using the calibration curve.

Table 8.4: Summary of the experimental conditions, the amount of AMS and water in aerosols and the amount of water in the carrier gas.

Contact distance, cm	Contact time, s	RH of the flow at the observation plane, %	Total mass of AMS, μg/cm3	Water taken up by aerosol, μg/cm3	H_2O taken by N_2 gas in deliquescence reactor, g/min
Inlet closed	0.0	77.5	0.960	0.00	0.00
1.3	0.78	78.6	0.960	0.059	2.10×10^{-4}
2.8	1.76	78.7	0.971	0.129	2.16×10^{-4}
5.0	3.14	79.9	0.982	0.137	4.48×10^{-4}
7.5	4.70	80.2	0.975	0.264	4.98×10^{-4}
21.5	13.5	80.5	0.929	0.522	5.59×10^{-4}
35.2	22.8	80.6	0.911	0.693	5.63×10^{-4}

As seen in the fourth column, the consistency in the amount of AMS through out the experiment is satisfactory. This suggests that there are no significant losses of the material in the system (or at least that its loss rate is constant) like, for instance, in the case of the deposition of aerosols at the walls. As expected, there is a steady increase in the amount of water taken up by aerosols (column 5) with contact time, the amount being comparable to the water taken by the carrier gas for the longest residence time.

The mass balance of the water transferred to the aerosol flow is shown in Table 8.5. In the case when aerosols are present, the total amount of water taken by the aerosol flow, shown here in column 2, is due to the water taken up by aerosol and the carrier gas, shown in Table 8.4, columns 5 and 6, respectively. These values are compared to the amount of water given away by the humid flow in the jacket and are shown in column 3 (Table 8.5). As it can be seen, there is a good agreement in the amount of water determined by these two methods, with the difference in most cases less than 10%, and maximum of 16% in the case of one measurement.

Table 8.5: Comparison of water amount transferred from the jacket to aerosol flow (at different contact lengths), determined using two different methods.

Contact distance, cm	Total H_2O taken by aerosol flow in deliquescence reactor, g/min	H_2O given away from the flow in the jacket, g/min	Difference in the H_2O balance determined by the two methods, %
Inlet closed	0.00	0.00	/
1.3	2.64×10^{-4}	2.83×10^{-4}	6.7
2.8	3.35×10^{-4}	3.99×10^{-4}	16.0
5.0	5.74×10^{-4}	5.77×10^{-4}	0.52
7.5	7.43×10^{-4}	7.87×10^{-4}	5.6
21.5	1.04×10^{-3}	1.13×10^{-3}	7.9
35.2	1.29×10^{-3}	1.28×10^{-3}	-0.77

In order to apply the kinetic model, proper boundary conditions are also needed. After testing the boundary conditions approach described in the previous section, it was found that the most consistent results are obtained when using the wall concentration estimated in a separate "boundary conditions" experiment. The boundary conditions experiment is, basically, the same type of the experiment described in Section 8.4.1. In this experiment, a N_2 gas at the same temperature, of the same flow rate (0.92 l/min) and the same initial RH (77.5 %) was humidified in the deliquescence reactor. The humidification was carried out using the same initial RH of the flow in the jacket and the experiment run in a way that the amount of water transferred to the inside flow was kept as close as possible to the amount of water transferred to the aerosol flow in the deliquescence kinetic experiment. The fitted flux obtained from that experiment was similarly used to verify the water mass balance, and the generated water concentration at the wall from that simulation used as the boundary conditions for the kinetic experiment. Figure 8.11 shows the water vapor concentration at the wall (blue line), obtained from such a "boundary condition" experiment.

Using this estimated wall concentration profile and assuming DRH = 79.6 %, the model was used to simulate the uptake of aerosols at each contact distance. The results of these simulations are shown in Table 8.6 and Figure 8.11. As discussed in Section 8.2, the uptake coefficient for each contact distance was determined as the value which generates the best agreement between the measured and calculated average concentration at the exit of the reactor. That is why all the simulation profiles shown in the Figure 8.11 "end" in the corresponding experimental measurement. It can be also observed that the simulated concentration profiles, shown in Figure 8.11, do not necessarily follow the "same" line. This is understandable, since these simulations were generated from different distributions, obtained at respective contact times. Although the individual simulations do not predict the "identical" average concentration routes, they are still similar enough and, what is important, they all result in comparable γ values.

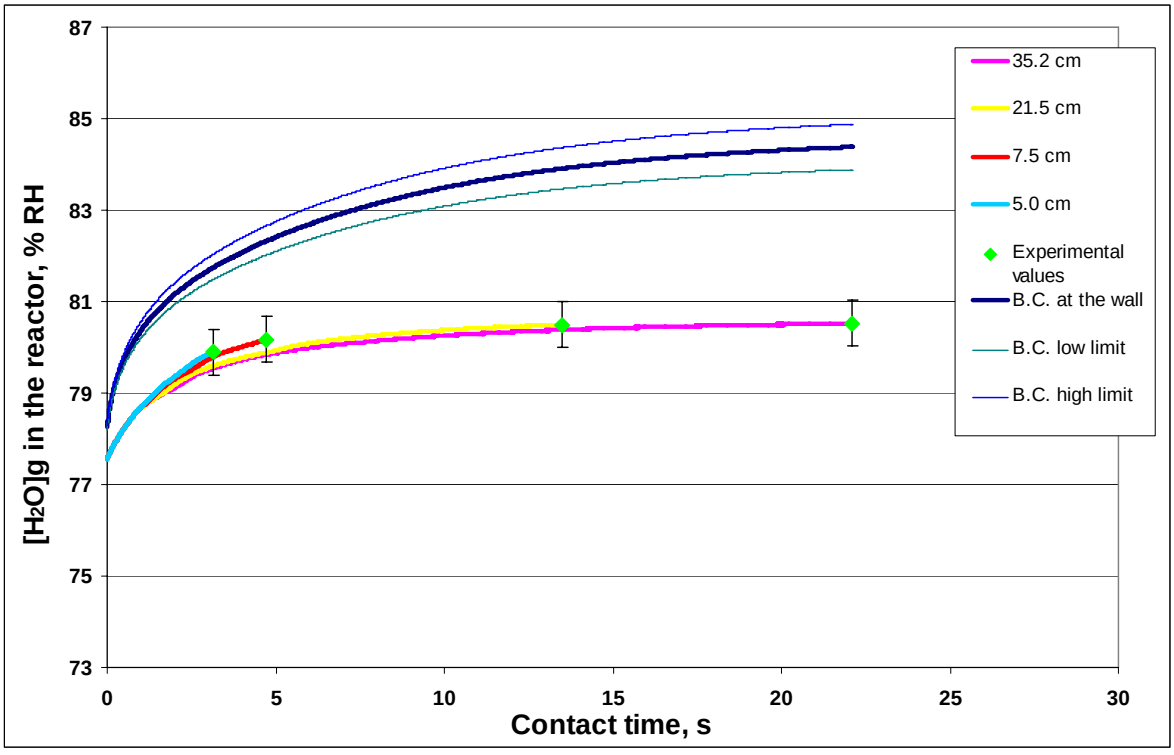

Figure 8.11: Simulated average water vapor concentrations in the reactor and at the wall for different contact times.

As shown in Table 8.6, the calculated gamma values for the contact distances from 5.0 to 35.2 cm are rather consistent, ranging between 0.0064 and 0.0080. It can be also noted that no results were reported for the two shortest contact distances - 1.3 and 2.5 cm. For these conditions, simulation did not result in any meaningful γ value, that is, the calculated values were outside the physically possible 0-1 range. This is most likely due to the fact that for this region it is difficult to accurately estimate the steep profile in the boundary conditions. Under those conditions there is a rather small amount of deliquesced aerosols, located primarily in the region next to or, virtually, at the wall, and any error in the estimated wall concentration will thus affect the simulation.

Table 8.6: Gamma values determined using 79.6% as the DRH value.

Distance, cm	Residence time, s	γ, 79.6% DRH as a cutoff value
1.3	0.78	/
2.8	1.76	/
5.0	3.14	$0.0069 \pm 4.34 \times 10^{-3}$
7.5	4.70	$0.0064 \pm 2.40 \times 10^{-3}$
21.5	13.5	$0.0075 \pm 2.99 \times 10^{-3}$
35.2	22.8	$0.0080 \pm 3.03 \times 10^{-3}$
Weighted mean of all determinations		$0.0072 \pm 6.54 \times 10^{-3}$

The sensitivity analysis of gamma has shown that uncertainties are mostly due to errors in estimating boundary conditions and aerosol size distribution. Although the accuracy of the humidity probe for this particular experiment was estimated to be 0.5%, this does not significantly contribute to the uncertainty in the calculated gamma. This is due to the fact that calculation of the uptake involves only relative changes in RH with respect to a certain referent value, like for instance in this case our initial RH (closed inlet position) of the aerosol flow. However, the choice of the representative DRH (cutoff) value with respect to the RHs corresponding to the beginning and the end of deliquescence process can significantly affect the calculated value of the uptake coefficient, as shown in Table 8.7.

Table 8.7: Gamma values determined using different cut-off (DRH) values.

Distance, cm	Residence time, s	γ, DRH=79.6%	γ, DRH=78.7%	γ, DRH=80.5%
1.3	0.78	/	/	/
2.8	1.76	/	/	/
5.0	3.14	0.0069	0.0033	0.0780
7.5	4.70	0.0064	0.0028	0.549
21.5	13.5	0.0075	0.0034	0.476
35.2	22.8	0.0080	0.0034	0.695

As expected, lower DRH cut-off values result in a decrease in the calculated gamma, whereas higher values lead to a significant increase in gamma. This is a direct consequence of the fact that DRH cut-off value determines the thickness of the boundary layer, within which it is assumed that all aerosols are deliquesced, while none is deliquesced in the dry core. This means that at a lower cut off value, the boundary layer is widened and the rate of the water uptake averaged over a bigger number of aerosols resulting in smaller γ. Similarly a higher cut-off value the thickness of the boundary layer is reduced and the uptake is due to a small fraction of particles in the high concentration region near the wall, resulting in high γs. As shown by the deliquescence experiment described in Chapter 7, this is not true description of the system. As it was shown by that experiment, there are aerosols deliquesced below that cut off RH, as well as that there are still non-deliquesced aerosols above that cut-off value.

This suggests that the kinetic model, in particular the part dealing with the description of the onset and offset of the deliquescence, require further improvement.

Chapter nine: Concluding remarks

9.1 Conclusions

In this work, the kinetics of the deliquescence process of ammonium sulfate aerosols has been studied experimentally. To the best of our knowledge, there have been no previous experimental (or theoretical) data available on the water vapor uptake by solid AMS aerosols and this is the first study of this kind. For that purpose, a new flow tube apparatus was designed. The apparatus is based on the system of Nafion dryers and humidifiers, which allows easy drying and humidification of the aerosol flow. The deliquescence reactor, witch is again a form of a Nafion humidifier, is also equipped with a movable inlet. The inlet enables easy variation of the contact time between aerosols and water vapor from the jacket, while keeping other experimental conditions constant. The system utilizes a Burgener nebulizer, which was shown to provide a stable source of aerosols over extended periods of time.

In the course of this work we have also tested and verified the numerical method for the characterization of aerosols from their IR extinction spectra. The method allows that the size, number distribution, phase and composition of aerosols be determined provided reliable refractive indices of the materials are known. For that purpose, we did a separate set of experiments to generate optical constants for the aerosol materials that are directly relevant to the AMS kinetic study. As a result of this work, we derived and reported a set of improved optical constants for solid AMS and a range of AMS solutions, from saturated (40% wt) to diluted (10% wt) liquid, in 5 % increments.

We have further shown that our new optical constants provide better fitting of the experimental spectra than those reported by B.Toon (for crystalline AMS) and S.Martin (for AMS solutions) and, thus, more reliable retrieval of particle distributions. Therefore, the new indices of refraction were used in the subsequent deliquescence and deliquescence kinetics experiments.These optical constants are also intended for the use in the characterization of AMS (aerosols) in remote sensing.

In the preparation for the kinetics study, the new deliquescence apparatus was tested by performing a standard deliquescence experiment to generate the well studied deliquescence curve of AMS. Under equilibrium conditions, the deliquescence in our flow system was observed to occur at RHs between the 77.9 and 80.8%, with the mean value determined as 79.6%±0.85. This is in excellent agreement with other values previously reported in the literature which are, typically, in the 78-80% range. Somewhat early onset of the deliquescence (77.9%) observed in our case could, perhaps, be attributed to the presence of water trapped in the particle pores during the drying process.

For the purpose of the deliquescence kinetic study, a new kinetic model was developed. The model allows determination of the water uptake on aerosols, based on the water vapor depletion in a laminar aerosol flow and the known number distribution of the deliquesced aerosols. The experiments were carried out at different degrees of deliquescence of solid aerosols in the flow, achieved by varying the contact time between the aerosol flow and water in the deliquescence reactor. The amount of water vapor transferred to the aerosol flow and the amount depleted due to its uptake by aerosols, were determined by monitoring relative humidities of the aerosol flow and the humid nitrogen flow in the reactor jacket. The number distributions of deliquesced aerosols were obtained from the IR extinction spectra, using the retrieval procedure.

The uptake coefficient of water vapor on solid AMS aerosols was determined to be in the range of 0.0025-0.011, with a weighted mean value of 0.0071, when assuming the deliquescence point at its mean value of 79.6 %. The sensitivity analysis of the model showed that the major uncertainty in the derived γ is due to the uncertainty in boundary conditions and retrieved size distribution. While the absolute value of RHs, including DRH, do not contribute significantly to this uncertainty, the choice of the DRH cut-off value does. This is due to the fact that the deliquescence does not occur abruptly at a single RH but over a range of humidities. The simplified approach of the current model regarding the treatment of the DRH point is something that should be addressed in future work.

9.2 Considerations for future work

We propose an improvement to the model, which would allow a more realistic treatment of the deliquescence process with respect to DRH. Since deliquescence apparently occurs over a range of humidities rather than at a single point, it seems necessary that the process be treated statistically.

This could be done by incorporating the probability density function (pdf) of the aerosol deliquescence in the humidity range of interest. For that purpose, the pdf function can be potentially generated from the dry and deliquesced aerosol number distributions retrieved in the standard deliquescence experiment (Chapter 7).

Once the kinetic model has been improved and the value of the water uptake on crystalline ammonium sulfate determined more accurately, it would be possible to further study the uptake of water on more diluted ammonium sulfate solution droplets. The versatility of the experimental setup and the tools developed for the characterization of ammonium sulfate aerosols allows us to study the deliquescence kinetic of other hygroscopic aerosols. In many cases, that would also require prior determination of the optical constants for the new aerosol materials which, as we showed, can be done easily in the existing or slightly modified set up.

It is known that the aerosol particles in the atmosphere often contain more than one component and their behavior as a cloud condensation nuclei (and their chemical and physical properties) is affected by their composition. Provided the database of the optical constants is available or the constants generated independently, the same method can be applied to study the uptake coefficient of multicomponent aerosols, such as mixed salts or inorganic-organic mixtures. This information would represent a valuable input to the models describing the effect of aerosols on climate change.

Finally, it should be noted that although there are obvious practical limitations to it, it would be very interesting to be able to study monodisperse aerosols. So far, we have been working with polydisperse aerosols, for which we have observed that the deliquescence occurs throughout all the modes in parallel. Thus, the derived uptake coefficient in this case refers to an average value, for the particular aerosol size distribution.

The fact is that working with monodisperse aerosols would to great extent simplify the entire procedure and the retrieval of more reliable kinetic data. However, more importantly, it would allow us to access the role of the aerosol size on the water uptake kinetics, a piece of information that would be of great interest not only to the atmospheric modeling studies, but also theoretical work such as molecular dynamic studies.

Annex

Nafion dryer performance testing

To establish optimal operating conditions for our experiments, we tested the Nafion dryer performance as a function of purge nitrogen flow rate, temperature and operating pressure of the atomizer. The experimental setups used for this study were the same as those employed in the study of optical constants for crystalline ammonium sulfate and SEM study, described in Chapters 3 and 4 respectively.

To asses the effect of the purge nitrogen flow rate on the Nafion drying efficiency, a solution of 2M $(NH_4)_2SO_4$ was atomized and the aerosols were carried into the system by 3 SLPM dry nitrogen. In this experiment the purge gas flow was varied from 3 to 26 SLPM. The RH obtained for each purge flow/aerosol flow ratio is presented in Table 6.

Table 1: The relative humidities measured as a function of the purge-to-aerosol flow ratio

Purge flow/Aerosol flow	2.33	3	3.67	4.33	5	8.67
RH,%	18.13	17.3	19	16.17	15.6	13.9

When changing experimental conditions we make sure that the system reached the new equilibrium state (constant RH and temperature), before recording spectra and moving on to new settings. For this particular experimental set up, we found that it takes about 15 minutes to reach a new equilibrium state. At least two IR spectra are recorded for each experimental condition to double check the RH.

As Figure 1 shows, the RH of the aerosol flow decreases linearly with the increase in the purge flow rate and it levels off at the purge-to-aerosol flow ratio of around 8. Additional increase in the purge flow rate does not contribute significantly to the further decrease in RH. This leads us to the conclusion that at this point the water vapor transfer from the aerosol side is diffusion limited and that for this geometry (size) of the dryer, the flow ratio of 8 is optimal to use when high drying rates are needed.

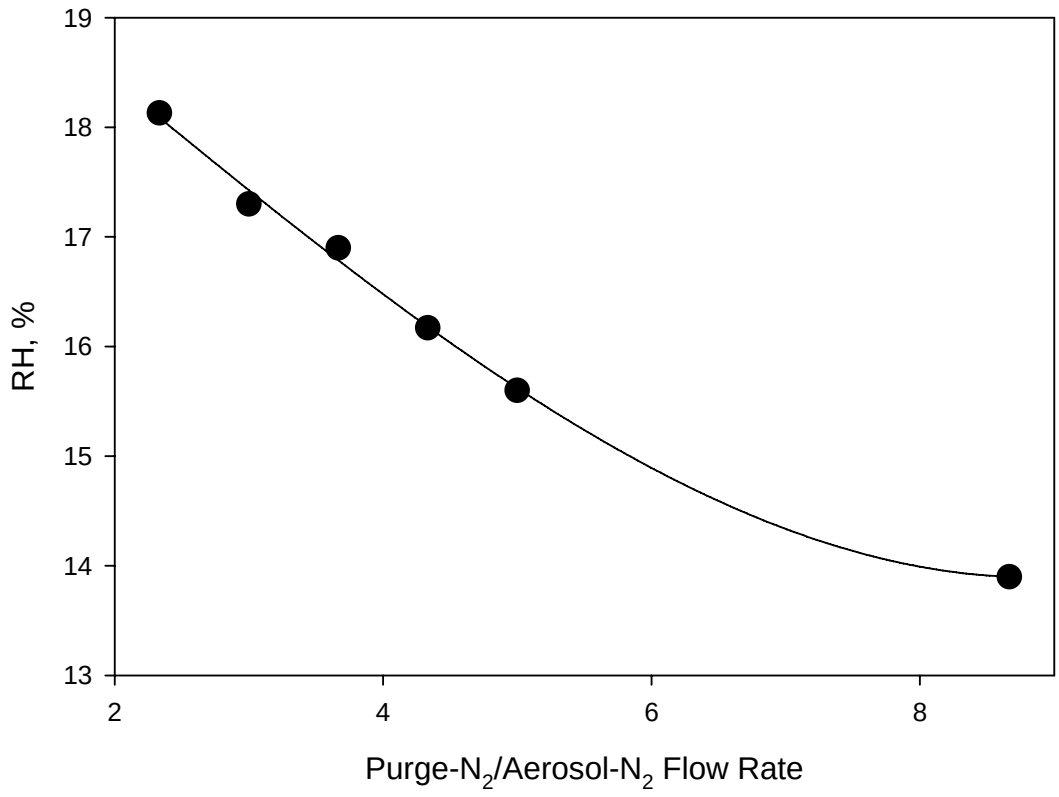

Figure 1: Efficiency of the Nafion dryer as a function of purge/aerosol flow rate at room temperature.

In the experiments carried out to test the temperature effect on the Nafion drying efficiency, the dryer was wrapped in foam insulation to reduce the temperature transfer between the system and the outside environment, and a thermocouple was introduced into the lower jacket inlet. Since Nafion drying efficiency depends inversely on temperature, the dryer was supplied with a flow of cooled purge gas, obtained by passing dry nitrogen through a copper coil immersed in an ice bath. At the exit of the ice bath, the copper tubing is wrapped with heating tape, this setup giving us control over the temperature of the purge gas. The results of this experiment are presented in Figure 2 where the red line indicated nearly the linear change in RH with the decrease in temperature and increase in the purge-to-aerosol flow ratio. As it can be seen, at a temperature of 9.4^{o}C and a flow ratio of 11, the RH can be reduced to 11.5%. Further decrease in temperature would require even higher drying flows which result in Nafion collapsing (inward).

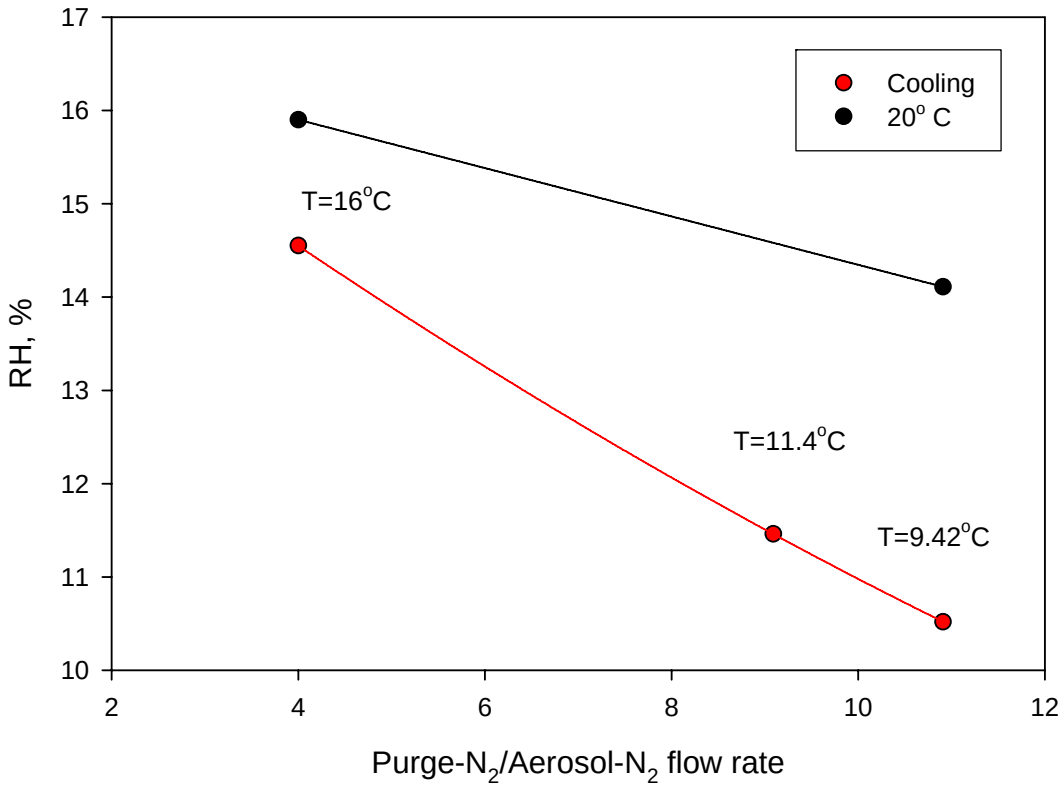

Figure 2: Nafion dryer efficiency dependence on the temperature and on the purge/aerosol flow rate.

The drying efficiency of the system was also tested in the presence of a KOH dryer, later used in the SEM experiments. In this particular experiment, aerosols were generated by atomizing 0.5 M $(NH_4)_2SO_4$ solution at 3 SLM. A set of experiments was done in which the aerosol flow was dried by using the Nafion or the KOH dryer only, or the combination of the two. The results are shown in Figure 3. It can be seen that at both, room and low temperature, there is a decrease in RH of the aerosol flow when the KOH dryer is connected to the experimental setup. A decrease of approximately 3% RH is seen at room temperature for any flow ratio, whereas a 4% RH decrease takes place at lower temperatures. With these conclusions in mind, SEM experiments were performed at around 10°C.

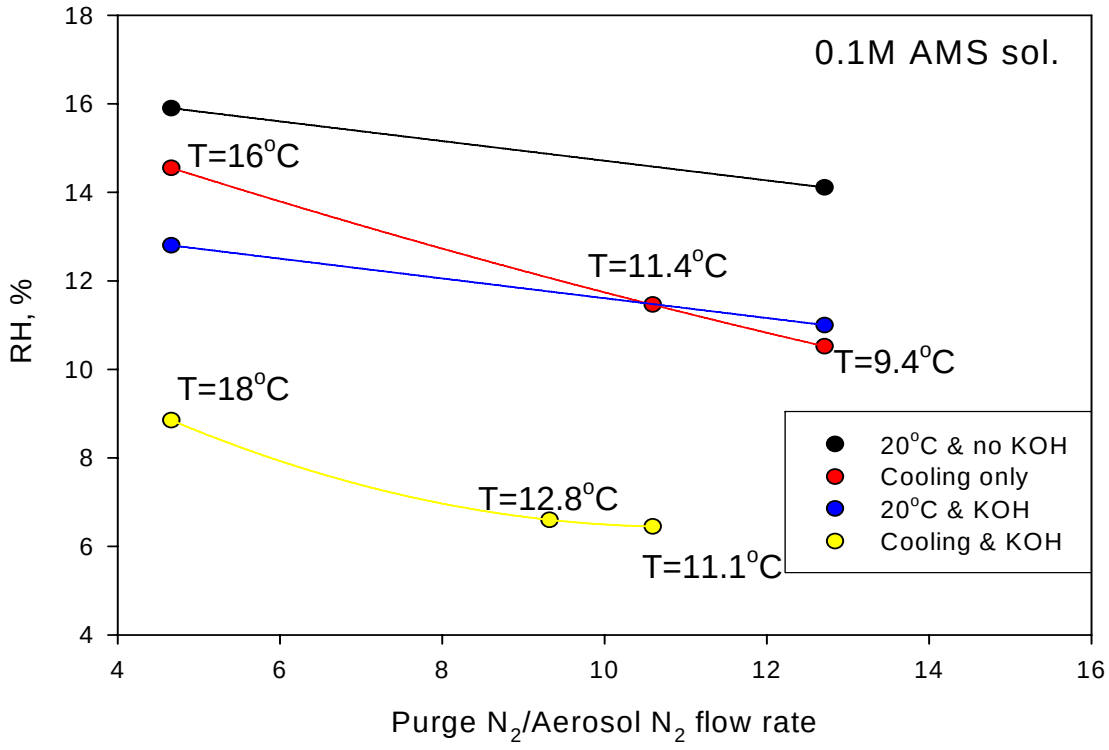

Figure 3: Water removal (from the aerosol flow) dependence on the: purge/aerosol flow rate (black line), temperature & purge/aerosol flow rate (red line), second dryer –KOH & purge/aerosol flow rate (blue line), second dryer & temperature & purge/aerosol flow rate (yellow line).

References

1. Buseck, P. R.; Posfai, M. Airborne Minerals and Related Aerosol Particles: Effects on Climate and the Environment. *Proceedings of the National Academy of Sciences of the United States of America* **1999,** *96,* 3372-3379.

2. Reist, P. *Aerosol Science and Technology*; McGraw-Hill Inc.: New York, **1993**; pp 267.

3. Warneck P. *Chemisty of the Natural Atmosphere*; Academic Press Inc.: Toronto, **1998**.

4. Campbell N.A.; Reece J.B. *Biology*; Benjamin Cummings: San Francisco, **2002**.

5. Timmer, B.; Olthuis, W.; van den Berg, A. Ammonia Sensors and Their Applications - a Review. *Sensors and Actuators B-Chemical* **2005,** *107,* 666-677.

6. Hinds, W. *Aerosol Technology*; Wiley-Interscience: **1999**.

7. Schwartz, S. The Whitehouse Effect-Shortwave Radiative Forcing of Climate by Anthropogenic Aerosols: an Overview. *Journal of Aerosol Science* **1996,** *27,* 359-382.

8. Seinfeld, J. H.; PandisS.N. *Atmospheric Chemistry and Physics- From Air Pollution to Climate Change*; Jhon Wiley & Sons, INC.: **1998**; pp 1-49.

9. Kiehl, J. T.; Trenberth, K. E. Earth's Annual Global Mean Energy Budget. *Bulletin of the American Meteorological Society* **1997,** *78,* 197-208.

10. Penner, J. E.; Chuang, C. C.; Grant, K. Climate Forcing by Carbonaceous and Sulfate Aerosols. *Climate Dynamics* **1998,** *14,* 839-851.

11. Kaufman, Y. J.; Fraser, R. S. The Effect of Smoke Particles on Clouds and Climate Forcing. *Science* **1997,** *277,* 1636-1639.

12. Crutzen P. http://insaindia.org/Anthropocene_Innsbruck%202006.ppt#1 . **2008**.

13. Klaus Willeke *Generation of Aerosols and Facilities for Exposure Experiments*; Ann Arbor Science: **1980**.

14. John W. Size Distribution Characteristics of Aerosols. In *Aerosol Measurement:Principles, Techniques and Applications*; Baron P., Willeke K., Eds.; John Wiley&Sons, INC.: **2001**.

15. Bohren C.F.; Huffman D.R. Absorption and Scattering by a Sphere. In *Absorption and Scattering of Light by Small Particles*; WILEY-VCH Verlag GmbH & Co. KGaA: Weinheim, Germany, **2004**; Chapter 4.

16. Department of Physics and Astronomy, G. S. U. HyperPhysics. http://hyperphysics.phy-astr.gsu.edu/hbase/hph.html . **2005**.

17. Cziczo, D. J.; Nowak, J. B.; Hu, J. H.; Abbatt, J. P. D. Infrared Spectroscopy of Model Tropospheric Aerosols As a Function of Relative Humidity: Observation of Deliquescence and Crystallization. *Journal of Geophysical Research, [Atmospheres]* **1997,** *102,* 18843-18850.

18. Djikaev, Y.; Doe, J.; Blow, J. Theory of Size Dependent Deliquescence of Nanoparticles: Relation to Heterogeneous Nucleation and Comparison With Experiments. *Journal of Physical Chemistry B* **2001,** 7708-7722.

19. Djikaev, Y.; Blow, J.; Doe, J. Kinetics of Fluctuational Deliquescence. *Journal of Chemical Physics* **2002,** *116,* 9865-9874.

20. Hameri, K.; Vakeva, M.; Hansson, H. C.; Laaksonen, A. Hygroscopic Growth of Ultrafine Ammonium Sulphate Aerosol Measured Using an Ultrafine Tandem Differential Mobility Analyzer. *Journal of Geophysical Research-Atmospheres* **2000,** *105,* 22231-22242.

21. Malvestuto, V.; Ascoli, S. A Deliquescence Model for Alkali Halide Nuclei. *Meteorologische Zeitschrift* **2001,** *10,* 37-43.

22. Mirabel, P.; Doe, J.; Blow, J. A Theory for the Deliquescence of Small Particles. *Journal of Chemical Physics* **2000,** *113,* 8200-8205.

23. Onasch, T. B.; Siefert, R. L.; Brooks, S. D.; Prenni, A. J.; Murray, B.; Wilson, M. A.; Tolbert, M. A. Infrared Spectroscopic Study of the Deliquescence and Efflorescence of Ammonium Sulfate Aerosol As a Function of Temperature. *Journal of Geophysical Research, [Atmospheres]* **1999,** *104,* 21317-21326.

24. Russell, L.; Ming, Y. Deliquescence of Small Particles. *Journal of Chemical Physics* **2002,** *116,* 311-321.

25. Weis, D. D.; Ewing, G. E. Water Content and Morphology of Sodium Chloride Aerosol Particles. *Journal of Geophysical Research-Atmospheres* **1999,** *104,* 21275-21285.

26. Tang, I. N.; Munkelwitz, H. R. Water Activities, Densities, and Refractive-Indexes of Aqueous Sulfates and Sodium-Nitrate Droplets of Atmospheric Importance. *Journal of Geophysical Research-Atmospheres* **1994,** *99,* 18801-18808.

27. Ge, Z. Z.; Wexler, A. S.; Johnston, M. V. Deliquescence Behavior of Multicomponent Aerosols. *Journal of Physical Chemistry A* **1998,** *102,* 173-180.

28. Finlayson-Pitts, B.; Pitts, J. Jr. *Chemistry of the Upper and Lower Atmosphere*; Academic Press: **1999**; pp 358-362.

29. Marcolli, C.; Luo, B. P.; Peter, T. Mixing of the Organic Aerosol Fractions: Liquids As the Thermodynamically Stable Phases. *Journal of Physical Chemistry A* **2004,** *108,* 2216-2224.

30. Hegg, D.; Larson, T.; Yuen, P. F. A Theoretical-Study of the Effect of Relative-Humidity on Light-Scattering by Tropospheric Aerosols. *Journal of Geophysical Research-Atmospheres* **1993,** *98,* 18435-18439.

31. Topping, D. O.; McFiggans, G. B.; Coe, H. A Curved Multi-Component Aerosol Hygroscopicity Model Framework: Part 1 - Inorganic Compounds. *Atmospheric Chemistry and Physics* **2005,** *5,* 1205-1222.

32. Topping, D. O.; McFiggans, G. B.; Coe, H. A Curved Multi-Component Aerosol Hygroscopicity Model Framework: Part 2 - Including Organic Compounds. *Atmospheric Chemistry and Physics* **2005,** *5,* 1223-1242.

33. Zasetsky, A.; Sloan, J. A New Method for the Quantitative Identification of the Composition, Size and Density of Stratospheric Aerosols From High Resolution IR Satelite Measurements. *Geophysical Research Letters* **2002,** *29,* 28-1-28-4.

34. Zasetsky, A. Y.; Khalizov, A. F.; Sloan, J. J. Characterization of Atmospheric Aerosols From Infrared Measurements: Simulations, Testing, and Applications. *Applied Optics* **2004,** *43,* 5503-5511.

35. Zasetsky, A. Y.; Khalizov, A. F.; Earle, M. E.; Sloan, J. J. Frequency Dependent Complex Refractive Indices of Supercooled Liquid Water and Ice Determined From Aerosol Extinction Spectra. *Journal of Physical Chemistry A* **2005,** *109,* 2760-2764.

36. Clapp, M. L.; Miller, R. E.; Worsnop, D. R. Frequency-Dependent Optical-Constants of Water Ice Obtained Directly From Aerosol Extinction Spectra. *J. Phys. Chem.* **1995,** *99,* 6317-6326.

37. TSI Constant Output Atomizer model 3076. http://www.tsi.com/products/atomizer.aspx . **2005**.

38. Instech. http://www.instechlabs.com/Pumps/peristaltic/ . **2007**.

39. Burgener Research Inc. http://burgenerresearch.com/MiraMistManual.html . **2007**.

40. Perma Pure LLC. http://www.permapure.com/ . **2007**.

41. Day, D. E.; Malm, W. C.; Kreidenweis, S. M. Aerosol Light Scattering Measurements As a Function of Relative Humidity. *Journal of the Air & Waste Management Association* **2000,** *50,* 710-716.

42. Leckrone, K.; Hayes, J. Efficiency and Temperature Dependence of Water Removal by Membrane Dryers. *Analytical Chemistry* **1997,** *69,* 911-918.

43. Wang, K. L.; Mccray, S. H.; Newbold, D. D.; Cussler, E. L. Hollow Fiber Air Drying. *Journal of Membrane Science* **1992,** *72,* 231-244.

44. FluoroPel Product Information. http://www.cytonix.com/fluoroproducts.html . **2005**.

45. Vaisala's HM70 Hand-Held Humidity and Temperature Meter. http://www.vaisala.com/DynaGen_Attachments/Att27258/HM70%20Brochure.pdf . **2005**.

46. Greenspan, L. Humidity Fixed Points of Binary Saturated Aqueous Solutions. *Journal of Research of the National Bureau of Standards - A* **1977,** *81A*.

47. Toon, O. B.; Pollack, J. B.; Khare, B. N. The Optical Constants of Several Atmospheric Aerosol Species: Ammonium Sulfate, Aluminum Oxide, and Sodium Chloride. *Journal of Geophysical Research* **1976,** *81,* 5733-5748.

48. Cziczo, D. J.; Abbatt, J. P. D. Deliquescence, Efflorescence, and Supercooling of Ammonium Sulfate Aerosols at Low Temperature: Implications for Cirrus Cloud Formation and Aerosol Phase in the Atmosphere. *J. Geophys. Res.* **1999,** *104,* 13781-13790.

49. Han, J. H.; Martin, S. T. An Aerosol Chemical Reactor for Coating Metal Oxide Particles With (NH4)SO4-H2SO4-H2O.1. - New Particle Formation. *Aerosol Science and Technology* **2001,** *34,* 363-372.

50. Hung, H. M.; Martin, S. T. Infrared Spectroscopic Evidence for the Ice Formation Mechanisms Active in Aerosol Flow Tubes. *Appl. Spectrosc.* **2002,** *56,* 1067-1081.

51. Onasch, T. B.; Siefert, R. L.; Brooks, S. D.; Prenni, A. J.; Murray, B.; Wilson, M. A.; Tolbert, M. A. Infrared Spectroscopic Study of the Deliquescence and Efflorescence of Ammonium Sulfate Aerosol As a Function of Temperature. *J. Geophys. Res. -Atmos.* **1999,** *104,* 21317-21326.

52. Zasetsky, A. Y.; Khalizov, A. F.; Earle, M. E.; Sloan, J. J. Frequency Dependent Complex Refractive Indices of Supercooled Liquid Water and Ice Determined From Aerosol Extinction Spectra. *J. Phys. Chem. A* **2005,** *109,* 2760-2764.

53. Socrates, G. *Infrared and Raman Characteristic Group Frequencies : Tables and Charts*; Wiley: New York, **2001**.

54. Weis, D. D.; Ewing, G. E. Infrared Spectroscopic Signatures of (NH4)(2)SO4 Aerosols. *J. Geophys. Res.* **1996,** *101,* 18709-18720.

55. Brooks, S. D.; Garland, R. M.; Wise, M. E.; Prenni, A. J.; Cushing, M.; Hewitt, E.; Tolbert, M. A. Phase Changes in Internally Mixed Maleic Acid/Ammonium Sulfate Aerosols. *J. Geophys. Res.* **2003,** *108*.

56. Dick, W. D.; Ziemann, P. J.; Huang, P. F.; McMurry, P. H. Optical Shape Fraction Measurements of Submicrometre Laboratory and Atmospheric Aerosols. *Meas. Sci. Technol.* **1998,** *9,* 183-196.

57. Sjogren, S.; Gysel, M.; Weingartner, E.; Baltensperger, U.; Cubison, M. J.; Coe, H.; Zardini, A. A.; Marcolli, C.; Krieger, U. K.; Peter, T. Hygroscopic Growth and Water Uptake Kinetics of Two-Phase Aerosol Particles Consisting of Ammonium Sulfate, Adipic and Humic Acid Mixtures. *Journal of Aerosol Science* **2007,** *38,* 157-171.

58. Martin, S. T.; Hung, H. M.; Park, R. J.; Jacob, D. J.; Spurr, R. J. D.; Chance, K. V.; Chin, M. Effects of the Physical State of Tropospheric Ammonium-Sulfate-Nitrate Particles on Global Aerosol Direct Radiative Forcing. *Atmospheric Chemistry and Physics* **2004,** *4,* 183-214.

59. Chelf, J. H.; Martin, S. T. Homogeneous Ice Nucleation in Aqueous Ammonium Sulfate Aerosol Particles. *Journal of Geophysical Research-Atmospheres* **2001,** *106,* 1215-1226.

60. Hung, H. M.; Martin, S. T. Infrared spectroscopic evidence for the ice formation mechanisms active in aerosol flow tubes. *Applied Spectroscopy* **2002**,56, 1067-1081.

61. Gosse, S. F.; Wang, M. Y.; Labrie, D.; Chylek, P. Imaginary Part of the Refractive Index of Sulfates and Nitrates in the O.7-2.8-Mu m Spectral Region. *Applied Optics* **1997,** *36,* 3622-3634.

62. Remsberg, E. E. Optical Constants of Concentrated Aqueous Ammonium Sulfate. *Applied Optics* **1973,** *12,* 1389-1390.

63. Downing, H. D.; Pinkley, L. W.; Sethna, P. P.; Williams, D. Optical Constants of Ammonium Sulfate in the Infrared. *Journal of the Optical Society of America* **1977,** *67,* 186-190.

64. Cziczo, D. J.; Abbatt, J. P. D. Deliquescence, Efflorescence, and Supercooling of Ammonium Sulfate Aerosols at Low Temperature: Implications for Cirrus Cloud Formation and Aerosol Phase in the Atmosphere. *Journal of Geophysical Research, [Atmospheres]* **1999,** *104,* 13781-13790.

65. Weis, D. D.; Ewing, G. E. Infrared Spectroscopic Signatures of (NH4)2SO4 Aerosols. *Journal of Geophysical Research, [Atmospheres]* **1996,** *101,* 18709-18720.

66. Zasetsky, A. Y.; Earle, M. E.; Cosic, B.; Schiwon, R.; Grishin, I. A.; McPhail, R.; Pancescua, R. G.; Najera, J.; Khalizov, A. F.; Cook, K. B.; Sloan, J. J. Retrieval of Aerosol Physical and Chemical Properties From Mid-Infrared Extinction Spectra. *Journal of Quantitative Spectroscopy & Radiative Transfer* **2007,** *107,* 294-305.

67. Cruz, C. N.; Pandis, S. N. Deliquescence and Hygroscopic Growth of Mixed Inorganic-Organic Atmospheric Aerosol. *Environmental Science and Technology* **2000,** *34,* 4313-4319.

68. Hameri, K.; Charlson, R.; Hansson, H. C. Hygroscopic Properties of Mixed Ammonium Sulfate and Carboxylic Acids Particles. *AIChE Journal* **2002,** *48,* 1309-1316.

69. Brooks, S. D.; Garland, R. M.; Wise, M. E.; Prenni, A. J.; Cushing, M.; Hewitt, E.; Tolbert, M. A. Phase Changes in Internally Mixed Maleic Acid/Ammonium Sulfate Aerosols. *Journal of Geophysical Research-Atmospheres* **2003,** *108*.

70. Tang, I. Thermodynamic and Optical Properties of Mixed-Salt Aerosols of Atmospheric Importance. *Journal of Geophysical Research* **1997,** *102,* 1883-1893.

71. Biskos, G.; Paulsen, D.; Russell, L. M.; Buseck, P. R.; Martin, S. T. Prompt Deliquescence and Efflorescence of Aerosol Nanoparticles. *Atmospheric Chemistry and Physics* **2006,** *6,* 4633-4642.

72. Colberg, C. A.; Krieger, U. K.; Peter, T. Morphological Investigations of Single Levitated H2SO4/NH3/H2O Aerosol Particles During Deliquescence/Efflorescence Experiments. *Journal of Physical Chemistry A* **2004,** *108,* 2700-2709.

73. Gysel, M.; Weingartner, E.; Baltensperger, U. Hygroscopicity of Aerosol Particles at Low Temperatures. 2. Theoretical and Experimental Hygroscopic Properties of Laboratory Generated Aerosols. *Environmental Science & Technology* **2002,** *36,* 63-68.

74. Kuni, F. M.; Shchekin, A. K.; Rusanov, A. I. Kinetics of Condensation on Soluble Nuclei. *Colloid Journal of the Russian Academy of Sciences* **1993,** *55,* 184-192.

75. Kuni, F. M.; Shchekin, A. K.; Rusanov, A. I. Condensation on Soluble Nuclei in the Region of Their Partial Dissolution. *Colloid Journal of the Russian Academy of Sciences* **1993,** *55,* 686-696.

76. Shchekin, A. K.; Rusanov, A. I.; Kuni, F. M. Thermodynamics of Condensation in the Formation of A Film on A Soluble Nucleus. *Colloid Journal of the Russian Academy of Sciences* **1993,** *55,* 776-783.

77. Shchekin, A. K.; Grinin, A. P.; Kuni, F. M. Kinetics of Dissolution, Adsorption, and Relaxation of the Matter Comprising Condensation Nucleus to Equilibrium in a Droplet Originating on the Nucleus. *Colloid Journal* **1998,** *60,* 111-121.

78. Narsimhan, G.; Ruckenstein, E. A New Approach for the Prediction of the Rate of Nucleation in Liquids. *Journal of Colloid and Interface Science* **1989,** *128,* 549-565.

79. Nowakowski, B.; Ruckenstein, E. Homogeneous Nucleation in Gases - A 3-Dimensional Fokker-Planck Equation for Evaporation From Clusters. *Journal of Chemical Physics* **1991,** *94,* 8487-8492.

80. Nowakowski, B.; Ruckenstein, E. A Kinetic Approach to the Theory of Nucleation in Gases. *Journal of Chemical Physics* **1991,** *94,* 1397-1402.

81. Ruckenstein, E.; Nowakowski, B. A Kinetic-Theory of Nucleation in Liquids. *Journal of Colloid and Interface Science* **1990,** *137,* 583-592.

82. Djikaev, Y. S.; Ruckenstein, E. A Kinetic Approach to the Theory of Heterogeneous Nucleation on Soluble Particles During the Deliquescence Stage. *Journal of Chemical Physics* **2006,** *124*.

83. Remorov, R. G.; George, C. Analysis of Chemical Kinetics at the Gas-Aqueous Interface for Submicron Aerosols. *Physical Chemistry Chemical Physics* **2006,** *8,* 4897-4901.

84. Remorov, R. G.; Zasetsky, A. Y.; Sloan, J. J. Low Pressure Aerosol Flow Reactor. *Aerosol Science and Technology* **2005,** *39,* 1038-1047.

85. Fuchs N.A..; Sutugin A.G. *Highly Dispersed Aerosols*. Ann Arbor, Ann Arbor Science.